OPTIMIZATION OF PHOTOVOLTAIC PERFORMANCE IN DSSCs VIA CuO DOPING OF TiO_2 AND ZnO PHOTOANODES

Higor Oliveira da Cunha

Thesis submitted to the Graduate Program in Instrumentation and Applied Optics (PPGIO), jointly offered by the Federal Center for Technological Education Celso Suckow da Fonseca (CEFET/RJ) and Fluminense Federal University (UFF), in partial fulfillment of the requirements for the degree of Doctor of Electrical Engineering.

Advisor: Profª Ana Lucia Ferreira de Barros, D.Sc.

Rio de Janeiro
April, 2026

OPTIMIZATION OF PHOTOVOLTAIC PERFORMANCE IN DSSCs
VIA CuO DOPING OF TiO_2 AND ZnO PHOTOANODES

Doctoral thesis presented to the Graduate Program in Instrumentation and Applied Optics at the Federal Center for Technological Education Celso Suckow da Fonseca (CEFET/RJ) and the Fluminense Federal University (UFF), as part of the requirements for obtaining the degree of Doctor of Electrical Engineering.

Higor Oliveira da Cunha

Examining Committee:

Ana Lucia Ferreira de Barros
Assinado de forma digital por Ana Lucia Ferreira de Barros
Dados: 2026.09.15 08:31:36 -03'00'

President, Ana Lucia Ferreira de Barros, D.Sc. (CEFET/RJ) (Orientadora)

Documento assinado digitalmente
gov.br
MARIA LUIZA ROCCO DUARTE PEREIRA
Data: 28/07/2026 14:42:15-0300
Verifique em https://validar.iti.gov.br

Maria Luiza Rocco Duarte Pereira, PhD (UFRJ/RJ)

Documento assinado digitalmente
gov.br
FABIO DA SILVA MIRANDA
Data: 28/07/2026 15:03:06-0300
Verifique em https://validar.iti.gov.br

Fabio da Silva Miranda, D.Sc. (UFF/RJ)

Documento assinado digitalmente
gov.br
ALVARO LUIS MARTINS DE ALMEIDA NOGUEIRA
Data: 29/07/2026 08:50:54-0300
Verifique em https://validar.iti.gov.br

Álvaro Luis Martins de Almeida Nogueira, D.Sc. (CEFET/RJ)

Documento assinado digitalmente
gov.br
VINICIUS NUNES HENRIQUE SILVA
Data: 30/07/2026 21:38:51-0300
Verifique em https://validar.iti.gov.br

Vinicius Nunes Henrique Silva, D.Sc. (UFF/RJ)

Rio de Janeiro
April, 2026

Ficha catalográfica elaborada pela Biblioteca Central do CEFET/RJ

C972 Cunha, Higor Oliveira da
Optimization of photovoltaic performance in DSSCs via CuO doping of TIO_2 and ZnO photoanodes / Higor Oliveira da Cunha – 2026.
156f : il. (algumas color.). , enc.

Tese (Doutorado). Centro Federal de Educação Tecnológica Celso Suckow da Fonseca, 2026.
Bibliografia : f. 144-156.
Orientadora: Ana Lucia Ferreira de Barros.

1. Geração de energia fotovoltaica. 2. Fotoeletroquímica. 3. Efeito fotovoltaico. 4. Células solares de Grätzel. 5. Energia solar. I. Barros, Ana Lucia Ferreira de (Orient.). II. Título.

CDD 621.31244

Elaborada pelo bibliotecário Leandro Mota de Menezes – CRB/7 nº 5281

DEDICAÇÃO

À minha mãe Maria Cleonice, ao meu pai Paulo Ferreira (*in memoriam*), à minha avó Maria da Guia (*in memoriam*), e aos meus queridos irmãos Gabriel Cunha e Thiago Cunha, por terem me ajudado ao longo desta trajetória acadêmica. A todos os amigos e professores que de alguma maneira estiveram comigo durante esse período e fizeram parte deste trabalho.

AGRADECIMENTOS

Agradeço aos meus pais por todos os esforços que já fizeram por mim, aos meus irmãos por sempre acreditarem no meu potencial e por todo o incentivo, ao meu primo e amigo Guilherme Freire por estar sempre ao meu lado, da mesma forma, aos meus amigos Vitor Paulo e Vitor Hugo.

O meu agradecimento especial à minha orientadora, Profª Drª Ana Lucia Ferreira de Barros pela oportunidade da realização deste trabalho. Extremamente grato por toda orientação, diligência e confiança ao longo deste tempo de convivência no desenvolvimento desta pesquisa.

Agradeço também a todos os professores do Programa de Pós-Graduação em Instrumentação e Óptica Aplicada (PPGIO) do Centro Federal de Educação Tecnológica Celso Suckow da Fonseca (CEFET/RJ), e da Universidade Federal Fluminense (UFF), pelas excelentes aulas ministradas, contribuindo de maneira ímpar para a minha evolução acadêmica e pessoal. Pela mesma razão, agradeço aos professores do Programa de Engenharia Elétrica (PEE) da Universidade Federal do Rio de Janeiro (COPPE/UFRJ), onde cursei parte das disciplinas de mestrado e doutorado.

Agradeço a todos os amigos do Laboratório de Física Experimental e Aplicada (LaFEA) do CEFET/RJ. Em especial, agradeço ao doutorando Arcano Matheus, por estar trabalhando comigo no LaFEA desde o mestrado e por toda a amizade além dos cálculos e experimentos realizados; ao Doutor Leonardo Bernardes pela amizade e por toda ajuda de sempre; ao pós-doutorando Rajendran Suresh Babu, por todo o suporte durante a pesquisa; ao doutorando e Profº José Antônio Rodrigues; à doutoranda e Profª Monique Pacheco, e ao Reinaldo Santana.

Por fim, agradeço ao CEFET/RJ, à FINEP, à CAPES, ao CNPq e à FAPERJ pelos recursos disponibilizados ao Laboratório de Física Experimental e Aplicada (LaFEA) para a realização deste trabalho.

Deixo registrado nestas páginas os meus sinceros agradecimentos a todos que me ajudaram a concluir esta etapa na minha vida, pois além de toda a minha dedicação e comprometimento, esta conquista só foi possível graças à ajuda de cada um de vocês.

A todos que me ajudaram até aqui, muito obrigado!

Higor Oliveira da Cunha

EPÍGRAFE

"*O destino embaralha as cartas e nós jogamos.*"

(Arthur Schopenhauer)

"*O primeiro dever da inteligência é desconfiar dela mesma.*"

(José Ortega y Gasset)

RESUMO

OTIMIZAÇÃO DO DESEMPENHO FOTOVOLTAICO EM CÉLULAS SOLARES SENSIBILIZADAS POR CORANTE (DSSCs) POR MEIO DA DOPAGEM COM CuO EM FOTOANODOS DE TiO_2 E ZnO

Este trabalho investiga o efeito da dopagem com óxido de cobre (CuO) no desempenho de células solares sensibilizadas por corante (DSSCs) baseadas em dióxido de titânio (TiO_2) e óxido de zinco (ZnO). Fotoanodos híbridos foram preparados utilizando TiO_2 ou ZnO dopados com CuO em diferentes concentrações (0–50 wt%).

A análise por difração de raios X (DRX) evidenciou modificações estruturais associadas à incorporação do dopante, com aumento da intensidade dos picos característicos do CuO em maiores concentrações. A morfologia e composição elementar foram avaliadas por microscopia eletrônica de varredura (MEV) e fluorescência de raios X (FRX), respectivamente. As DSSCs foram sensibilizadas com o corante padrão N3 e com extrato natural de *Vitis labrusca* (V.L.), cuja presença de antocianinas foi confirmada por espectroscopias no ultravioleta-visível (UV-Vis) e no infravermelho por Transformada de Fourier (FTIR).

Os resultados eletroquímicos indicaram que a dopagem com CuO promoveu melhoria significativa no desempenho fotovoltaico, com eficiência máxima observada para 20 wt% de dopante. Para dispositivos sensibilizados com Vitis labrusca, foram obtidas eficiências de 1,15% para TiO_2–CuO e 0,92% para ZnO–CuO. Para o corante N3, os valores atingiram 1,81% e 1,53%, respectivamente.

Em comparação, os fotoanodos não dopados apresentaram desempenho inferior, com eficiências de 0,18% (TiO_2) e 0,14% (ZnO) para Vitis labrusca, e 0,85% (TiO_2) e 0,70% (ZnO) para o corante N3. Esses resultados demonstram que a dopagem com CuO resulta em um aumento expressivo na eficiência, especialmente para sistemas sensibilizados com corantes naturais.

A incorporação de CuO em fotoanodos de TiO_2 e ZnO mostrou-se uma estratégia eficaz para melhorar a conversão fotovoltaica em DSSCs, destacando o potencial desses sistemas como alternativas sustentáveis para geração de energia.

Palavras-chave: Fotoeletroquímica; Células solares de Grätzel; Eletrodos anódicos; Energia renovável; Efeito fotovoltaico.

ABSTRACT

OPTIMIZATION OF PHOTOVOLTAIC PERFORMANCE IN DSSCS VIA CuO DOPING OF TIO_2 AND ZnO PHOTOANODES

This work investigates the effect of copper oxide (CuO) doping on the performance of dye-sensitized solar cells (DSSCs) based on titanium dioxide (TiO_2) and zinc oxide (ZnO). Hybrid photoanodes were prepared using TiO_2 or ZnO doped with CuO at different concentrations (0–50 wt%).

X-ray diffraction (XRD) analysis revealed structural modifications associated with dopant incorporation, with increased intensity of characteristic CuO peaks at higher concentrations. Morphological and elemental characterizations were carried out using scanning electron microscopy (SEM) and X-ray fluorescence (XRF), respectively. The DSSCs were sensitized with the standard N3 dye and with a natural extract of *Vitis labrusca* (V.L.), the presence of anthocyanins in which was confirmed by ultraviolet-visible (UV-Vis) and Fourier-transform infrared (FTIR) spectroscopies.

Electrochemical measurements showed that CuO doping significantly enhances photovoltaic performance, with maximum efficiency achieved at 20 wt% doping. For devices sensitized with Vitis labrusca, conversion efficiencies of 1.15% for TiO_2–CuO and 0.92% for ZnO–CuO were obtained. For N3-based devices, efficiencies reached 1.81% and 1.53%, respectively.

In comparison, undoped photoanodes exhibited lower performance, with efficiencies of 0.18% (TiO_2) and 0.14% (ZnO) for Vitis labrusca, and 0.85% (TiO_2) and 0.70% (ZnO) for the N3 dye. These results demonstrate that CuO doping leads to a significant improvement in photovoltaic efficiency, particularly in systems using natural sensitizers.

The incorporation of CuO into TiO_2 and ZnO photoanodes represents an effective strategy to enhance DSSC performance, highlighting the potential of these systems as sustainable alternatives for solar energy conversion.

Keywords: Photoelectrochemistry; Grätzel solar cells; Anode electrodes; Renewable energy; Photovoltaic effect.

LIST OF FIGURES

Figure 1 - Solar radiation spectrum. Adapted from: [10]. 20
Figure 2 - Structure of the Sun. Adapted from: [14]. 21
Figure 3 – Electromagnetic spectrum of solar and terrestrial radiation. Adapted from: [17]. 22
Figure 4 - Earth's Energy Balance. Adapted from: [19]. 24
Figure 5 - World map of the spatial distribution of solar energy. Adapted from: [20]. . 25
Figure 6 – Solar irradiance throughout the day. Adapted from: [21]. 25
Figure 7 - Basic principle of a photovoltaic cell. Adapted from: [23]. 26
Figure 8 - P-N junction. Adapted from: [25]. 28
Figure 9 - (a) Evolution of solar cells and (b) Cost vs. efficiency relationship between first (I), second (II) and third generation (III) solar cells. Adapted from: [27, 33]. 34
Figure 10 – Components of DSSCs [38]. 38
Figure 11 – Steps in the dye preparation process: (a) utilization of the peels, (b) drying, (c) crushing, (d) crushed peels, (e) dye extraction, (f) filtering, (g) finished dye. 40
Figure 12 – Anodic solutions in different proportions. 41
Figure 13 – Spin coating technique. 42
Figure 14 – Terminated anodes: (a) ZnO and TiO_2, (b) ZnO-$CuO_{5\%}$ and TiO_2-$CuO_{5\%}$, (c) ZnO-$CuO_{10\%}$ and TiO_2-$CuO_{10\%}$, (d) ZnO-$CuO_{20\%}$ and TiO_2-$CuO_{20\%}$, (e) ZnO-$CuO_{30\%}$ and TiO_2-$CuO_{30\%}$, (f) ZnO-$CuO_{50\%}$ and TiO_2-$CuO_{50\%}$. 42
Figure 15 – Preparation of cathodes. 43
Figure 16 - Pt cathodes. 43
Figure 17 – DSSCs assembly diagram. Adapted from: [67]. 44
Figure 18 – Assembled DSSCs: (a) ZnO, TiO_2 (V.L. and N3), (b) ZnO-$CuO_{5\%}$, TiO_2-$CuO_{5\%}$ (V.L. and N3), (c) ZnO-$CuO_{20\%}$, TiO_2-$CuO_{20\%}$ (V.L. and N3), (d) ZnO-$CuO_{30\%}$, TiO_2-$CuO_{30\%}$ (V.L. and N3), (e) ZnO-$CuO_{10\%}$, TiO_2-$CuO_{10\%}$ (V.L. and N3), (f) ZnO-$CuO_{50\%}$, TiO_2-$CuO_{50\%}$ (V.L. and N3) 45
Figure 19 – Summary of the steps in constructing Grätzel cells: (a) Fruit used and Ru, (b) Dye extraction, (c) Anodic solutions, (d) Spin coating, (e) Drop casting, (f) Annealing in a muffle furnace, (g) Cathodes, (h) Anodes, and (i) DSSCs. 45
Figure 20 – Diagram of DSSC operation. 46

Figure 21 – Schematic of the effect of CuO doping on TiO_2/ZnO. Adapted from: [67]. 51
Figure 22 – Organizational chart of optical, morphological, structural, and electrochemical characterizations. 54
Figure 23 - Optical characterization of natural dye extracted from black grapes using FTIR – LaFEA (model: Agilent Cary 630). 55
Figure 24 – Operation of the UV-VIS spectrophotometer (model: SHIMADZU UV-2600i). Adapted from: [48]. 58
Figure 25 – Spectrophotometer used in UV-VIS absorbance analyses – LaFEA (model: SHIMADZU UV-2600i). 60
Figure 26 - X-ray diffraction technique. Adapted from: [53]. 63
Figure 27 - Geometric representation of diffraction according to Bragg's Law. Adapted from: [54]. 63
Figure 28 - D2 Phaser equipment used in XRD analyses. 64
Figure 29 - Schematic representation of the X-ray fluorescence process. Adapted from: [58]. 67
Figure 30 – Equipment for X-ray fluorescence characterization (Epsilon 1, model: Malvern Panalytical). 68
Figure 31 – Scanning Electron Microscope (SEM) – NanoFAB (UERJ) (model: JEOL JSM-7100F). 70
Figure 32 – Simplified schematic representation of the components that make up the SEM. Adapted from: [61]. 71
Figure 33 – Operating principle of the atomic force microscope. Adapted from: [65].. 74
Figure 34 – Measurements performed using AFM – LaFEA (model: Nanosurf EasyScan 2). 75
Figure 35 – Multi-potentiostat in conjunction with the solar simulator (Ivisun® IVIUM Technologies – IVIUM Compactstat). 76
Figure 36 – Characteristic curves of DSSCs (J–V) and (P–V). 79
Figure 37 – Fill Factor (FF). 80
Figure 38 – (a) Nyquist and (b) Equivalent Circuit. Adapted from: [72]. 82
Figure 39 – Transmittance spectra of the evaluated dyes. Adapted from: [28,30]. 85
Figure 40 – Absorbance of natural dyes. Adapted from: [28,30]. 90

Figure 41 – Basic molecular structure of anthocyanin [69]. 90
Figure 42 – Samples (XRD): (a) CuO, (b) TiO_2, (c) TiO_2-$CuO_{5\%}$, (d) TiO_2-$CuO_{10\%}$, (e) TiO_2-$CuO_{20\%}$, (f) TiO_2-$CuO_{30\%}$, (g) TiO_2-$CuO_{50\%}$. Adapted from: [38]. 94
Figure 43 – Samples (XRD): (a) ZnO, (b) ZnO-$TiO_{5\%}$, (c) ZnO-$CuO_{10\%}$, (d) ZnO-$CuO_{20\%}$, (e) ZnO-$CuO_{30\%}$, (f) ZnO-$CuO_{50\%}$. Adapted from: [38]. 95
Figure 44 – Overlap of TiO_2 samples varying with CuO doping. Adapted from: [38].. 96
Figure 45 – Overlap of ZnO samples varying with CuO doping. Adapted from: [38]. . 96
Figure 46 – Samples (XRF): (a) CuO, (b) TiO_2, (c) TiO_2-$CuO_{5\%}$, (d) TiO_2-$CuO_{10\%}$, . 100
Figure 47 – Samples (XRF): (a) ZnO, (b) ZnO-$CuO_{10\%}$, (c) ZnO-$CuO_{20\%}$,..... 101
Figure 48 – XRF spectra of TiO_2 samples doped with CuO. Adapted from: [38]. 102
Figure 49 – XRF spectra of ZnO samples doped with CuO. Adapted from: [38]..... 102
Figure 50 – Surface morphologies performed by SEM: (a) TiO_2 anode, (b) Pt cathode, (c) TiO_2-CuO anode, (d) ZnO-CuO anode, (e) ZnO [30,73,77-79]. 104
Figure 51 – Surface morphologies from this work performed using SEM: (a) TiO_2, (b) ZnO [38]. 105
Figure 52 – Surface morphology of this work performed using SEM: Pt cathode [38]. 107
Figure 53 – Surface morphologies of TiO_2-CuO from this work performed by SEM at different concentrations: (a) 5%, (b) 10%, (c) 20%, (d) 30%, (e) 50% [38]. 108
Figure 54 – Surface morphologies of ZnO-CuO from this work performed by SEM at different concentrations: (a) 5%, (b) 10%, (c) 20%, (d) 30%, (e) 50% [38]. 111
Figure 55 – TiO_2 anodes by spin coating technique: (a), (b) and (c). Pt cathodes by drop casting technique: (d), (e) and (f) [29,80,71]. 113
Figure 56 – Anode AMFs: (a) TiO_2, (b) TiO_2-$CuO_{5\%}$, (c) TiO_2-$CuO_{10\%}$, (d) TiO_2-$CuO_{20\%}$, (e) TiO_2-$CuO_{30\%}$, (f) TiO_2-$CuO_{50\%}$ [38]. 114
Figure 57 – Anode AMFs: (a) ZnO, (b) ZnO-$CuO_{5\%}$, (c) ZnO-$CuO_{10\%}$, (d) ZnO-$CuO_{20\%}$, (e) ZnO-$CuO_{30\%}$. (f) ZnO-$CuO_{50\%}$ [38]. 115
Figure 58 – Pt cathode (AFM) [38]. 116
Figure 59 – J-V curves of CuO doping in TiO_2 and ZnO: (a) no doping, (b) 5%, (c) 10%, (d) 20%, (e) 30%, and (f) 50% [38]. 118
Figure 60 – P-V curves of CuO doping in TiO_2 and ZnO: (a) no doping, (b) 5%, (c) 10%, (d) 20%, (e) 30%, and (f) 50% [38]. 124

Figure 61 – Photovoltaic parameters: (a) J_{SC}, (b) FF and (c) V_{OC}. 130
Figure 62 – Solar conversion efficiencies. 131
Figure 63 – EIS curves of CuO doping in TiO_2 and ZnO: (a) no doping, (b) 5%, (c) 10%, (d) 20%, (e) 30%, and (f) 50% [38]. 135
Figure 64 – Corresponding equivalent circuit [38]. 137
Figure 65 – Series model of the DSSC circuits associated with the impedances. 139
Figure 66 – (a) Randles circuit and (b) Randles frequency response for the Nyquist diagram. Adapted from: [99]. 140

LIST OF TABLES

Table 1 - Approximate wavelength ranges [16]. 22
Table 2 - Percentage ratio between the crystalline and amorphous parts of the samples.
..... 97
Table 3 - Semi-quantitative percentage of compounds in the samples. 97
Table 4 - Samples analyzed (X-ray fluorescence). 99
Table 5 - Oxide concentration in the analyzed samples. 103
Table 6 - Comparison of the electrical parameters obtained in this work, shown in ... 132
Table 7 - Values of each element of the equivalent circuit with their associated errors.
..... 137

LIST OF ABBREVIATIONS

AFM – Atomic Force Microscopy

AMF – Atomic Morphological Features

ATR – Attenuated Total Reflectance

BG – Black Grape

CEFET – Centro Federal de Educação Tecnológica Celso Suckow da Fonseca

COPPE/UFRJ – Instituto Alberto Luiz Coimbra de Pós-Graduação e Pesquisa em Engenharia da Universidade Federal do Rio de Janeiro

DC – Direct Current

DSSC – Dye-Sensitized Solar Cell

EIS – Electrochemical Impedance Spectroscopy

FF – Fill Factor

FTIR – Fourier Transform Infrared Spectroscopy

FTO – Fluorine-doped Tin Oxide

HOMO – Highest Occupied Molecular Orbital

IMPS – Intensity Modulated Photocurrent Spectroscopy

IMVS – Intensity Modulated Photovoltage Spectroscopy

J–V – Current Density–Voltage Curve

LaFEA – Laboratório de Física Experimental e Aplicada

LUMO – Lowest Unoccupied Molecular Orbital

NanoFAB – Laboratório Multiusuário de Nanofabricação e Caracterização de Nanomateriais

NLR – National Laboratory of the Rockies

P–V – Power–Voltage Curve

RPM – Rotação por Minuto

SEM – Scanning electron microscopy

UERJ – Universidade do Estado do Rio de Janeiro

UV–Vis – Ultraviolet–Visible Spectroscopy

V.L. – Vitis labrusca (natural dye)

XRD – X-ray Diffraction

XRF – X-ray Fluorescence

LIST OF SYMBOLS

C – Capacitance (F)

Cdl – Double-layer capacitance (F)

CdTe – Cadmium telluride

CIGS – Copper-Indium-Gallium-Selenium

CO_2 – Carbon Dioxide

CuO – Copper Oxide

D – Diffusion coefficient ($cm^2 \cdot s^{-1}$)

E_Fn – Quasi-Fermi level of electrons (eV)

E_redox – Redox potential of the electrolyte (eV)

e^- – Electron

f – Frequency (Hz)

FF – Fill factor (dimensionless)

GaAs – Gallium arsenide

hν – Photon energy

I – Electric current (A)

I(t) – Time-dependent electric current (A)

I_0 – Amplitude of current response (A)

I^- – Iodeto

I_3^- – Triiodeto

Imáx – Maximum electric current (A)

J – Current density ($A \cdot cm^{-2}$)

J_0 – Saturation current density ($A \cdot cm^{-2}$)

Jsc – Short-circuit current density ($A \cdot cm^{-2}$)

kWh/m^2 – Kilowatt-hour per square meter

mA/cm^2 – Milliampere per square centimeter

MHz – Megahertz

mW/cm^2 – Milliwatts per square centimeter

nm – Nanometer

O_2 – Oxygen

P – Output power (W)

Pin – Incident light power density ($W \cdot cm^{-2}$)

Pmax – Maximum output power (W)

Pt – Platinum

R – Electrical resistance (Ω)

Rct – Charge transfer resistance (Ω)

Re – Electrolyte resistance (Ω)

Rs – Series resistance (Ω)

Si – Silicon

TiO_2 – Titanium dioxide

TiO_2–CuO – Titanium Dioxide–Copper Oxide

V – Voltage (V)

V(t) – Time-dependent applied voltage (V)

V_0 – Amplitude of applied voltage (V)

Vmáx – Maximum electrical voltage (V)

Voc – Open-circuit voltage (V)

W – Watt

Z – Complex impedance (Ω)

Z′ (Zre) – Real part of impedance (Ω)

Z″ (Zim) – Imaginary part of impedance (Ω)

Z_1 – Interfacial impedance (Ω)

Z_2 – Substrate/contact impedance (Ω)

Zw – Warburg impedance (Ω)

ZnO – Zinc oxide

a-Si:H – Hydrogenated amorphous silicon

ºC – Celsius degree

µHz – Microhertz

µm – Micrometer

η – Power conversion efficiency (%)

φ – Phase difference between voltage and current (rad)

ω – Angular frequency ($rad \cdot s^{-1}$)

Ω – Ohm

SUMMARY

1 Introduction 19

1.1 Solar Resource 21

1.1.1 Earth's Energy Balance 23

1.1.2 Spatial Distribution of Solar Energy 24

1.2 Evolution of Photovoltaic Cells 26

1.3 Motivation 31

1.4 Objectives 32

1.5 Solar Cell Generations 33

2 Experimental Procedure 38

2.1 Components of DSSCs 38

2.2 Materials and Methods 39

2.3 Preparation of the Dye 40

2.4 Anode Preparation 41

2.5 Cathode Preparation 43

2.6 DSSC Assembly 44

2.7 Operating Principle 46

2.8 Effects of CuO Doping on TiO_2 and ZnO Electrodes 51

3 Characterization Techniques 54

3.1 Optical Characterization 55

3.1.1 Fourier Transform Infrared Spectroscopy (FTIR) 55

3.1.2 Ultraviolet-Visible (UV-VIS) Absorption Spectrophotometry 57

3.2 Structural and Morphological Characterization 61

3.2.1 X-ray Diffraction (XRD) 61

3.2.2 X-ray Fluorescence (XRF) 66

3.2.3 Scanning Electron Microscopy (SEM) 70

3.2.4 Atomic Force Microscopy (AFM) 73

3.3 Electrochemical Characterization 75

3.3.1 Characteristic Curves of Photovoltaic Cells (J-V) and (P-V) 77

3.3.2 Electrochemical Impedance Spectroscopy (EIS) 80

4 Results and Discussion 84

4.1 Transmittance (FTIR) 84

4.2 Absorbance (UV-VIS) 88

4.3 Counts (XRD) 92

4.4 Photon Intensity (XRF) 98
4.5 Surface Morphology (SEM) 103
4.6 Electrode Structures (AFM) 112
4.7 Current Density (J-V Curve) 117
4.8 Power (P-V Curve) 123
4.9 Photovoltaic Parameters (Jsc, FF, Voc, η) 129
4.10 Impedance of DSSCs (EIS) 133
5 Conclusion and Future Work 142
5.1 Final Considerations 142
5.2 Future Work 143
References 144

1 Introduction

The increase in the world's population and the technological advances of civilizations have resulted in an exponential growth in the search for new sources of electrical energy capable of matching this demand [1]. Although fossil fuels are not sustainable and present serious environmental and health problems, they are still very common in the energy sector [2]. Greenhouse gases, such as methane, carbon dioxide and nitrous oxide, are emitted in large quantities during the combustion process of fossil fuels [3].

Different forms of renewable energy, such as biomass, wind, hydroelectric, marine, geothermal and solar, are recognized as alternatives to traditional sources [4]. Among the alternative sources mentioned, photovoltaic solar energy stands out for revealing immense potential, especially in tropical and subtropical countries. In the specific context of Brazil, its geographical position offers a significant advantage in this scenario. The country is located among tropical countries, standing out in a privileged way due to its “proximity” to the Equator [5].

This location gives Brazil a high incidence of solar irradiation throughout the day, with substantial values ranging from 4.25 kWh/m^2 to 6.5 kWh/m^2 [6]. It is noteworthy that this solar radiation is abundant throughout practically the entire year, characterizing the region as conducive to the implementation of technologies aimed at converting solar energy into electricity. These characteristics point to photovoltaic solar energy as an effective and sustainable alternative to meet the country's energy demands [6,7].

Most of the solar radiation that reaches the Earth's surface has a wavelength between 300–2500 nm, encompassing UV light (<380 nm), visible light (380–780 nm, also known as sunlight), and near-infrared light (>780 nm) [8]. As represented in Figure 1, the solar spectrum is composed of 3% to 5% UV light, 42% to 43% visible light, and 52% to 55% near-infrared light [9]. Irradiance at the Earth's surface is lower than at the top of the atmosphere due to the scattering and absorption of light by certain gas molecules (N_2, O_2, H_2O, CO_2). The average global solar irradiance is estimated to be approximately 1,365 W/m^2 in a 24 hour day throughout the year [9,10].

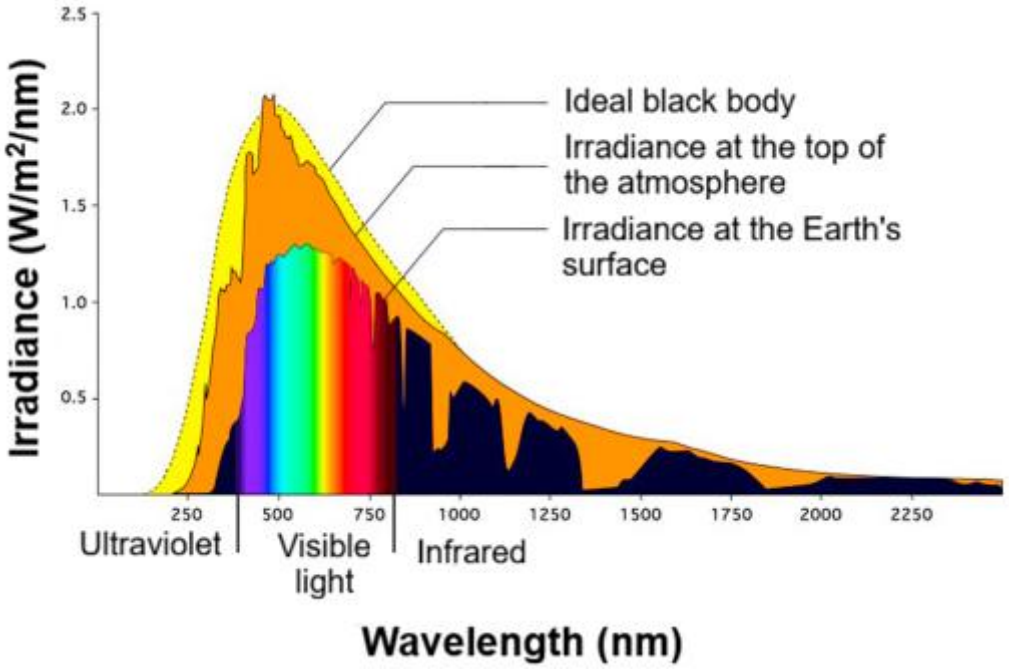


Figure 1 - Solar radiation spectrum. Adapted from: [10].

The current state of greenhouse gases and the expected state (if there are no changes in energy sources) will result in unfavorable climate changes, serious health problems, rising sea levels, changes in the ecosystem, among others [10,11]. These conditions resulting from fossil fuels represent a threat to life throughout planet Earth [11].

Based on these facts, governments began to review their energy strategies and policies to minimize these problems. Some suggestions were proposed to reduce greenhouse gases and related issues, partially or totally, such as improving the efficiency of current technologies and/or developing new devices that are efficient and have lower environmental impacts [10-12].

Given this context, this work aimed to develop new energy-generating devices in a sustainable manner, utilizing the most recent technology in the field of electrical energy conversion achieved through the photovoltaic effect (Emerging Third-Generation Solar Cells), specifically through Dye-Sensitized Solar Cells (DSSCs), also known as Grätzel Solar Cells [11-13].

To ensure a proper understanding of the topics covered, this thesis has been divided into five chapters. The first chapter introduces the subject, highlighting the

relevance of new research on renewable energy sources in the face of increasing energy demand over the years. Furthermore, it provides a concise summary of the evolution of various existing solar cells, from their initial conception to the present day.

In the second chapter, all the materials and methods employed are presented, along with a detailed description of all the experimental procedures performed for the assembly of the DSSCs. The third chapter presents the instruments and characterization techniques used. The fourth chapter addresses the results obtained, offering an analysis through morphological, structural, optical, and electrochemical characterizations. Finally, in the fifth chapter, the final considerations are presented and perspectives for future work are pointed out.

1.1 Solar Resource

The Sun, as shown in Figure 2, plays a fundamental role as a source of light and heat for life on Earth. Its energy is transmitted to our planet and others in the Solar System by means of electromagnetic waves [12,13].

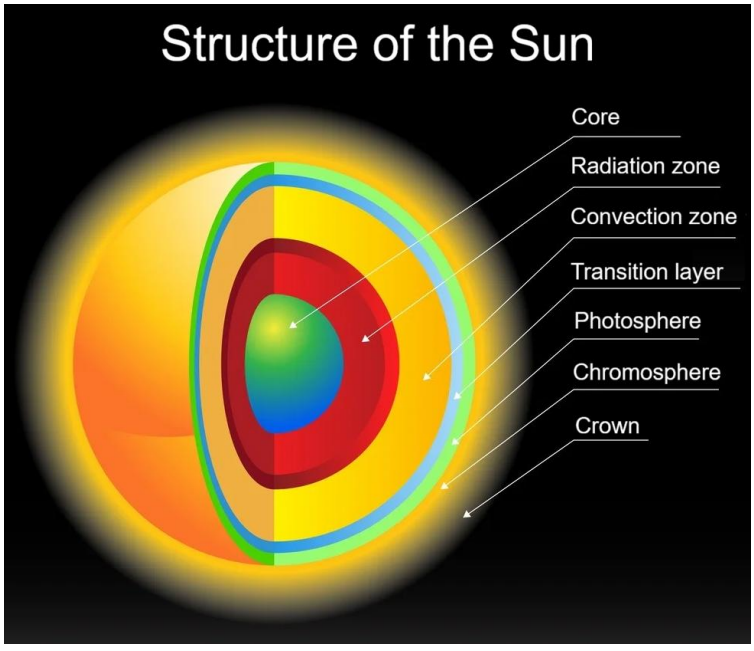


Figure 2 - Structure of the Sun. Adapted from: [14].

This radiation includes visible and near-visible radiation, as well as ultraviolet and near-infrared radiation, emitted by the Sun. Terrestrial radiation refers to infrared

radiation released by the Earth's atmosphere. The distinct regions of these radiations are characterized by their wavelength ranges within the broad range of 0.20 μm to 100.00 μm [15].

The constituent elements of solar and terrestrial radiation, along with their approximate wavelength ranges, can be seen below in Table 1:

Table 1 - Approximate wavelength ranges [16].

Wavelength range (nm)	**Spectrophotometry class**
100 – 200	Far ultraviolet
200 – 380	Near ultraviolet
380 – 780	Visible
780 – 3000	Near-infrared

Figure 3 provides a better understanding of the electromagnetic spectrum of solar and terrestrial radiation [16,17].

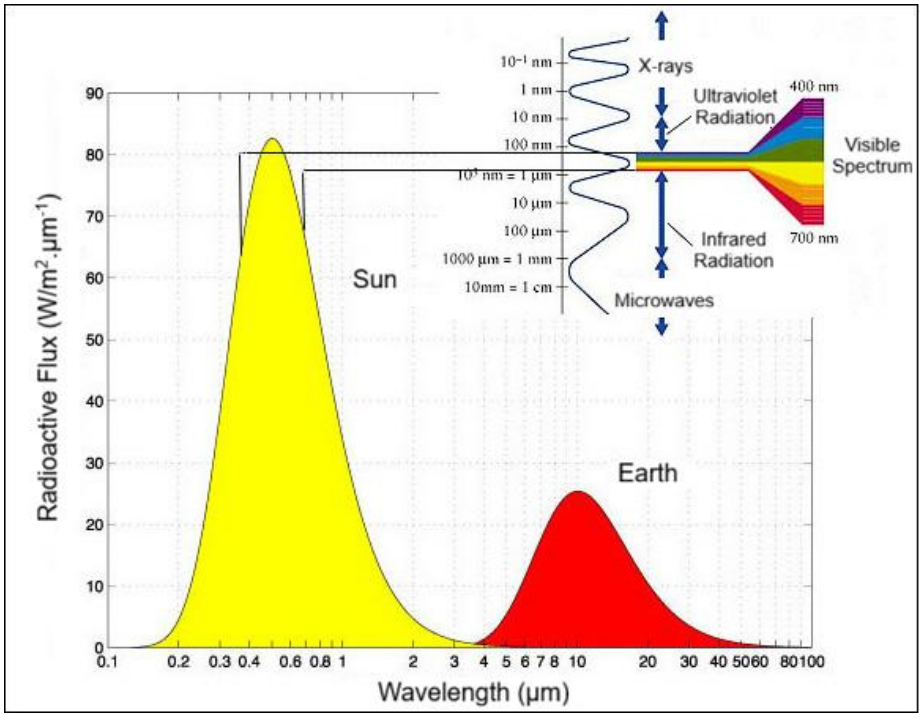


Figure 3 – Electromagnetic spectrum of solar and terrestrial radiation. Adapted from: [17].

The main emphasis here is on shortwave solar radiation. About 99% of the solar radiation that reaches the Earth's surface is concentrated in the 300 nm to 3,000 nm range of the solar spectrum [17].

In the upper layer of the Earth's atmosphere, solar irradiance has an approximate intensity of 1,360.8 ± 0.5 W/m² [16, 17]. This value, known as Total Solar Irradiance (TSI), represents the intensity of solar radiation at the top of the Earth's atmosphere, considering the average Earth-Sun distance [15,16]. It is worth noting that, although it was erroneously called the Solar Constant for several years, the correct designation is Total Solar Irradiance.

Since 2003, TSI has been meticulously measured by the Total Irradiance Monitor (TIM) instrument, which was launched by the National Aeronautics and Space Administration (NASA) aboard the Solar Radiation and Climate Experiment (SORCE) [18]. TSI measurements taken by TIM monitor sunlight incident on the top of the Earth's atmosphere using an active cavity radiometer at ambient temperature [16,18]. The results of TSI measurements performed by TIM reveal that the value of solar irradiance incident at the top of the Earth's atmosphere is not constant.

In other words, the solar irradiance incident on the top of the Earth's atmosphere can no longer be called the Solar Constant, as was the case until a few years ago. The most accurate value of the current TSI is 1,360.8 ± 0.5 W/m², dated 2008, in contrast to previous estimates from the 1990s, which pointed to 1,365.4 ± 1.3 W/m² [17,18].

1.1.1 Earth's Energy Balance

On the Earth's surface, on a cloudless day at midday, direct solar radiation reaches approximately 1,000 W/m² in many regions [18]. Although the availability of solar energy is influenced by location (including latitude and elevation), season, and time of day, the main elements affecting the availability of incident solar energy on the Earth's surface are the presence of clouds and other meteorological conditions. In turn, these predominant elements also vary according to location and time period. Figure 4 presents the Earth's Energy Balance.

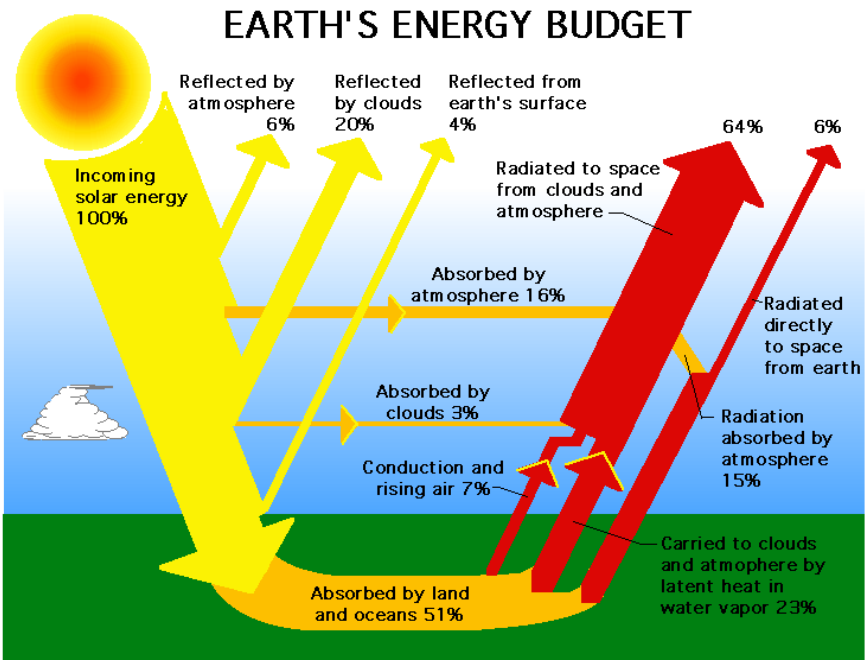


Figure 4 - Earth's Energy Balance. Adapted from: [19].

The total solar irradiance incident on the top of the Earth's atmosphere is reduced before reaching the Earth's surface as follows: reflected by clouds (20%), reflected by the atmosphere (6%), absorbed by clouds (3%), and absorbed by the atmosphere (16%). The portion of solar irradiance that reaches the Earth's surface (55%) is reflected by the Earth's surface (4%) and absorbed by the land and oceans (51%) [17,18].

1.1.2 Spatial Distribution of Solar Energy

The global map of the spatial distribution of potential solar energy, developed by NASA, can be seen in Figure 5, highlighting the extensive geographical variation of solar resources on a global scale.

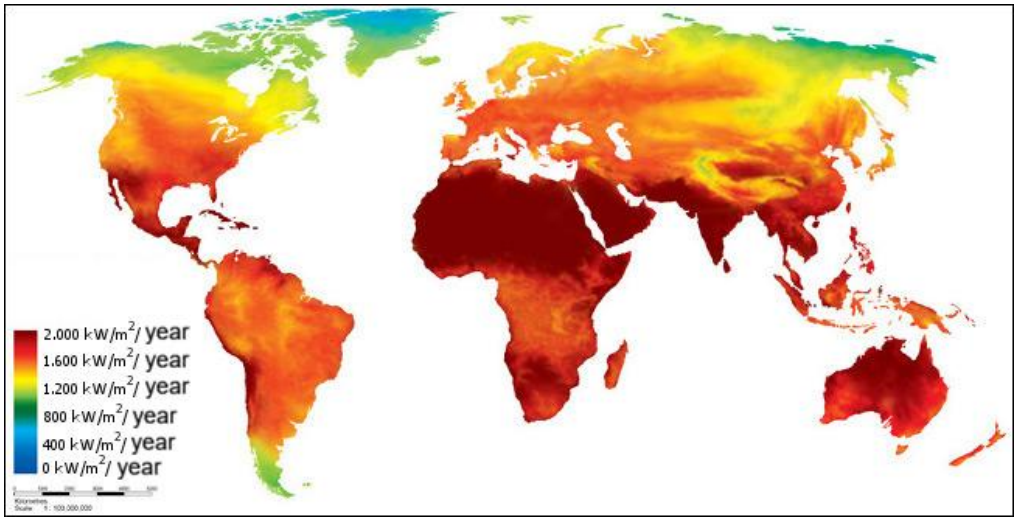


Figure 5 - World map of the spatial distribution of solar energy. Adapted from: [20].

This variation occurs due to the factors mentioned in the Earth's Energy Balance, among several others. Given that the main elements impacting the availability of solar energy on the Earth's surface are cloud cover and other meteorological conditions, Figure 6 shows a graph with data from solar irradiance measurements. This graph illustrates the effect of the reduction in incident solar irradiance due to various atmospheric conditions, highlighting mainly variations in cloud cover.

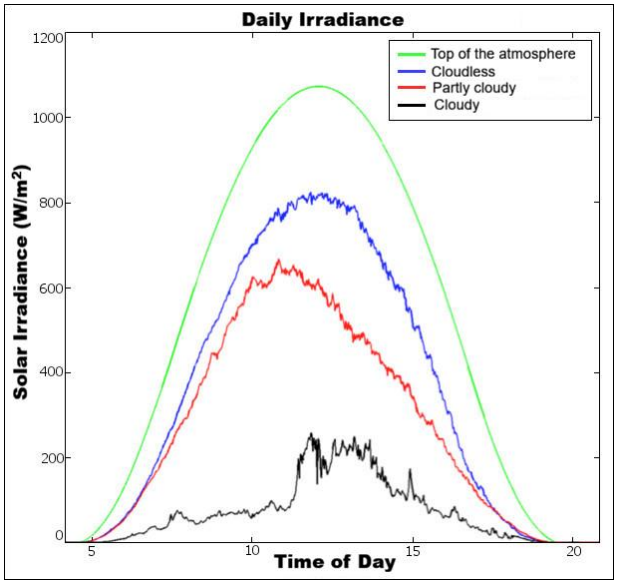


Figure 6 – Solar irradiance throughout the day. Adapted from: [21].

Due to the diverse factors influencing the availability of solar resources on the Earth's surface, obtaining the most precise possible determination of the amount of solar irradiance incident on a given location becomes crucial. This is essential for proper use in power generation systems, engineering projects, and other applications.

1.2 Evolution of Photovoltaic Cells

The evolution of photovoltaic cells reflects the continuous advancement of materials science and energy engineering in the search for more efficient and accessible renewable energy sources. From the first silicon cells developed in the 1950s, with initial applications in space systems, to third-generation technologies such as organic cells, perovskite cells[1] [8], and dye-sensitized solar cells, significant progress has been observed in terms of efficiency, cost, and versatility. This development has been driven by the global need to reduce carbon emissions and diversify the energy matrix, consolidating solar energy as one of the main sustainable alternatives for the future. [22]. Figure 7 shows the basic principle of a photovoltaic cell.

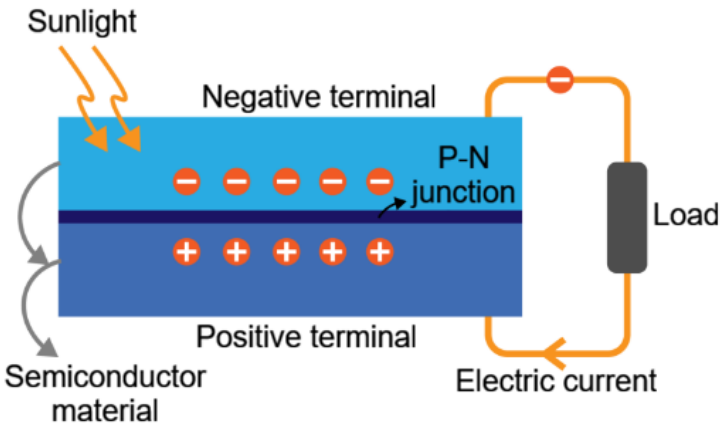


Figure 7 - Basic principle of a photovoltaic cell. Adapted from: [23].

The evolutionary trajectory of photovoltaic cells can be divided into different technological generations, each one marked by significant advances in performance,

[1] Perovskite solar cells are photovoltaic devices that employ semiconductor materials with a perovskite-type crystal structure (typically hybrid organic-inorganic or fully inorganic halides), characterized by a high optical absorption coefficient, long charge-carrier diffusion length, and optoelectronic properties favorable for the efficient conversion of solar radiation into electrical energy [8].

cost, and applicability. First-generation cells, based primarily on crystalline silicon (monocrystalline and polycrystalline), dominated the market for decades due to their high efficiency and stability. However, the high production costs and energy consumption associated with silicon refining have driven the development of more economical alternatives [22,23].

In this context, second-generation cells, known as thin-film cells, emerged, using materials such as cadmium telluride (CdTe) and copper-indium-gallium disulfide (CIGS) [10]. These technologies have significantly reduced manufacturing costs and allowed for greater application flexibility, although they generally exhibit lower efficiencies than crystalline silicon cells. Even so, they represent an important advance in democratizing the use of solar energy [15,21].

More recently, third-generation cells have stood out for introducing new physicochemical concepts and innovative materials. Among them, dye-sensitized solar cells (DSSCs), organic cells, and perovskite cells stand out [12,13]. These technologies seek not only to reduce costs but also to explore properties such as transparency, lightness, and mechanical flexibility. In the case of DSSCs, for example, there is a direct inspiration from natural photosynthesis processes, using dyes for light absorption and semiconductors such as TiO_2 for electron transport [22-24].

Following these discoveries, several researchers developed studies on the subject, culminating in 1954 when the American chemist Calvin Souther Fuller, along with his colleagues Gerald Pearson (physicist) and Daryl Chapin (engineer), created a diffusion method in cells. This process involved introducing impurities into silicon crystals, allowing control of their electrical properties [15,22]. Thus, the first silicon solar cell emerged, which has since become widely recognized globally, being the most commercially available and mass-produced solar cell.

Over time, there has also been a continuous effort to improve energy efficiency through strategies such as semiconductor doping, interface engineering, electrolyte optimization, and the development of new photoactive materials. Furthermore, recent research has explored hybrid architectures and tandem devices, which combine different materials and conversion mechanisms to overcome the theoretical limitations of conventional Technologies [14,19].

Thus, the evolution of photovoltaic cells demonstrates a transition from robust, yet rigid and costly systems, to increasingly versatile, efficient and economically viable devices, keeping pace with contemporary demands for sustainability and technological innovation [20-22].

To achieve this feat, the researchers developed a silicon rod doped with a minimal concentration of gallium, giving it conductivity. In this way, the mobile charges became positive (positive "P" type silicon). The rod was then immersed in a hot lithium bath, resulting in an excess of free electrons on the surface of the rod, which became carriers with negative charges (negative "N" type silicon). When two semiconductors of these two types ("P" and "N") are joined in a way that maintains the continuity of the crystal lattice, the so-called "P-N junction" is formed [22,24], as illustrated in Figure 8.

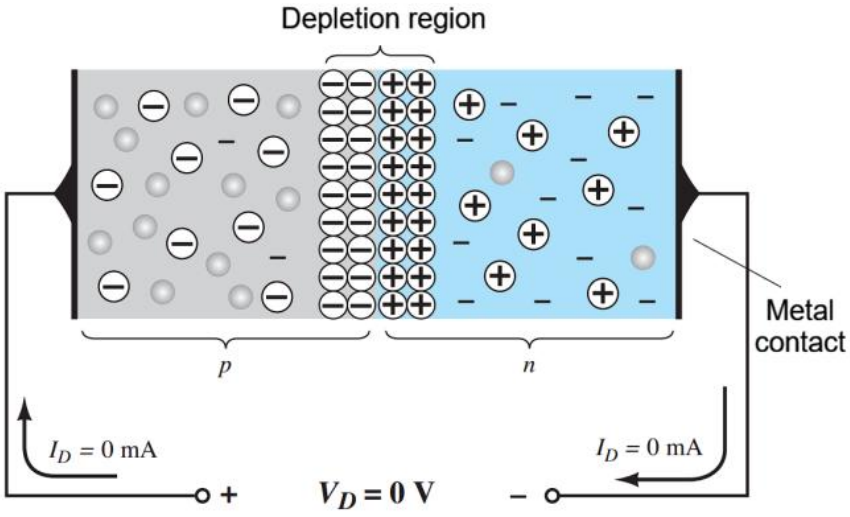


Figure 8 - P-N junction. Adapted from: [25].

Figure 8 represents the p-n junction in equilibrium, that is, without the application of an external voltage (VD = 0 V) and without net current flow (ID = 0 mA). This is one of the most important structures in the history of photovoltaic cells, since it was precisely the physical mastery of this type of junction that allowed the development of silicon solar cells, especially the first generation, which marked the beginning of modern photovoltaic conversion [18,25].

The region on the left, identified as p-type material, has holes as its majority carriers, while the region on the right, identified as n-type material, has electrons as its

majority carriers [20,23]. This occurs because, in the p-type semiconductor, acceptor dopant atoms are introduced, creating an electron deficiency in the crystal lattice, while in the n-type semiconductor, donor dopants are introduced, providing extra electrons. When these two materials come into contact, a spontaneous charge diffusion process is established: electrons from the n-side tend to migrate to the p-side, where their concentration is lower, and holes from the p-side tend to migrate to the n-side, for the same reason [22-25].

However, this initial diffusion does not remain indefinitely. As electrons and holes cross the interface, they recombine near the junction, leaving behind fixed, non-mobile ions in the crystal lattice: on the n-side remain positive charges from ionized donors, and on the p-side remain negative charges from ionized acceptors [23]. The accumulation of these fixed charges forms the so-called depletion region or space charge region, indicated in the center of the figure. This region is so named because there is a significant reduction in free carriers. As a consequence, an internal electric field arises, oriented from the n-side to the p-side, which opposes the diffusion process [21-23].

This internal electric field generates a potential barrier, which prevents the continuation of the net diffusive flow. Thus, the equilibrium state shown in Figure 8 is established: although there are opposing trends in charge movement, the diffusion current and the drift current exactly compensate each other, resulting in zero total current [25]. This is why the image highlights VD = 0 V and ID = 0 mA. In other words, even without external voltage, the junction already possesses an extremely important internal electrostatic organization for the operation of semiconductor devices [24-26].

In the context of the evolution of photovoltaic cells, this structure was crucial. The first efficient solar cells, developed with crystalline silicon, were based precisely on a p-n junction capable of creating an internal electric field [24,25]. When light strikes the semiconductor, photons with sufficient energy promote electrons from the valence band to the conduction band, forming electron-hole pairs. If these carriers are generated near the depletion region, the internal electric field of the junction separates these charges: electrons are directed to the n-side and holes to the p-side. This separation reduces immediate recombination and allows the charges to be collected by the metallic

contacts, producing electric current in the external circuit. Therefore, the p-n junction is not just a structural detail; it constitutes the physical heart of the classic photovoltaic cell. [23-26].

Historically, the consolidation of this architecture was a milestone because it showed that it was possible to directly convert light energy into electricity using an electrically organized semiconductor material. First-generation silicon cells achieved great relevance precisely because they combined light absorption with the presence of an efficient and stable p-n junction [25]. Later, with the evolution of photovoltaic technologies, thin films and then third-generation cells, such as DSSCs, organic cells, and perovskites, emerged [27]. Although many of these newer technologies do not use exactly the same traditional p-n junction in its classic form, they all inherited the same fundamental physical principle evidenced in this figure: the need for an internal mechanism for separating photo-generated charges [22-26].

This work focuses precisely on the search for new methodologies that can continue to improve the photovoltaic performance of DSSCs. To achieve this objective, CuO doping was performed on TiO_2 and ZnO semiconductors. To avoid the use of synthetic dyes composed of heavy metals, the photosensitization of the developed cells was carried out using a natural dye extracted from black grapes (*Vitis labrusca*) due to its wide spectral absorption range related to the incident solar wavelength.

In DSSCs, for example, instead of a conventional p-n junction, there is a functional interface between the excited dye, the semiconductor, and the electrolyte, which plays the role of promoting the separation and transport of charges. In perovskite cells and certain organic heterostructures, separation occurs through interfaces between materials with suitable energy levels [26-28]. Thus, throughout the evolution of photovoltaic cells, the central concept has ceased to be exclusively the silicon p-n junction, but the principle it inaugurated has remained: absorb light, generate carriers, and efficiently separate them before they recombine.

Before presenting the experimental procedures performed, the motivation that led to the research in this work is presented below.

1.3 Motivation

As presented in previous sections, the contemporary world faces significant challenges related to the growing demand for energy, the urgent need to mitigate climate change, and the search for sustainable energy sources. In this context, Dye-Sensitized Solar Cells (DSSCs) emerge as a promising alternative for clean energy generation, offering potential advantages in terms of cost, efficiency, and versatility.

The increase in greenhouse gas emissions and the scarcity of non-renewable energy resources highlight the urgency of adopting more sustainable energy sources. DSSCs offer the possibility of converting solar energy into electricity efficiently, contributing to the reduction of dependence on fossil fuels and minimizing environmental impacts.

Despite advancements in solar cell technologies, many face challenges related to toxic materials, high production costs, and technical complexity. Grätzel Solar Cells, on the other hand, have the potential to overcome these limitations, being manufactured with abundant materials provided by nature, such as organic photosensitizers, and simpler processes, making them more accessible in terms of construction.

The pursuit of greater efficiency in solar energy conversion is a constant goal in solar cell research. DSSCs offer a promising approach by allowing sensitization with a variety of dyes, enabling adaptation to different light conditions and environments. This makes them ideal for applications in diverse geographical regions and in different contexts, from portable devices to large industrial installations.

The research and development of new DSSCs represent an opportunity to advance scientific knowledge in the field of photovoltaics. By exploring new sensitizing materials, optimizing manufacturing processes, and understanding the fundamental mechanisms of energy conversion, this research will contribute not only to sustainable electricity generation but also to scientific progress in general.

Therefore, the development of this work on new energy-generating devices through the photovoltaic effect is motivated by the pressing need for sustainable solutions to global energy challenges, offering a thesis for scientific, technological, and social innovation, aiming not only at the advancement of science but also at building a more sustainable and resilient future.

1.4 Objectives

The objective of this work was to develop twenty-four Grätzel solar cells, comparing them in relation to the photoelectrochemical conditions of each cell through the various anodic reactions performed with CuO doping in TiO_2 and ZnO semiconductors, where they are generally used in a singular manner.

The intention of doping was to improve the photovoltaic performance of each cell and, in addition, to find the gain, saturation, and optimum point curves, considering that in previous works, such as in [28], it was found that the TiO_2-CuO (50%) anodic hybrid surface presented significant efficiencies (≈ 5x >) when compared to electrodes manufactured using only TiO_2. As ZnO is also widely used in the construction of these cells, it was decided to dope it with CuO as well.

To observe the optimum point of this combination between the oxides, that is, to evaluate the best photovoltaic parameters and also the saturation, doping was carried out in proportions of 5%, 10%, 20%, 30% and 50%. Pt was chosen for the photocatalytic electrode due to the previous study [29], where the reduction reaction was satisfactorily achieved in electron capture. The anode and cathode were constructed using spin coating and drop casting techniques, respectively.

In previous studies [28,30], it was possible to observe the absorption potential present in each natural dye extracted from pitomba (*Talisia esculenta*), jiló (*Gilo group*), lantana (*Lantans repens*), tango (*Solidago canadensis*) and black grape (*Vitis labrusca*), with the latter being considered the best organic dye among . For this reason, the photosensitizer extracted from black grapes was used in twelve cells, and the others used synthetic dye (N3) for comparative performance purposes. In order to assist in electron transport and regenerate the dye, an iodine-based electrolyte (I) was used. For detailed results, structural, morphological, optical and electrochemical characterizations were performed.

It is worth noting that all references used in this section come from work developed by researchers at the Laboratory of Experimental and Applied Physics (LaFEA), CEFET/RJ (Maracanã, block D, rooms 19 A-C), coordinated by Prof. Dr. Ana Lucia Ferreira de Barros.

1.5 Solar Cell Generations

In 1991, Michael Gratzel and O'Regan developed dye-sensitized solar cells (DSSCs), which for this reason are also known as Gratzel solar cells [26]. Grätzel (1944) is a professor at the École Polytechnique Federale de Lausanne (Switzerland), where he directs the Photonics and Interfaces Laboratory.

He pioneered research on energy and electron transfer reactions in mesoscopic materials and their optoelectronic applications, and also co-invented the Grätzel cell with Brian O'Regan, pioneering the use of nanomaterials in lithium-ion batteries [26,31].

The German-Swiss materials inventor developed a new type of photovoltaic cell that is based on dyes and relies on photosynthesis. In this cell, sunlight is transformed into electrical energy with the support of organic dyes.

Grätzel has published over 800 articles, two books, and holds over 50 patents. Scientific American ranks him among the 50 most recognized scientists in the world. Known for developing groundbreaking scientific research, the scientist has received the following awards [32]:

- Harvey Award (2007);
- Balzan Award (2009);
- Millennium Technology Award (2010);
- Albert Einstein World Prize for Science (2012);
- Marcel Benoist Prize (2013);
- King Faisal International Prize (2015).

That is, 14 years ago, Grätzel received the Millennium Technology Prize for the invention of dye-sensitized solar cells (DSSCs), valued at over US$1,000,000.00 [32].

Grätzel solar cells are a type of photovoltaic cell that converts sunlight into electricity, and as shown in Figure 9 through the graph of photovoltaic cell evolution, they belong to the group of emerging third-generation cells [33]. As an illustrative summary, Figure 9(a) presents a graph using data from the National Laboratory of the Rockies (NLR) in the United States, showing the evolution of efficiency for all types of

solar cells produced by various companies from 1975 to the present day. Meanwhile, Figure 9(b) compares first, second, and third-generation solar cells in terms of their cost-efficiency ratio.

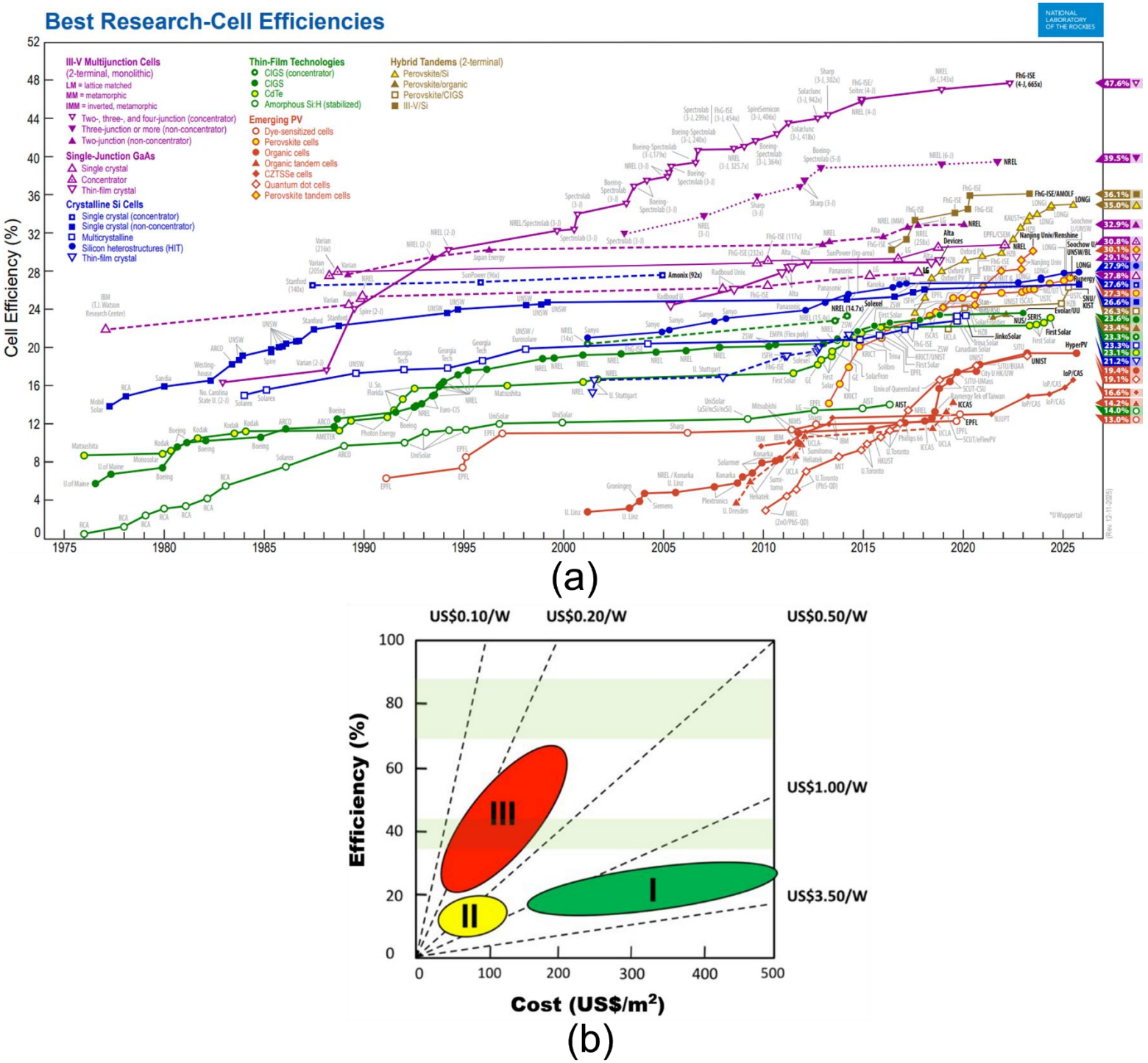


Figure 9 - (a) Evolution of solar cells and (b) Cost vs. efficiency relationship between first (I), second (II) and third generation (III) solar cells. Adapted from: [27, 33].

For better understanding, the technologies related to each generation of solar cell are described below:

- **First generation (I):** solar cells manufactured using monocrystalline or polycrystalline silicon wafers, as well as gallium arsenide. Silicon cells are predominantly used in terrestrial applications, leading the global photovoltaic market. Gallium arsenide cells, on the other hand, are restricted to space applications due to their high costs [34];
- **Second generation (II):** thin-film solar cells, which can be composed of amorphous silicon, cadmium telluride (CdTe), or copper indium gallium diselenide ($CuInGaSe_2$). These cells also have terrestrial applications and are a few μm (micrometers) thick [34,35];
- **Third generation (III):** the most recent solar cell manufacturing technology, represented by organic cells, Grätzel solar cells (DSSCs), and multijunction cells. Because they are still relatively new technologies, organic solar cells are mostly found in university laboratories and sustainable energy research centers, such as LaFEA, which conducts research to improve this technology and achieve better photovoltaic performance. This is also why this work is so important. Multijunction solar cells have high efficiencies but high manufacturing costs, and therefore their application is restricted to the space sector or in systems with solar concentrators for terrestrial use [35,36].

Among the technologies presented, the one that currently holds the leading position in the global photovoltaic market is crystalline silicon-based solar cells (first generation), accounting for approximately 90% of modules sold. This significant share is due to several factors, including the abundance of silicon in nature, the broad technological mastery by various countries, the presence of a consolidated production industry, and absorption characteristics that efficiently align with the solar spectrum [34-36].

As shown in Figure 9(b), DSSCs emerge as a potential technology to meet the cost vs. efficiency condition, considering that currently marketed silicon solar panels are

relatively expensive and do not present such high efficiencies (≈ 25%) when compared to emerging third-generation solar cells.

The operating principle of Grätzel solar cells basically consists of a photoelectrochemical process, where sunlight is absorbed by a sensitizing dye that absorbs light photons and generates excited electrons, which are then injected normally into the TiO_2 (titanium dioxide) layer that coats the electrode [26]. In this way, the excited electrons flow through the external circuit, generating an electric current. In Chapter 2 this operating principle will be explained in more detail.

DSSCs are a photovoltaic technology that offers an alternative to traditional silicon cells. They have unique characteristics that bring both benefits and limitations. [26,37]:

Advantages:

- Good performance in low light: they work very well in diffused light or indoor environments, maintain reasonable efficiency even on cloudy days, ideal for IoT devices, sensors, etc;
- Low production cost: they utilize inexpensive materials such as TiO_2 and organic dyes, simple manufacturing processes (they do not require high purity like silicon), they can be produced using low-cost techniques (ex: printing);
- Flexibility and aesthetics: they can be colored or transparent, applicable to windows, facades, and architectural design, possibility of flexible substrates,
- Less sensitive to defects: it does not require perfect crystallinity like silicon cells, less impact of impurities on performance.

Disadvantages:

- Low efficiency compared to silicon: efficiency: ~7–12%, silicon cells easily exceed 20%;
- Stability problems: the liquid electrolyte may leak or degrade, it is sensitive to temperature and UV radiation, and it has a shorter lifespan than conventional technologies;
- Difficult sealing and encapsulation: the need for efficient sealing to prevent electrolyte evaporation;
- Limited performance at high temperatures: efficiency may decrease with

increasing temperature.

In order to overcome the aforementioned challenges, the search for new methodologies regarding DSSCs becomes essential, as these offer an innovative approach to converting solar energy into electricity, emphasizing flexibility and lower production costs.

As shown in Figure 9(a), DSSCs belong to the group of emerging photovoltaic technologies traditionally classified as third-generation. However, it is observed that their conversion efficiency remains significantly lower than that of crystalline silicon technologies, more established thin-film technologies, and, notably, multi-junction cells. While the latter already exceed 45% efficiency under laboratory conditions, DSSCs exhibit maximum efficiencies of around 11%, demonstrating that classification as a third-generation technology does not necessarily imply high efficiency levels.

This apparent contradiction stems from the fact that the classification of photovoltaic generations is linked to the operating principle, the materials used, and the technological strategy adopted to reduce manufacturing costs and enhance production sustainability rather than exclusively to energy performance. DSSCs were designed to leverage low-cost manufacturing processes, abundant materials, mechanical flexibility, and good performance under diffuse light and in indoor environments; these characteristics make them promising for specific applications, despite their lower efficiencies compared to more mature photovoltaic technologies.

Figure 9(b) reinforces this interpretation by illustrating the relationship between efficiency and cost. Third-generation technologies (Region III) occupy a range of higher potential efficiency and lower cost per watt compared to previous generations. However, this region represents a technological goal and development potential; it does not imply that all third-generation technologies have already simultaneously achieved high levels of efficiency.

DSSCs are a clear example of this situation: although classified as third-generation cells, their current stage of development still prioritizes advantages such as low cost, manufacturing simplicity, and suitability for low-irradiance conditions, at the expense of achieving the highest conversion efficiencies.

2 Experimental Procedure

This chapter describes the materials and methods used in each phase of DSSC construction, covering the preparation of the dye, anode, cathode, electrolyte, and finally, the assembly of the device.

2.1 Components of DSSCs

DSSCs consist of layers formed by glass substrates coated with thin films of transparent semiconducting oxides such as FTO (fluorine-doped tin oxide) or ITO (indium tin oxide) that act as electrodes. Using techniques such as spin coating or drop casting, TiO_2 and ZnO nanoparticles are deposited onto the anode to achieve high porosity and a large surface area [38]. For the photocathodic electrode, platinum-based deposits are typically used (since it is an inert electrode). This process catalyzes the electrons (reduction) from the photoanode (oxidizing electrode). Dyes are deposited on the anodic layer, acting as photosensitizers, interacting with the semiconductor oxides and maximizing absorption of the incident solar spectrum. The electrolyte, containing a redox pair, usually iodine-based (aqueous solution), is added between the two electrodes and is responsible for dye regeneration [26,38]. Figure 10 shows the components that make up the DSSCs developed in this work.

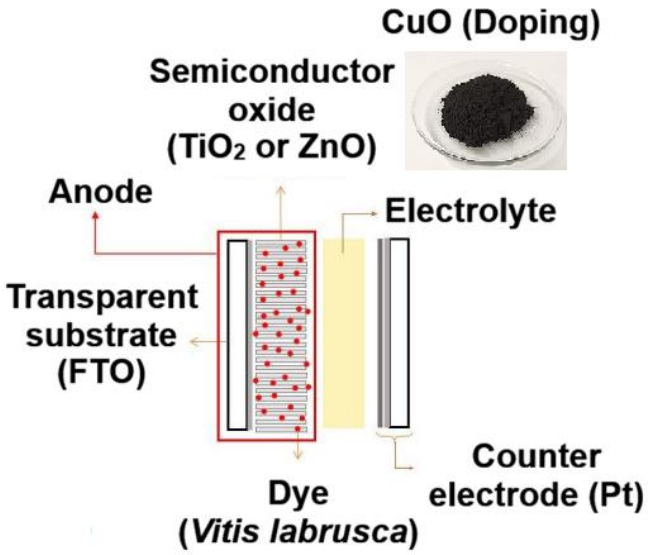


Figure 10 – Components of DSSCs [38].

2.2 Materials and Methods

For the fabrication of the solar cells, the following materials were used, acquired from Sigma-Aldrich (Louis, MO): transparent conductive thin films coated with fluorine-doped tin oxide (FTO) with a surface resistivity of approximately 10 Ω/sq and 99% purity, supplied in dimensions of 100 mm x 100 mm x 3 mm (for the construction of the DSSCs in this study, they were cut to dimensions of 2.5 cm x 2.5 cm), polyethylene glycol, titanium dioxide (≅ 20 nm), zinc oxide (≅ 23 nm), hexachloroplatinic acid, ruthenium, potassium iodide, and iodine. Chemical substances such as copper oxide (≅ 27 nm) and acetonitrile were acquired from Dinâmica Química Contemporânea (São Paulo, Brazil). Silicone adhesive (TEK BOND) and other chemicals, such as acetic acid and ethanol, were obtained from local companies (Rio de Janeiro, Brazil), with analytical grade used as received, without undergoing additional chemical processes.

To analyze the dye's transmittance, optical characterization was performed using an Agilent Cary 630 FTIR spectrometer. The absorption of the dye solution was evaluated using a SHIMADZU UV-2600i spectrophotometer. To characterize the phases of the crystalline chemical compounds and obtain the values for the 13 anodic samples, a BRUKER D2 Phaser diffractometer was used, and to qualitatively and quantitatively evaluate the concentrations using X-ray fluorescence, a commercial Epsilon 1 (Malvern Panalytical) instrument was used.

For structural characterization, an Atomic Force Microscope (AFM) was used, through the Nanosurf EasyScan 2 equipment. To obtain image results regarding the morphology of each electrode, a Scanning Electron Microscope (SEM), model JEOL JSM-7100F, was used. Finally, with the DSSCs already constructed, electrochemical characterizations were performed using a multipotentiostat (IVIUM Compactstat), simultaneously with the solar simulator (Ivisun® IVIUM Technologies). Through these instruments it was possible to obtain the electrical parameters of the DSSCs: short-circuit current density (Jsc), open-circuit voltage (Voc), fill factor (FF) and conversion efficiency (η).

2.3 Preparation of the Dye

In previous studies [28,30], it was possible to observe the absorption potential present in each natural dye extracted from pitomba (*Talisia esculenta*), jiló (*Gilo group*), lantana (*Lantana repens*), tango (*Solidago canadensis*) and black grape (*Vitis labrusca*), the latter being considered the best organic dye among these. For this reason, the photosensitizer extracted from black grape was used in all cells. In any case, Chapter 4 presents in more detail the optical conditions favorable to the choice of this natural dye.

Black grapes were obtained from a local market in Rio de Janeiro, Brazil. They were washed several times with water and then carefully peeled. The skins were then washed again with water and dried at room temperature. After drying, approximately 10 g of the skin sample was crushed using a mixer (model: M-08, COD: 3970-02), and then placed in a beaker with 50 ml of ethanol added. Over 12 hours, this mixture was able to extract the dyes. To obtain a purely liquid dye solution, the residue was separated from the skins through filtration using filter paper and a funnel. The dye was then stored at 5 °C in an airtight container. Figure 11 shows the steps described.

In order to evaluate the comparative degree of performance of DSSCs, the synthetic dye ruthenium (Ru) was used. Its preparation consists of Ru (0.03528 g) plus ethanol (100 ml).

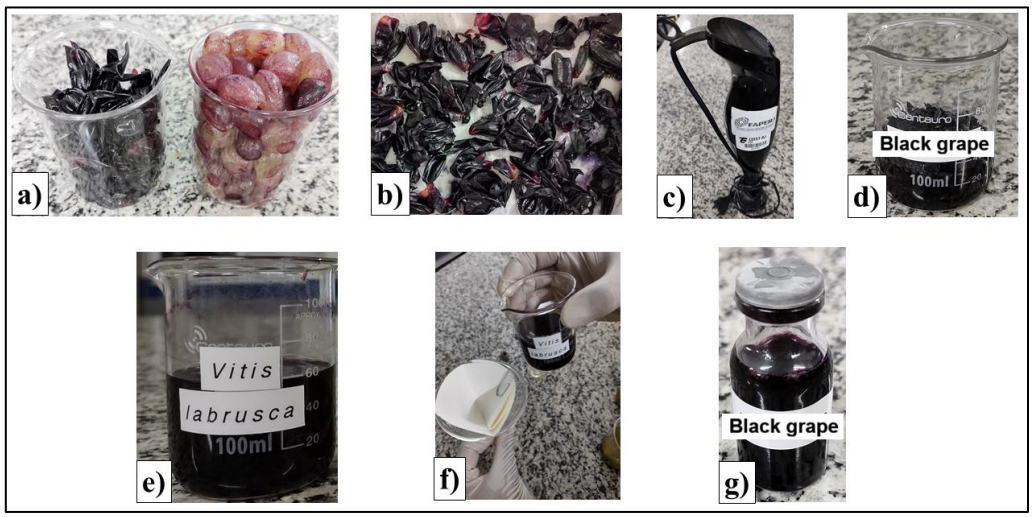


Figure 11 – Steps in the dye preparation process: (a) utilization of the peels, (b) drying, (c) crushing, (d) crushed peels, (e) dye extraction, (f) filtering, (g) finished dye.

2.4 Anode Preparation

Before starting the preparation of the solutions, the beakers used were properly washed with water and sterilized with ethanol; then, they were placed in an oven at 90 ºC for 10 minutes, thus removing any possible contamination. For this procedure, the following chemical compounds were used: polyethylene glycol (0.3 g), TiO_2 powder (1 g), ZnO (1 g), CuO (1 g), distilled water (6 ml), and acetic acid (6 ml). During the use of the oxides, the lights remained off to prevent premature oxidation due to incident photons.

Thus, TiO_2 and ZnO solutions were prepared first. The main focus of this work was the doping of the TiO_2-CuO and ZnO solutions with CuO in proportions of 5%, 10%, 20%, 30%, and 50%. After all the aforementioned chemical reagents had been added to the beakers, the solutions remained in the ultrasonic bath for 3 hours.

To obtain a uniform surface on the FTO substrate, the spin coating technique was used. The coating was applied at 1000 RPM for 10 seconds, with the rotation controlled by an Arduino. Figures 12 and 13 show, respectively, the anodic solutions and the deposition technique used to obtain the desired homogeneous surface.

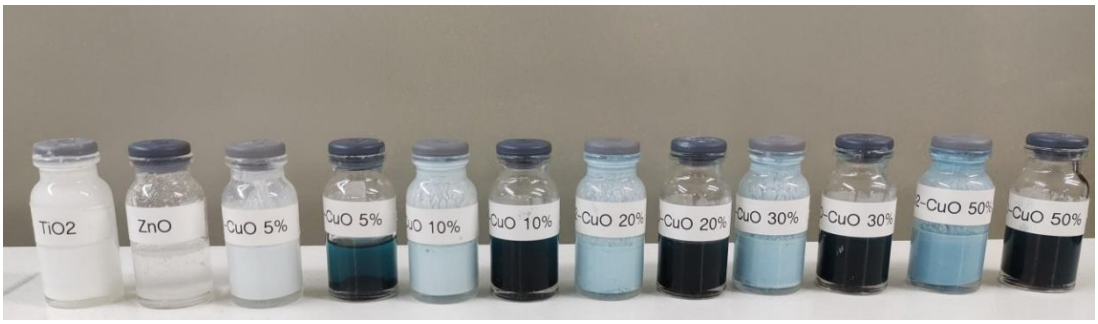


Figure 12 – Anodic solutions in different proportions.

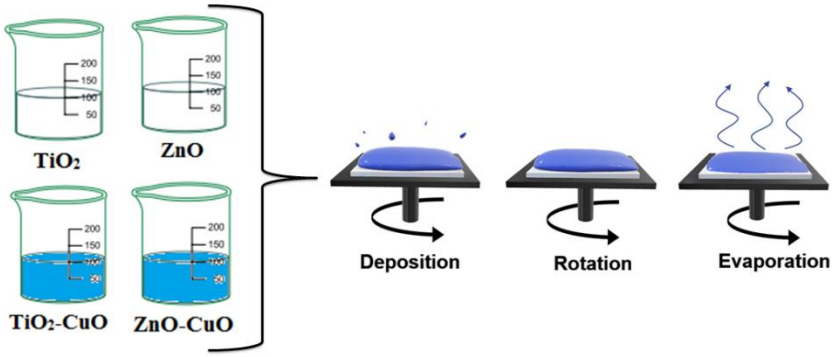


Figure 13 – Spin coating technique.

Before depositing both solutions, the surface resistivity of all FTO substrates was checked using a multimeter, observing a surface resistivity of approximately 18.5 Ω/sq. To finalize the construction of the anode, the substrates coated with TiO_2, ZnO, TiO_2-CuO, and ZnO-CuO were placed in a muffle furnace and annealed at a temperature of 450 °C for 30 minutes. After annealing, as shown in Figure 14, the twelve developed anodes can be observed.

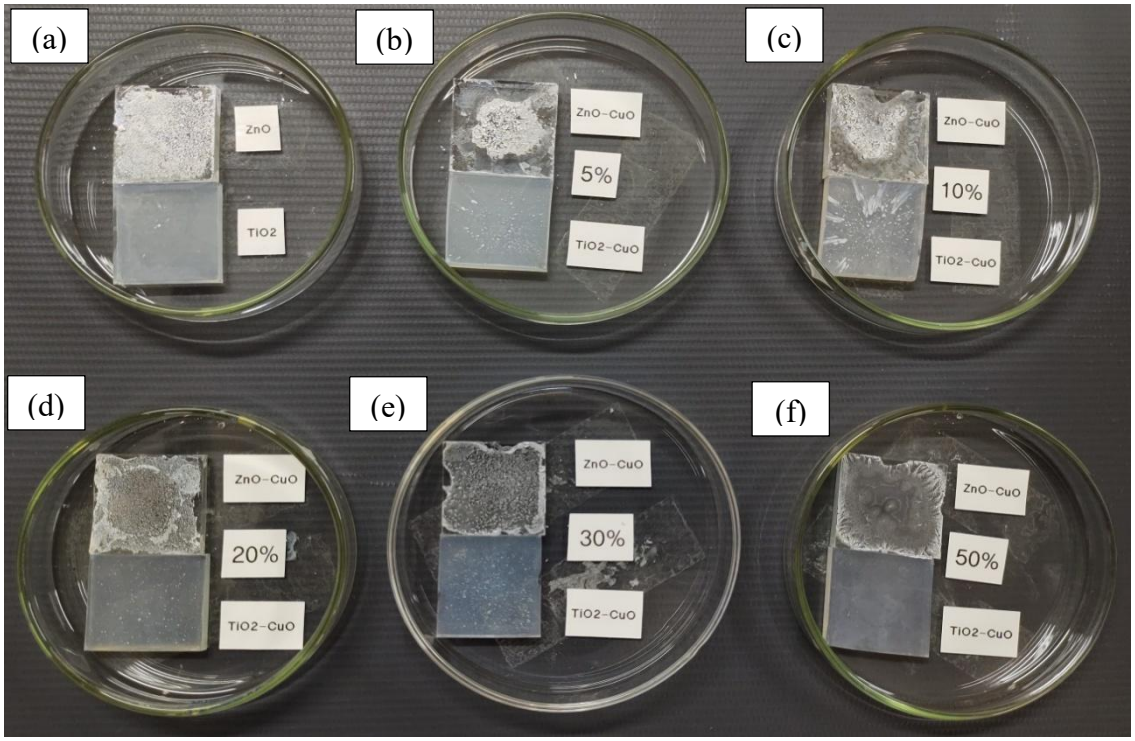


Figure 14 – Terminated anodes: (a) ZnO and TiO_2, (b) ZnO-$CuO_{5\%}$ and TiO_2-$CuO_{5\%}$, (c) ZnO-$CuO_{10\%}$ and TiO_2-$CuO_{10\%}$, (d) ZnO-$CuO_{20\%}$ and TiO_2-$CuO_{20\%}$, (e) ZnO-$CuO_{30\%}$ and TiO_2-$CuO_{30\%}$, (f) ZnO-$CuO_{50\%}$ and TiO_2-$CuO_{50\%}$.

2.5 Cathode Preparation

In this step, the beaker and test tube were sterilized before the start of the procedures. The platinum (Pt) cathode solution was used to perform the catalysis (reduction) process of the cells. For this, the Pt counter electrode was prepared using a 2 mM hexachloroplatinic acid solution ($H_2Cl_6Pt_6H_2O$). After that, the solution was placed in the ultrasonic bath and covered with distilled water for 30 min. The deposition method for this case was drop casting, where the solution droplets were poured using a micropipette in a single layer. The identification process of the FTO coating was performed in the same way as for the anode, using a multimeter. Finally, the Pt-coated substrates were placed in a muffle furnace and annealed at a temperature of 350 ºC for 30 min. Figure 15 shows the procedure performed and Figure 16 shows the finished cathodes.

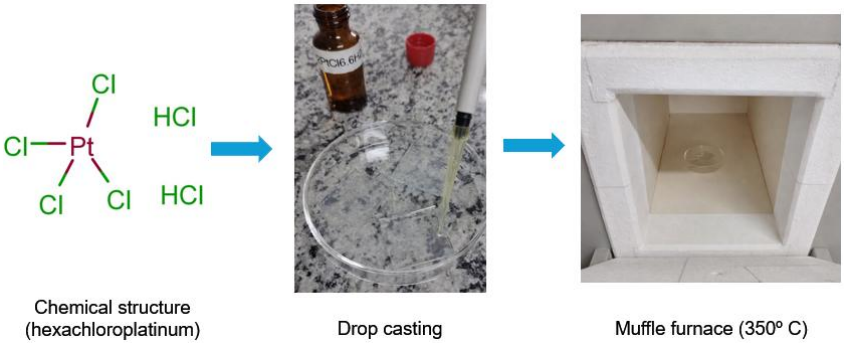


Figure 15 – Preparation of cathodes.

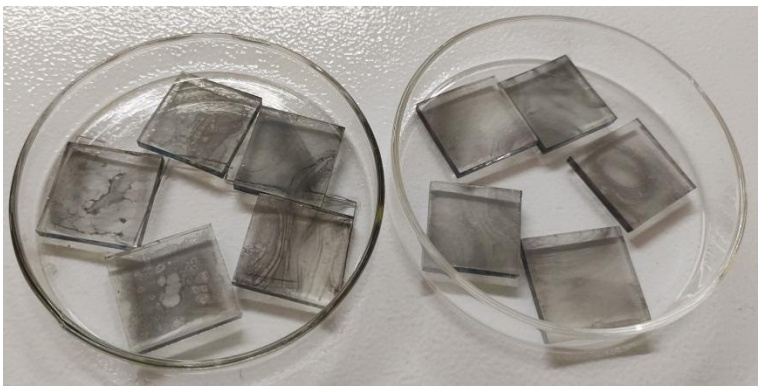


Figure 16 - Pt cathodes.

2.6 DSSC Assembly

To finalize the assembly of the photovoltaic cells, the electrodes (anodes with the dyes already deposited and cathode) were joined, and a redox electrolyte consisting of an iodine-based solution capable of assisting in electron transport was deposited between them [28]. In this work, the electrolytic solution was prepared using potassium iodide (2.075 g), iodine (0.12 g), acetonitrile (5 ml), and polyethylene glycol (0.2 g) [42-44]. Before remaining in the ultrasonic bath for 30 min, the solution was stored in an insulated container that did not allow the passage of light, thus preventing possible oxidation [28,38].

In this final assembly procedure, electrolyte injection can cause spillage outside the active area of the solar cell. When this happens, there is no effective electron transport between the device components, and thus, its efficiency decreases. Sealing prevents electrolyte leakage. To achieve this, a small amount of silicone was applied externally (without interfering with the electrochemical properties of the cells) in a horizontal track on both adjacent sides of one of the electrodes in a parallel manner. On the sides of each electrode, a small strip was left to serve as a contact for electrochemical characterization. The schematic representation of the DSSC assembly in this work can be seen in Figure 17.

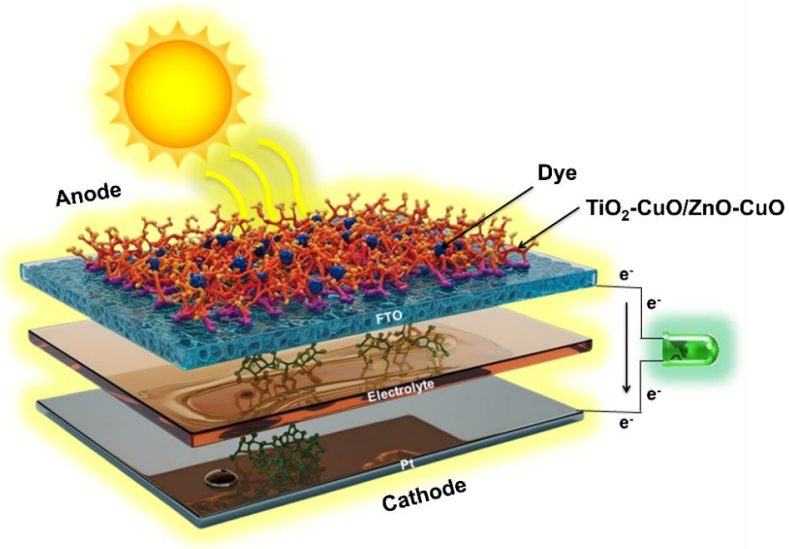


Figure 17 – DSSCs assembly diagram. Adapted from: [67].

After all the procedures have been carried out, the assembly of the developed DSSCs can be observed in Figure 18.

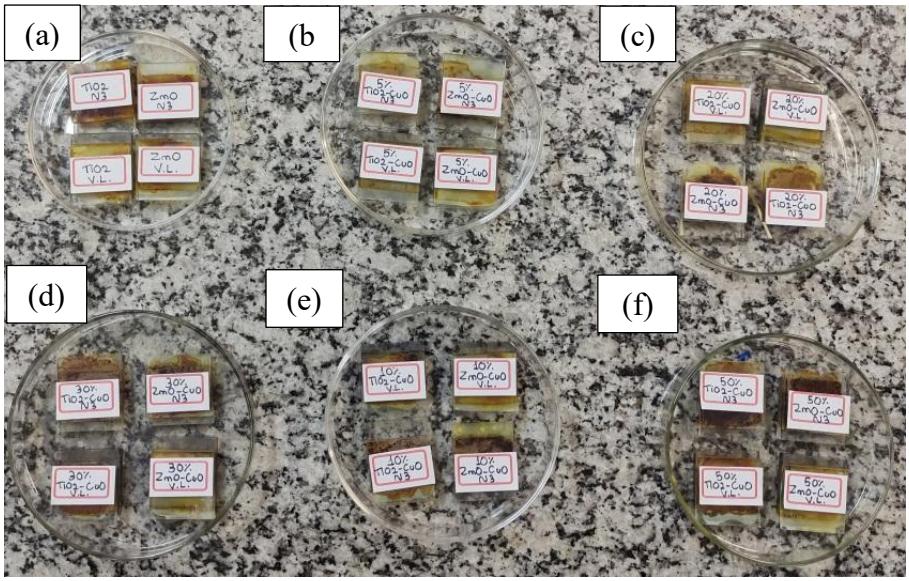


Figure 18 – Assembled DSSCs: (a) ZnO, TiO_2 (V.L. and N3), (b) ZnO-$CuO_{5\%}$, TiO_2-$CuO_{5\%}$ (V.L. and N3), (c) ZnO-$CuO_{20\%}$, TiO_2-$CuO_{20\%}$ (V.L. and N3), (d) ZnO-$CuO_{30\%}$, TiO_2-$CuO_{30\%}$ (V.L. and N3), (e) ZnO-$CuO_{10\%}$, TiO_2-$CuO_{10\%}$ (V.L. and N3), (f) ZnO-$CuO_{50\%}$, TiO_2-$CuO_{50\%}$ (V.L. and N3)

In summary, Figure 19 presents all the steps taken up to the final construction of the DSSCs, as described below:

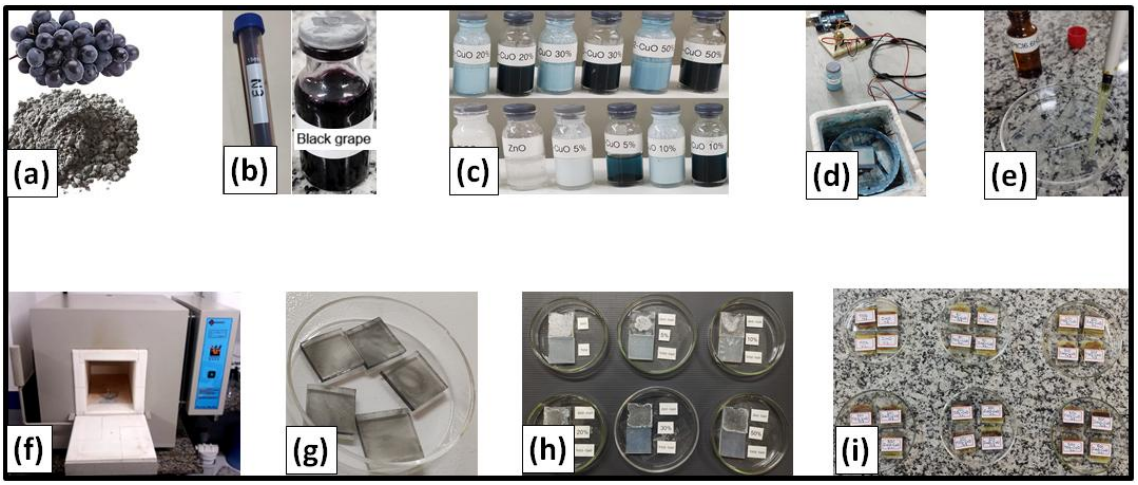


Figure 19 – Summary of the steps in constructing Grätzel cells: (a) Fruit used and Ru, (b) Dye extraction, (c) Anodic solutions, (d) Spin coating, (e) Drop casting, (f) Annealing in a muffle furnace, (g) Cathodes, (h) Anodes, and (i) DSSCs.

2.7 Operating Principle

The operation of a DSSC is based on the spatial separation between the light absorption stage and the charge transport stage. In the architecture shown in Figure 20, the photoanode consists of a conductive glass coated with a mesoporous semiconductor oxide film, onto which the dye molecules are adsorbed, the counter electrode is coated with Pt, and between them is the redox electrolyte, usually of the pair I^-/I_3^-.[26] In this system, the dye absorbs visible radiation, while the semiconductor acts primarily as an electron collector and transporter. In an efficient DSSC, the Lowest Unoccupied Molecular Orbital (LUMO) level of the excited dye must be energetically above the semiconductor's conduction band to allow electron injection, while the Highest Occupied Molecular Orbital (HOMO) level must be in a suitable position so that the oxidized dye is regenerated by the electrolyte [26,39]. Below, in Figure 20, a better understanding of the operation of DSSCs can be found.

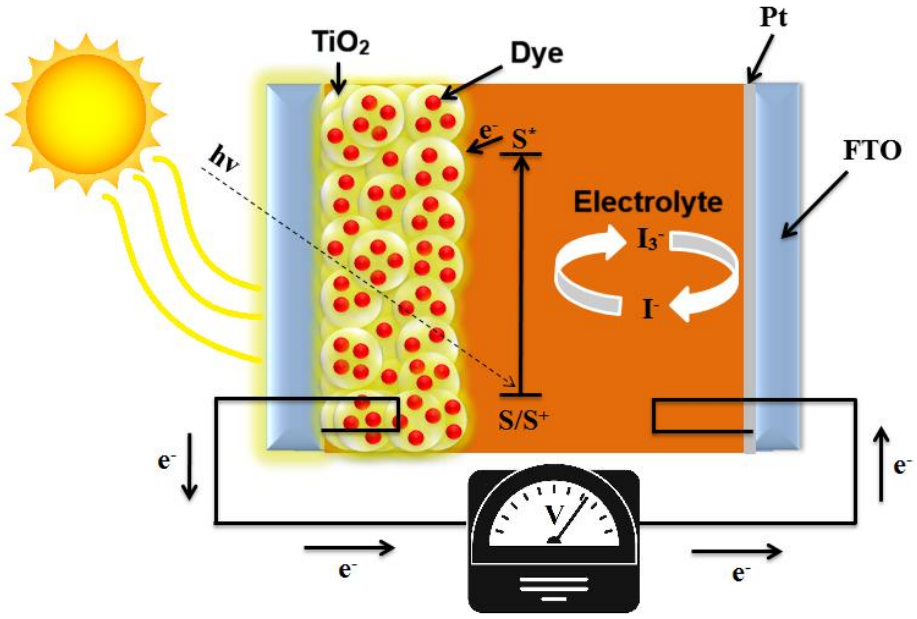


Figure 20 – Diagram of DSSC operation.

In the initial condition, before illumination, the dye is in its ground state, which can be represented as S. When solar radiation strikes the cell, photons pass through the FTO and reach the dye molecules anchored to the surface of TiO_2 or ZnO. The photon

energy promotes an electron from the HOMO to the LUMO, generating the excited state S^*. This step can be written as [26]:

$$S + h\nu \rightarrow S^* \tag{2.1}$$

or, in electronic terms,

$$S(HOMO) + h\nu \rightarrow S^*(LUMO) \tag{2.2}$$

This is the first essential step in the photovoltaic process: the conversion of light energy into an electronic excitation located in the dye molecule. Then, the electron in the excited state of the dye is rapidly injected into the conduction band of the semiconductor [26,38]. Thus, the dye loses the excited electron and becomes oxidized, represented by S^+, while the semiconductor receives the electron [39]:

$$S^* \rightarrow S^+ + e^-_{(CB)} \tag{2.3}$$

or, to phrase it more explicitly,

$$S^*(LUMO) \rightarrow S^+(HOMO\ vacante) + e^-_{TiO_2/ZnO} \tag{2.4}$$

The Figure 20 represents this step by the arrow that goes from the excited dye towards the semiconductor film. The driving force of this injection stems from the energy alignment: the LUMO of the dye must be at a higher energy than the edge of the conduction band of TiO_2 or ZnO, so that the electron transfer is thermodynamically favorable. After injection, the electron percolates through the nanocrystalline oxide lattice to the FTO, travels through the external circuit, performs electrical work, and reaches the Pt counter electrode [36-39].

Meanwhile, the oxidized dye S^+ cannot remain indefinitely in this state, as this would interrupt the photovoltaic process. It needs to be regenerated by the electrolyte. In the I^-/I_3^- system, iodide ions donate electrons to the oxidized dye, restoring it to its ground state [26]. A simplified and widely used way to perform this step is:

$$2S^{+} + 3I^{-} \rightarrow 2S + I_3^{-} \quad (2.5)$$

Or, in elementary form, considering one dye at a time:

$$S^{+} + e^{-} \rightarrow S \quad (2.6)$$

This electron is chemically supplied by the iodide. Thus, the electrolyte temporarily sacrifices itself to regenerate the dye, forming triiodide I_3^-. At the Pt counter electrode, electrons from the external circuit reduce I_3^- back to I_2^-, closing the redox cycle [26-28]:

$$I_3^{-} + 2e^{-} \rightarrow 3I^{-} \quad (2.7)$$

Thus, the electrolyte is not simply an ionic medium: it is the dye-regenerating agent and the mediator of positive charge transport within the cell. Platinum is used because it efficiently catalyzes the reduction of I_3^-, decreasing kinetic losses at this interface [26]. Therefore, the complete photoelectrochemical cycle of a DSSC can be summarized by the following main steps [26-28,39]:

$$S + h\nu \rightarrow S^{*}$$
$$S^{*} \rightarrow S^{+} + e_{(CB)}^{-}$$
$$2S^{+} + 3I^{-} \rightarrow 2S + I_3^{-}$$
$$I_3^{-} + 2e^{-} \rightarrow 3I^{-}$$

The macroscopic result of this set of processes is the generation of an electric current in the external circuit. In other words, light excites the dye, the dye injects electrons into the semiconductor, the semiconductor transports these electrons to the external circuit, the electrolyte regenerates the dye, and the counter electrode closes the electrochemical circuit [29].

In the specific case of TiO_2 and ZnO-based photoanodes, both are n-type semiconductor oxides, but they perform this role with distinct characteristics. TiO_2 is the classic material for DSSCs because it exhibits high chemical stability, good surface

affinity with dye anchoring groups, and a large specific surface area when used in a mesoporous structure. ZnO, on the other hand, generally has greater electron mobility, which can favor electron transport [28,38]. However, ZnO is more sensitive to surface interactions with certain dyes and acidic media, and may undergo surface dissolution and form aggregates that intensify recombination or hinder the ideal adsorption of the sensitizer. Therefore, although ZnO is promising as a fast electron transport pathway, TiO_2 often exhibits more robust and reproducible performance in conventional DSSCs [38,39].

When CuO is introduced into the system, a semiconductor oxide, typically of the p-type, comes into play, with a narrower band gap than TiO_2 and ZnO. Doping or modification with CuO alters the electronic and interfacial environment of the photoanode [28]. At appropriate concentrations, CuO can introduce electronic states capable of amplifying optical absorption, modifying band alignment, favoring charge separation, and reducing interfacial recombination, especially if it forms local n-p heterointerfaces with TiO_2 or ZnO [38-41]. In these heterointerfaces, an internal electric field is established that helps to repel electrons and holes, which can prolong the carrier lifetime and increase Jsc and, in some cases, Voc. However, excess CuO can create trapping centers and additional recombination pathways, impairing performance [28]. Thus, the effect of doping is strongly dependent on the concentration, dispersion, morphology, and quality of the interface [38,43].

For TiO_2-doped with CuO, the most accepted mechanism is that small amounts of CuO promote better charge separation and can adjust the Fermi level and the surface electronic structure of the photoanode [41]. Since the injected electron continues to be preferentially collected by the n-semiconductor's conducting lattice, the presence of CuO domains can act as an interfacial modifier: it reduces electron recombination in TiO_2 with the oxidized dye or with I_3^-, provided the interface is well-adjusted [40-43]. Conversely, if the CuO coverage is excessive, these domains may cease to act as charge separation aids and begin to compete with the main transport route, increasing recombination losses [28].

For ZnO doped with CuO, the reasoning is analogous, but with even greater sensitivity to the interface. ZnO already exhibits fast electron transport. Thus, the introduction of CuO can both improve charge separation via p-n heterojunctions and

disrupt the electronic equilibrium of the material if it generates excessive defects [38]. At moderate levels, copper doping can modify the carrier concentration, create shallow states useful for transport, and adjust the Fermi level, benefiting charge extraction. At high levels, however, recombination centers, structural disorder, and losses due to electron trapping arise, compromising photovoltaic efficiency [38-42]. From an energy standpoint, the cell operates properly when three conditions are met simultaneously [38]:

1. The LUMO of the dye must be above the conduction band of TiO_2 or ZnO to allow electron injection;
2. The HOMO of the dye must be below, at an appropriate potential, the redox pair I^-/I_3^-, to allow for dye regeneration;
3. Electron transport in the oxide must be faster than recombination reactions. When TiO_2 or ZnO are modified by CuO, the main effect is precisely to alter this third condition and, partially, also the local energy alignment at the interfaces.

It is also important to highlight the competitive processes responsible for the losses. The main one is electronic recombination, which can occur between: (i) the electron in the semiconductor and the oxidized dye S^+, or (ii) the electron in the semiconductor and the triiodide I_3^- of the electrolyte. These routes can be represented in a simplified way by [26-28]:

$$e_{(CB)}^- + S^+ \rightarrow S \quad (2.8)$$

$$e_{(CB)}^- + I_3^- \rightarrow 3I^- \quad (2.9)$$

When CuO doping is optimized, the tendency is to reduce these recombinations by improving the internal field and modifying the interfacial barriers, when it is not optimized, the exact opposite can occur [28,29]. Therefore, the performance improvement in TiO_2-CuO or ZnO-CuO photoanodes usually appears only within a narrow composition window [38-40].

In summary, the Figure 20 represents a DSSC in which the dye is the center of the photoactive process: it absorbs light, undergoes electronic transition from HOMO to LUMO, injects electrons into TiO_2 or ZnO, is regenerated by the I^-/I_3^- electrolyte, and

the circuit is closed by catalytic reduction at the Pt electrode. TiO_2 offers high stability and a large area for dye adsorption, ZnO offers faster electron transport, and doping with CuO, when properly controlled, can improve charge separation and interfacial alignment, contributing to increased photovoltaic performance of the DSSC.

2.8 Effects of CuO Doping on TiO_2 and ZnO Electrodes

Doping with CuO (copper oxide) in TiO_2 (titanium dioxide) and ZnO (zinc oxide), illustrated in Figure 21, improves the photovoltaic conversion efficiency of DSSCs due to a series of mechanisms that directly impact the electronic, optical, and structural properties of these materials [38].

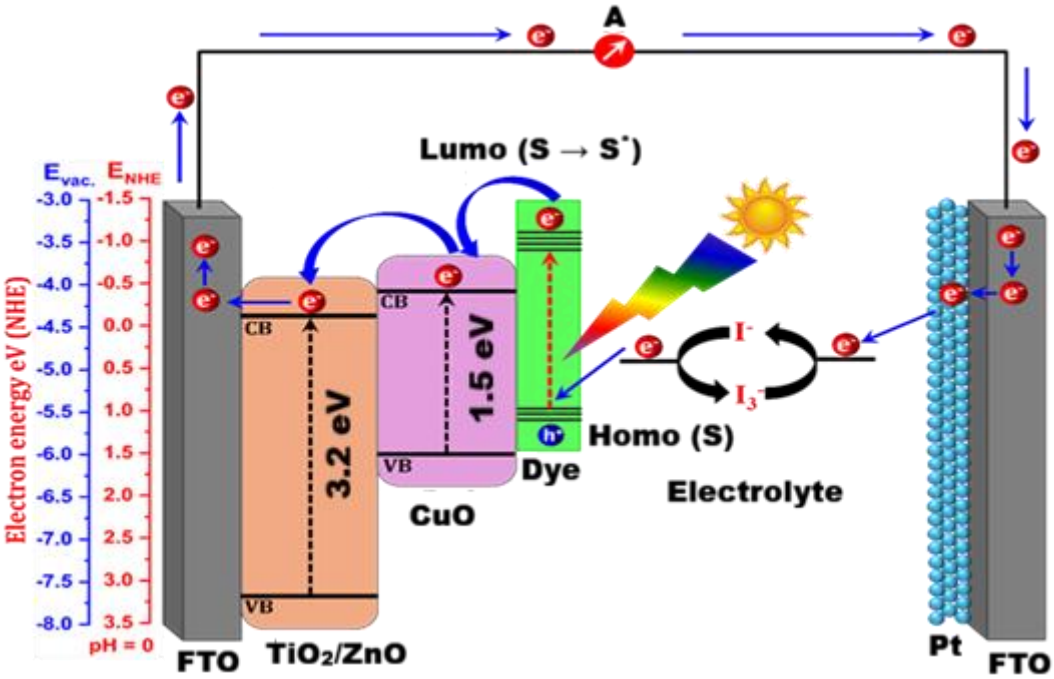


Figure 21 – Schematic of the effect of CuO doping on TiO_2/ZnO. Adapted from: [67].

The Figure 21 represents the operating mechanism of a DSSC based on a TiO_2/ZnO photoanode modified with CuO. Under illumination, the dye absorbs photons and is excited from the HOMO to the LUMO. Then, the excited electron is injected into the photoanode semiconductor. The presence of CuO, due to its smaller bandgap and

favorable energy alignment with TiO_2/ZnO, promotes better charge separation and reduces interfacial recombination between the injected electrons, the oxidized dye, and the electrolyte [28,38,39]. In this way, more electrons reach the FTO and travel through the external circuit to the Pt counter electrode, where the reduction of the I_3^-/I^- redox pair occurs. The electrolyte, in turn, regenerates the oxidized dye, closing the photoelectrochemical cycle. Experimentally, the TiO_2/CuO combination proved to be more efficient due to the greater chemical stability of TiO_2, the better interfacial interaction with the dye, and the more effective suppression of electronic recombination [38]. The factors are presented in greater detail below:

- Reduction of Electron-Hole Recombination: the recombination of photogenerated electrons with holes (or with electron-accepting species in the electrolyte) is one of the main limitations to efficiency [28,41]. Doping CuO in TiO_2 and ZnO can reduce the recombination rate due to the creation of intermediate energy levels within the band gap of these materials [38]. These intermediate levels act as "traps" for electrons, slowing down the recombination process and allowing more time for electrons to be transferred to the external circuit [38]. In the case of TiO_2 and ZnO, both are materials with a large band gap (~3.2 eV for TiO_2 and ~3.3 eV for ZnO), which limits their absorption of visible light [28,38]. The introduction of CuO (with a smaller band gap, around 1.2–2.1 eV) promotes the appearance of new energy states and reduces electronic recombination through different charge transfer pathways [41].
- Modification of Band Structure: Doping with CuO modifies the band structure of TiO_2 and ZnO. When CuO is additioned, energy levels arise within the forbidden band of the host semiconductor, which can reduce the effective forbidden band of the doped material [28,38]. This makes the material more efficient at absorbing visible light, broadening the light spectrum exploited by the solar cell [41]. TiO_2 doped with CuO has a greater capacity to absorb wavelengths in the visible spectrum, which increases the number of photons absorbed. In ZnO, which is known for its high electron mobility, doping with CuO also improves light absorption and charge separation [38-41].
- Enhanced Electron Transfer: CuO doping in TiO_2 or ZnO can also improve electron transfer within the material. CuO has high charge carrier mobility,

which facilitates electronic conduction in the doped material [38,42]. This promotes better separation of photoinduced charges, allowing photoexcited electrons to move more rapidly through the semiconductor layer to the collecting electrode. For TiO_2 and ZnO, which already have good electron transport properties, doping with CuO can minimize structural defects that act as recombination centers and improve electron mobility, resulting in greater efficiency in collecting the generated charges [38,42,43].

- Increased Electron Density: CuO, when introduced in small concentrations, can act as an electron donor or acceptor, depending on the oxidation state, increasing the density of free electrons in the material [28,41]. This increase in charge carrier density improves the electrical conductivity of the oxide layer, facilitating the migration of photogenerated electrons to the external circuit, which increases the current generated by the solar cell [28].
- Improved Light Absorption: The addition of CuO can alter the optical properties of TiO_2 and ZnO, making them more effective at absorbing light in the visible spectrum [38,42]. This is because CuO, with its narrower band gap, can absorb visible light more efficiently than pure TiO_2 or ZnO, which are better suited to absorbing ultraviolet light [43]. This greater absorption leads to a higher generation of electron-hole pairs, increasing the efficiency of the cell [41].
- Synergistic Effects at the Dye Interface: The interface between the semiconductor (TiO_2 or ZnO) and the dye is crucial for the efficiency of DSSCs, as it is where electron injection from the dye to the semiconductor occurs. Doping with CuO can modify the surface properties of the material, improving the anchoring of the dye to the semiconductor, which optimizes the electron transfer process [38,43]. An optimized interface can increase the efficiency of electron injection into the semiconductor, resulting in greater quantum efficiency [43].

These combined factors contribute to an increase in solar conversion efficiency in CuO-doped DSSCs on TiO_2 or ZnO, making them more competitive in terms of photovoltaic performance. The next chapter presents the instruments used and the characterization techniques.

3 Characterization Techniques

With the aim of evaluating the electrodes, the dye, and the DSSCs, this chapter presents the optical, morphological, structural, and electrochemical analyses performed. Figure 22 provides a comprehensive overview of the scope of each characterization. A brief introduction to the particularities of each technique and instrument used follows.

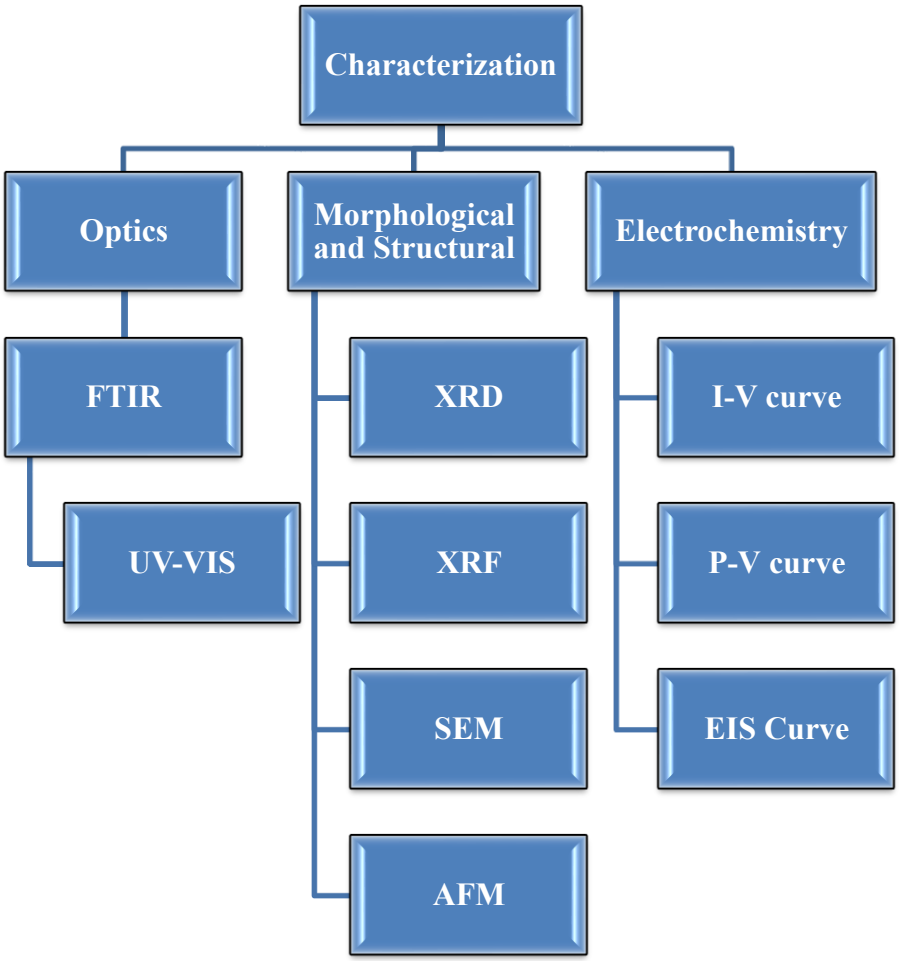


Figure 22 – Organizational chart of optical, morphological, structural, and electrochemical characterizations.

3.1 Optical Characterization

This section presents the optical analyses performed to evaluate the transmittance and absorption of the dye used in this study, as well as to identify the chemical elements through their corresponding spectra. For this purpose, Fourier Transform Infrared Spectroscopy (FTIR) and Ultraviolet-Visible Spectroscopy (UV-VIS) techniques were employed.

3.1.1 Fourier Transform Infrared Spectroscopy (FTIR)

The Fourier Transform Infrared (FTIR) spectroscopy technique aims to identify the chemical elements present in the analyzed samples. This identification is made possible by the fact that each atomic bond exhibits a degree of vibration, that is, a specific characteristic frequency [44]. In this way, FTIR allows the identification of the vibrations of these molecules.

As illustrated in Figure 23, to conduct this optical characterization, this study employed FTIR (model: Agilent Cary 630).



Figure 23 - Optical characterization of natural dye extracted from black grapes using FTIR – LaFEA (model: Agilent Cary 630).

The instrument measures the ability of the substance present in the sample to transmit, reflect, or absorb infrared radiation. This allows for the identification of the binding bands of the elements associated with the functional groups of the samples.

The Agilent Cary 630 FTIR is a compact and robust spectrometer designed for fast and reliable analysis, featuring [45]:

- Portable and compact design, ideal for laboratories with limited space;
- Fast spectrum acquisition (in seconds);
- Integrated ATR (Attenuated Total Reflectance) accessory, eliminating complex sample preparation;
- Typical spectral range: 4000–650 cm^{-1};
- High sensitivity for identifying functional groups in organic compounds (such as dyes).

FTIR is based on the interaction between infrared radiation and the vibrational modes of molecules. When IR radiation strikes the sample, some of the energy is absorbed if it corresponds to the vibrational frequency of specific chemical bonds [46].

The spectrum obtained is the result of transforming the interferogram according to Eq. 3.1[45,46]:

$$I(\tilde{\nu}) = \int_{-\infty}^{\infty} I(x)\ e^{-i2\pi\tilde{\nu}x}\, dx \tag{3.1}$$

Where:

- $I(x)$: interferogram (time domain/shift);
- $I(\tilde{\nu})$: spectrum as a function of wavenumber (cm^{-1});
- $\tilde{\nu}$: wavenumber (spectral frequency).

ATR (Attenuated Total Reflectance) is the most commonly used mode on the Cary 630:

- IR radiation undergoes total internal reflection in a crystal (example: diamond, ZnSe);

- An evanescent wave forms that penetrates a few micrometers into the sample;
- Absorption depends on the interaction with that wave.

Penetration depth Eq. (3.2) [46,47]:

$$d_p = \frac{\lambda}{2\pi n_1 \sqrt{\sin^2\theta - \left(\frac{n_2}{n_1}\right)^2}} \tag{3.2}$$

Where:

- λ: wavelength;
- n_1: crystal index;
- n_2: sample index;
- θ: angle of incidence.

In the context of DSSCs, FTIR spectroscopy is particularly relevant for identifying functional groups such as hydroxyls, carbonyls, and carboxyls, which play a fundamental role in the adsorption of the dye to the surface of semiconductors, such as TiO_2 and ZnO.

The technique allows the investigation of chemical interactions between the dye and semiconductor oxides, including modified systems, such as those doped with CuO. Shifts in characteristic peaks or changes in the intensity of vibrational bands can indicate the formation of coordinate bonds between the functional groups of the dye and the semiconductor, highlighting different adsorption modes (monodentate, bidentate, or bridging). Such interactions directly influence the efficiency of the electron injection process and, consequently, the photovoltaic performance of DSSCs [44,46]. Thus, FTIR analysis is an essential tool for understanding the optical properties of the dyes used in this work.

3.1.2 Ultraviolet-Visible (UV-VIS) Absorption Spectrophotometry

The instrument used in UV-VIS spectroscopy is called a spectrophotometer. This equipment is used to obtain information about the absorption level of a specific

sample placed in the optical path of the device. As a beam of light passes through the sample, its luminous intensity is recorded [48]. The spectrophotometry technique is widely used for absorption analyses in relation to wavelength in various areas, such as physics, chemistry, materials engineering, biochemistry, and clinical applications [48]. Figure 24 shows a representation of the basic operating principle of the UV-VIS spectrophotometer used in this work.

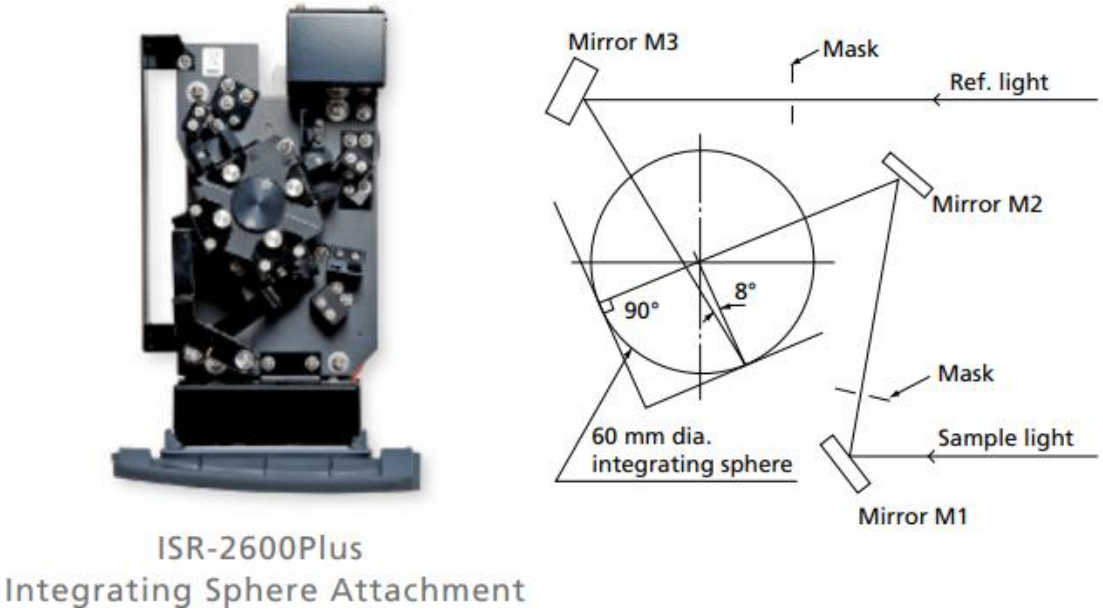


Figure 24 – Operation of the UV-VIS spectrophotometer (model: SHIMADZU UV-2600i). Adapted from: [48].

Figure 24 shows a schematic of the ISR-2600Plus integrating sphere accessory, used in conjunction with the Shimadzu UV-2600i spectrophotometer. This sphere, as the name suggests, plays a crucial role in collecting and measuring light, both from the reference and the sample, allowing for more precise and comprehensive analyses [66]. Its optical bandgap is given by Eq. (3.3) [48,49]:

$$(\alpha h\nu)^n = A(h\nu - E_g) \tag{3.3}$$

Where:

- α: absorption coeficiente;
- $h\nu$: photon energy;

- E_g: bandgap;
- n: transition type (½ or 2).

An integrating sphere is a hollow cavity with a highly reflective inner coating, usually made of a material such as tetrafluoroethylene. Light entering the sphere is reflected multiple times off the inner walls before being detected. This multiple reflection process ensures that the light is evenly distributed across the entire inner surface of the sphere, making the measurement of light intensity more accurate and independent of the position of the light source or detector [48]. The energy of radiation is given by Eq. (3.4) [49]:

$$E = \frac{hc}{\lambda} \tag{3.4}$$

Where:

- E: photon energy;
- h: Planck's constant;
- c: speed of light;
- λ: wavelength.

In studies requiring extreme precision, it is necessary to take extra precautions and avoid touching the optical surface of the cuvette, as oils from the skin, particles from cleaning cloths, dust, and even fingerprints can interfere with the results.

As explained regarding the operating principle, the fundamental components of a spectrophotometer include not only the cuvettes, but also the light source, mirrors, masks, integrating sphere and detector [48]:

- Light source: light from the spectrophotometer source (usually a deuterium or tungsten lamp) is directed onto the integrating sphere;
- Mirrors: Light is directed by means of mirrors (M1, M2, and M3) to different points on the sphere. Mirror M1 directs the sample light onto the sphere,

while mirror M2 directs the reference light;

- Masks: Masks are used to limit the amount of light entering the sphere and to define the angle of incidence of light on the sample;
- Integrating sphere: the light entering the sphere is reflected multiple times on the inner walls, creating a uniform distribution of light;
- Detector: A detector is positioned in a hole in the sphere. It measures the intensity of the light emerging from the sphere, both from the sample and the reference.

Figure 25 shows the SHIMADZU spectrophotometer used in this work, model (UV-2600 i), along with the LabSolutions UV-VIS software.



Figure 25 – Spectrophotometer used in UV-VIS absorbance analyses – LaFEA (model: SHIMADZU UV-2600i).

A key feature of this instrument's monochromator system (UV-2600 i) is its wide wavelength range for measurement. With the optional ISR-2600 Plus Integrating Sphere accessory, the wavelength range for measurement can be extended from 220 nm to 1400 nm, resulting in a significant expansion of its applications [48,49]. Therefore, this technique constitutes an essential tool for correlating optical properties and the performance of the devices developed in this work.

3.2 Structural and Morphological Characterization

To evaluate the phases of the crystalline chemical compounds TiO_2, ZnO, TiO_2-CuO, and ZnO-CuO and obtain quantitative values for each, X-ray diffraction (XRD) was performed using a D2 Phaser diffractometer (BRUKER). X-ray fluorescence (XRF) was also used, but for analytical purposes, to identify and quantify the elements in the samples. The equipment used for this characterization was the Epsilon 1 (Malvern Panalytical). The structural evaluation of the electrode surfaces was performed using atomic force microscopy (AFM) with a Nanosurf EasyScan 2 instrument. After the structural analysis, a morphological analysis of the anodes and cathodes was also performed using scanning electron microscopy (SEM) with a JEOL JSM-7100F instrument. The following subsections describe the operation of the aforementioned equipment.

3.2.1 X-ray Diffraction (XRD)

X-ray diffraction is a powerful analytical technique used to characterize the crystalline structure of materials. When X-rays strike a sample, they interact with the atoms of the sample, resulting in X-ray diffraction. Analysis of the diffraction patterns allows the identification of various information about the sample's structure [50]. Here are some of the main characteristics that X-ray diffraction can identify in a sample [51]:

- **Atomic arrangement:** X-ray diffraction can reveal information about the spatial arrangement of atoms in the sample. This includes the relative position of the atoms, the distance between them, and the angles between the crystal planes;
- **Crystal lattice:** from the diffraction patterns, it is possible to determine the crystal lattice of the sample. This involves identifying the unit cell parameters, which describe how the atoms are arranged in relation to each other;
- **Crystallite (grain) size:** the width of the diffraction peaks is related to the size of the crystallites in the sample. A wider diffraction spectrum may

indicate smaller crystallites, while narrower peaks are associated with larger crystallites;

- **Defects in the crystal lattice:** the presence of defects, such as vacancies or impurities, can be identified by analyzing diffraction patterns. These alterations in the crystal structure affect the diffraction patterns in specific ways;
- **Crystalline phases:** X-ray diffraction can help identify different crystalline phases present in the sample. This is especially useful for characterizing polycrystalline materials or complex samples with multiple phases;
- **Crystallographic orientation:** in certain cases, diffraction can be used to determine the preferred crystallographic orientation of the grains in the sample.

This information is valuable in various fields, including materials science, engineering, chemistry, physics, and others, where understanding atomic structure is essential to understanding the properties and behavior of materials. Since the main focus of this study is to modify anodic surfaces through CuO doping, characterization using this technique is extremely useful.

X-ray diffraction, developed in the early decades of the 20th century, represented one of the technological innovations that enabled the deciphering of the DNA structure [50]. This technique operates on crystals, which are molecules with a regular and repetitive arrangement. When X-rays pass through a sample, they are deflected or diffracted in different directions, according to the arrangement of atoms in the sample, with the final trajectory of the X-rays being recorded on a film. The cohesion of the crystalline arrangement is crucial, since the X-rays need to pass through several layers of atoms [51,52]. Otherwise, diffraction will occur in overlapping patterns, resulting in a blurred and indistinct image. However, when the structure presents an atomic arrangement that repeats periodically, the diffracted X-rays form a pattern composed of clear and well-defined points [52]. Different structures scatter X-rays, generating distinct characteristic patterns. This technique is shown in Figure 26.

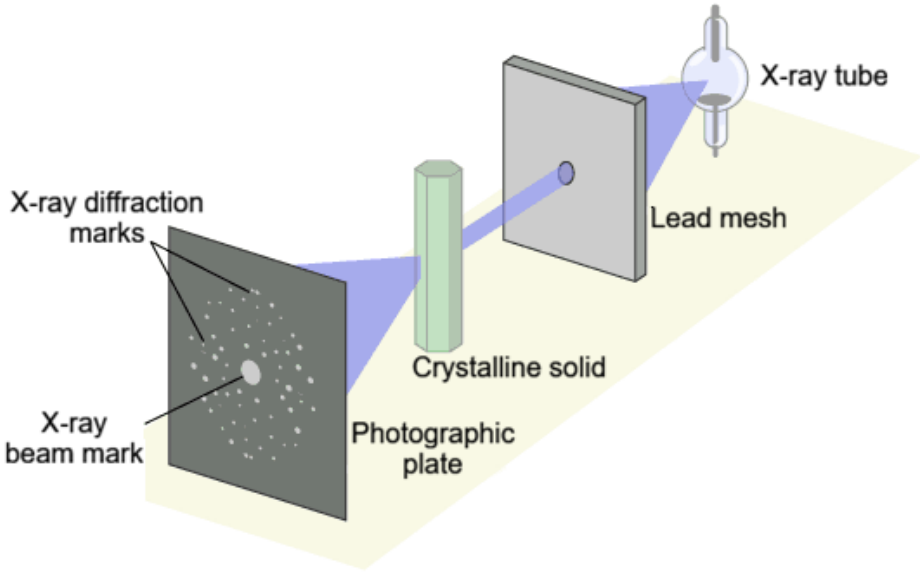


Figure 26 - X-ray diffraction technique. Adapted from: [53].

Its operation basically consists of the fact that when the atoms that make up matter are regularly spaced in a crystalline lattice and the incident radiation has a wavelength of the same order as this spacing, constructive and destructive interference will occur [50-53]. The constructive interference of scattered X-rays, originating from the crystalline lattice formed by the atoms, characterizes diffraction, as illustrated in Figure 27.

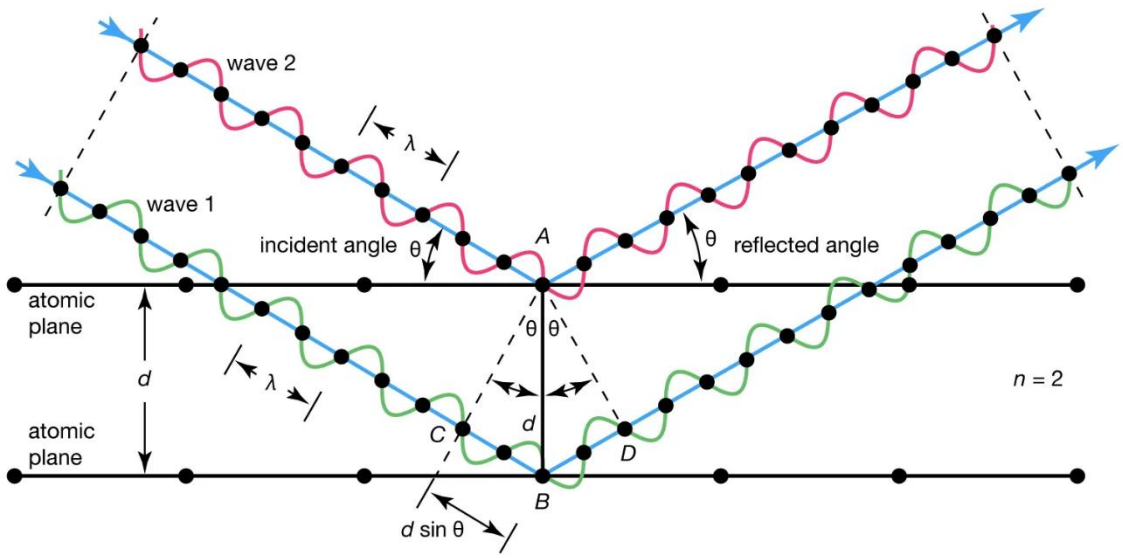


Figure 27 - Geometric representation of diffraction according to Bragg's Law. Adapted from: [54].

Coherent scattering (scattering of radiation that does not alter the energy of the incident beam) occurs at a well-defined angle called the Bragg angle. Interference occurs when Bragg's Law, Eq. (3.5) shown below is satisfied [52,54].

$$\lambda = 2.dhkl.sen\,\theta hkl \tag{3.5}$$

Where λ represents the wavelength of X-rays, d is the interplanar distance between atoms, θ is the Bragg angle, and the subscripts h, k, and l are the Miller indices that characterize the planes and directions within the crystal lattice [50-54].

The X-ray diffraction profile was obtained using the BRUKER D2 Phaser benchtop commercial equipment (Figure 28), located in the Laboratory of Electronic Instrumentation and Analytical Techniques (LIETA) at UERJ.



Figure 28 - D2 Phaser equipment used in XRD analyses.

The D2 Phaser is a diffractometer that operates in Bragg-Brentano geometry. It is equipped with a fast linear (1D) LYNXEYE detector, which can also operate in scintillator mode (0D), an X-ray tube with a copper anode, which has a characteristic emission line of 1.541 Å / 8.047 keV (Cu-Kα1), a maximum power of 300W (30 kV x 10 mA), and a scanning accuracy of ± 0.002° in the range of -3° to 160° in 2θ [51,55]. The sample holder is fixed in a spinner system, with a user-defined rotation speed, to increase statistical accuracy and reduce the effects of preferential orientation. It has an integrated monitor, keyboard, and mouse, and DIFFRAC.SUITE™ data acquisition software. The DIFFRAC software was used for phase identification. BRUKER's EVA™, which in addition to identifying the phases contained in the samples also provides a semi-quantitative graph of these phases to indicate their proportions, totaling a value of 100% [55].

Following the experiment, a scan was performed for each sample under the following operating conditions used in the diffraction measurement:

a) Voltage: 30 kV;
b) Current: 10 mA;
c) Slit: 0,6 mm;
d) Kβ filter: Ni;
e) Rotation: 15 rpm;
f) Measurement time: 0,5 s;
g) Initial angle: 5°;
h) Final angle: 90°;
i) Angular increment: 0,02°.

The analyses were conducted in θ–2θ geometry, employing Cu Kα radiation (λ ≈ 1.5406 Å), allowing the identification of the crystalline phases present in the TiO_2 and ZnO semiconductors and in the CuO-modified systems. It is observed, therefore, that the principle of the technique is based on the diffraction of X-rays by the crystalline planes of the material, with the diffraction peaks described by Bragg's Law, which relates the wavelength of the radiation to the interplanar spacing and the diffraction angle. From the obtained diffractograms, it was possible to identify the predominant

crystalline phases, such as the anatase phase of TiO_2, the structure of ZnO, and the monoclinic phase of CuO, as well as to evaluate possible structural modifications resulting from doping. The width of the diffraction peaks was used to estimate the average size of the crystallites using the Scherrer, Eq. (3.6) [50-53]:

$$D = \frac{K\lambda}{\beta \cos\theta} \tag{3.6}$$

Where:

- D: average crystallite size;
- K: constant (~0,9);
- β: peak width (FWHM);
- θ: diffraction angle.

Possible shifts in the peaks were analyzed as indicators of voltages in the crystal lattice and interaction between the phases. This information is fundamental to understanding the relationship between crystal structure, electronic transport, and photovoltaic performance of DSSCs, since the structural organization of semiconductors directly influences charge mobility and device efficiency [51-54].

3.2.2 X-ray Fluorescence (XRF)

X-ray fluorescence is a physical phenomenon in which atoms absorb energy in the form of X-rays and emit that energy in the form of lower-energy X-rays. This process occurs when atoms are exposed to high-energy X-ray radiation, such as X-rays or gamma rays. The X-ray fluorescence process generally involves three steps [56]:

- **Excitement:** atoms absorb the energy from incident X-rays, resulting in the removal of inner electrons from the atom. This event leaves a vacant space in lower energy levels.
- **Emission:** to fill the vacant space in the lower energy levels, electrons from higher levels can fall to these lower levels, releasing energy in the process. This energy is emitted in the form of lower-energy X-rays.

- **Detection:** an X-ray detector is used to measure and record the X-rays emitted during the process.

X-ray fluorescence is frequently used in analytical techniques, such as X-ray fluorescence spectroscopy (XRF). In this technique, the intensity and energy of the emitted X-rays are measured, allowing the identification of the elements present in a sample and the determination of their concentrations. This technique is widely used in various fields, including materials science, chemistry, metallurgy, engineering in general, industrial quality control, etc. [57].

In other words, X-ray fluorescence (XRF) is a physical phenomenon that occurs in the process of orbital electron transition. X-ray fluorescence analysis is a qualitative-quantitative method based on measuring the intensities (number of X-rays detected per unit of time) of the characteristic X-rays emitted by the elements that constitute a sample [56,57].

When a beam of ionizing radiation strikes the sample, an interaction process occurs with the constituent elements of the sample. In this interaction process, ionization of the elements can occur (photoelectric effect), and as a consequence, the elements (atoms) emit spectral lines with energies characteristic of the element and whose intensity is related to the concentration of the element in the sample [38,57]. Figure 29 presents a schematic representation of the X-ray fluorescence process.

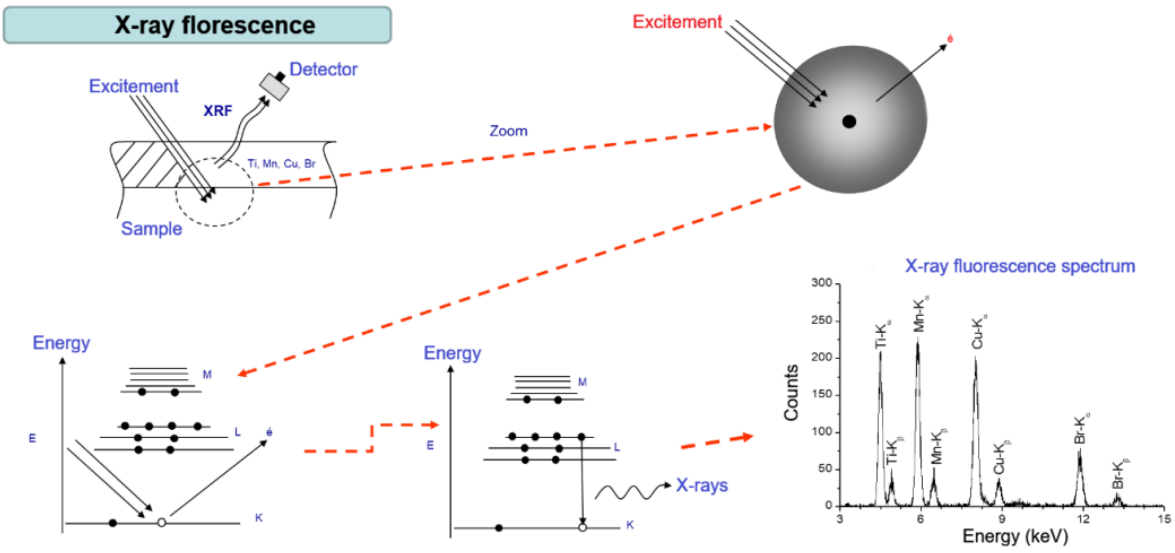


Figure 29 - Schematic representation of the X-ray fluorescence process. Adapted from: [58].

When an element in a sample is excited, it tends to eject electrons from its orbitals, and as a consequence, electrons from more distant levels perform a quantum leap to fill the resulting vacancy. Each electronic transition constitutes a loss of energy for the electron, and this energy is emitted in the form of an X-ray photon, with a characteristic and well-defined energy for each element. Thus, in summary, as explained at the beginning of the subsection, X-ray fluorescence analysis basically consists of three phases: excitation of the elements that constitute the sample, scattering of the characteristic X-rays emitted by the sample, and detection of these X-rays [56-58].

The objective of this characterization in the present work was to analyze TiO_2 and ZnO samples doped with CuO at different concentrations. For this purpose, the analyses were performed using the commercial Epsilon 1 instrument (Malvern Panalytical) from UERJ, as shown in Figure 30.

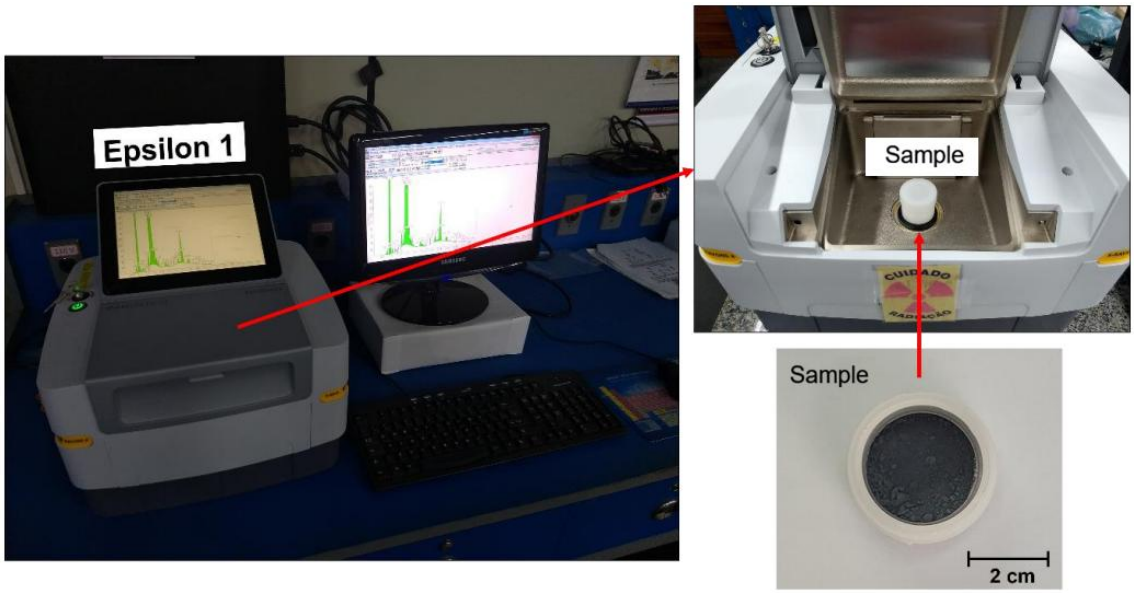


Figure 30 – Equipment for X-ray fluorescence characterization (Epsilon 1, model: Malvern Panalytical).

The equipment consists of an X-ray tube with a silver (Ag) target and an SDD (Silicon Drift Detector) (energy resolution < 135 eV for Mn-Kα). Sample analyses were performed using a voltage of 50 kV, a current of 100 μA, a Cu filter (500 μm) with an

acquisition time of 300 s. Elemental concentrations were calculated using the equipment's own software and the fundamental parameters of X-ray fluorescence [59]. Elemental identification is done using Moseley's Law, Eq. (3.7) [58]:

$$\sqrt{\nu} = K(Z - \sigma) \tag{3.7}$$

Where:

- ν: frequency of emitted radiation;
- Z: atomic number;
- σ: shielding constant;

In the XRF spectra, in addition to the elements present in the samples, the XRF line peaks of the elements Ar (K lines) and Ag (L lines) appear. The XRF analyses were not performed in a vacuum, and the presence of Ar in the XRF spectrum is due to the presence of argon from atmospheric air (dry air contains about 1% Argon by volume, 1.0 atm, 20°C). The presence of Ag is a contribution from the target of the X-ray tube used in the acquisition of measurements. In the X-ray fluorescence spectrum, in addition to containing the characteristic X-ray peaks, it may contain some artifacts (sum peak and escape peak) [56-58]. The "sum peak" occurs in the XRF spectrum when two photons reach the X-ray detector simultaneously. Since the electronic circuit cannot discriminate the energies of each photon individually, the event will be recorded as if it were only one photon with energy corresponding to the sum of the energies of the two photons [59].

On the other hand, the “escape peak” results from the interaction of X-ray photons emitted by the sample atoms with the detector material (usually Silicon). The characteristic radiation that reaches the detector can cause characteristic Silicon XRF (Energy of 1.74 keV). These 1.74 keV photons can escape from the detector, thus the detector registers photons with energies lower than the E_0 energy of the photons incident on the detector [57,58]. The E_{esc} energy will be given by Eq. (3.8) [58]:

$$E_{esc} = E_0 - 1{,}74\ keV \tag{3.8}$$

Thus, using X-ray fluorescence, it was possible to analyze TiO_2 and ZnO samples doped with CuO at different concentrations, an analysis that was fundamental to the proposed study. In order to evaluate the morphology of the developed surfaces, the following subsection presents characterizations using electron microscopy techniques.

3.2.3 Scanning Electron Microscopy (SEM)

To evaluate the surface structures of samples composed of TiO_2, ZnO, CuO and Pt, the Scanning Electron Microscope (SEM) model (JEOL JSM-7100F) was used. This equipment has the ability to generate high-resolution images, evaluating the topographic aspects and composition of each of them [60].

This characterization was performed at the NanoFAB laboratory of UERJ, where it was possible to produce images using scanning electron microscopy of the two anodes and cathodes developed in this work. Figure 31 shows the equipment used.



Figure 31 – Scanning Electron Microscope (SEM) – NanoFAB (UERJ) (model: JEOL JSM-7100F).

The operation of the SEM basically consists of the integration of the following blocks: electron gun, demagnification system (reduction of the electron beam diameter) and scanning units [60]. A simplified and didactic schematic representation of the components that make up the equipment can be seen in Figure 32.

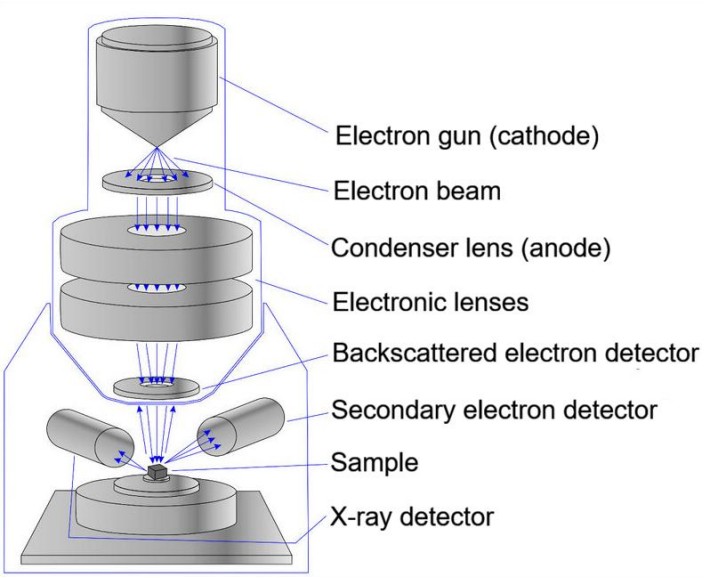


Figure 32 – Simplified schematic representation of the components that make up the SEM. Adapted from: [61].

An electron gun is used to emit an electron beam with sufficient energy to be captured by detectors. Through electromagnetic lenses, this beam is demagnified, aiming to generate a focused electron beam with a small diameter in a specific region of the sample [60,61]. The electron gun is the set of components whose purpose is to generate electrons, where the emitted beam must be stable and of sufficient intensity so that, upon reaching the sample, it can generate a good signal. For better understanding, Eq. (3.9) presents the wavelength of the electron (De Broglie) [62]:

$$\lambda = \frac{h}{p} = \frac{h}{\sqrt{2meV}} \tag{3.9}$$

Where:

- λ: electron wavelength;
- h: Planck's constant;
- m: electron mass;

- e: electron charge;
- V: acceleration voltage.

Therefore, the higher the voltage, the smaller (λ) and the better the resolution. The demagnification system of an electron beam is similar to the demagnification of a light beam, relying on condenser lenses and the final lens, also called the objective lens. Most SEMs have two condenser lenses, whose function is to reduce the diameter of the electron beam. The greater the electric current passing through the condensers, the smaller the final size of the electron beam, and consequently, the lower the electric current of the beam when it reaches the sample [60-62]. The final lens, on the other hand, has the function of focusing the image by varying the focal length of the electron beam along the optical axis of the column. Thus, the approximate solution is given by Eq. (3.10) [62]:

$$d \propto \frac{\lambda}{\alpha} \tag{3.10}$$

Where:

- d: resolution;
- α: beam opening.

It should be noted that this is the most powerful lens in the SEM, and due to the intense electric current passing through its coils, it generally needs to be cooled. In virtually all cases, this lens contains the deflecting coils, astigmatism correction coils, and the final aperture. Unlike the optical microscope, the electrons in this case do not produce a real image of the sample [61,62], what occurs is an effect on the beam illuminating the sample point by point, creating a rectangular pattern (scan), where the power of the signal generated from each point produces a reflection of the differences in the sample.

The scanning unit requires condenser lenses and electromagnetic deflection coils (scanning coils), capable of shifting the beam along a line, and then moving the line position to the other, so that a rectangular scan can be formed on the sample and on the display screen [60].

In order to achieve contrast in the image, the signal intensity from the interaction

of the sample beam needs to be measured point by point on the sample surface. In the last step, using an electron detector, the signals generated from the sample are collected, converted into photons by means of a scintillator, and into electrical signals used to modulate the image intensity on the monitor [60-62].

This work evaluated the structural morphology of the surfaces of anodes composed of TiO_2, ZnO, TiO_2-CuO, and ZnO-CuO at different concentrations, and of Pt cathodes. It is noteworthy that all were deposited on FTO substrates.

As a complement to these morphological evaluations, the following subsection presents the structural characterization of each electrode analyzed by atomic force microscopy.

3.2.4 Atomic Force Microscopy (AFM)

The AFM (Atomic Force Microscope) was the instrument used, capable of presenting microscopic images of electrodes with TiO_2, ZnO, CuO, and Pt surfaces in relation to their structure, scanning the samples through a cantilever with a sensitive and sharp tip. The deflection process of this cantilever is associated with Hooke's Law, Eq. (3.11) [63] and is capable of providing important data such as the width, length, and height of the surface of the analyzed sample [64]:

$$F = -kx \tag{3.11}$$

Where:

- F: force between tip and sample;
- k: cantilever spring constant;
- x: deflection.

With the AFM, it is possible to measure forces smaller than 1μ between the tip and the sample surface, and from the forces of attraction and repulsion between the two, it is possible to generate the topographic image.

Typically for DSSCs, the instrument is used to analyze the anode topography. For this work, in addition to the anodes, the Pt cathode topography was also evaluated.

Furthermore, this atomic force microscope can also map some mechanical and physicochemical properties [64]. Regarding the results, ideally the surface should have low roughness, and the topographic images should be uniform, since in a homogeneous film, the possibilities of recombination are minimized [63,64]. Several factors can contribute to obtaining good results, such as the deposition technique used, which for this work, for both anodes, was deposition through spin coating, the homogeneity of the solutions, since in some cases the particles may resist the ultrasonic vibration process, causing deformations on the surface, possible contaminations during the procedures, among others. In a simplified way, Figure 33 shows the operation of the AFM.

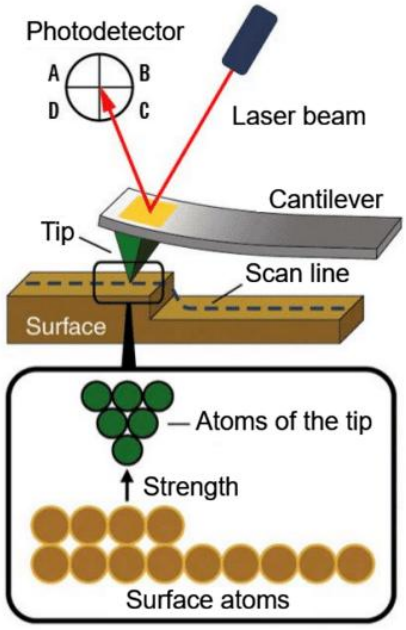


Figure 33 – Operating principle of the atomic force microscope. Adapted from: [65].

To detect deflections towards or away from the sample surface, a laser beam is fired. Reflecting the incident beam onto the flat top of the tip, any deflection on this will cause small changes in the direction of the reflected beam. To track these changes, a position-sensitive photodiode, identified as (PSPD) [62,65] is used.

Thus, if an AFM tip passes over a raised surface feature, the resulting deflection (and the subsequent change in the direction of the reflected beam) is recorded by the PSPD. Through Eq. (3.12) we have the Van der Waals Force (tip-surface interaction) [65]:

$$F \propto \frac{1}{r^2} \tag{3.12}$$

Where:

- r: tip-to-sample distance.

Figure 34 shows the AFM instrument used.



Figure 34 – Measurements performed using AFM – LaFEA (model: Nanosurf EasyScan 2).

When performing the procedures, it is emphasized that to obtain satisfactory dye adsorption results on the substrate, it is necessary that there are cavities or pores in the thin film of the nanostructure, and that there are homogeneous and mesoporous coatings throughout the substrate, without any elevations or large craters in the anodic film [62-65].

3.3 Electrochemical Characterization

The electrochemical and photovoltaic characterization of DSSC-type devices requires instrumentation capable of integrating precise electrical measurements with controlled lighting conditions. In this context, the use of a system based on a multi-potentiostat coupled to a solar simulator, specifically the IVIUM CompactStat from IVIUM Technologies, stands out. This equipment allows the simultaneous acquisition

of electrochemical and photovoltaic data with high sensitivity, being widely used in the analysis of semiconductor devices and photoelectrochemical systems [66]. Figure 35 shows the instrument used.



Figure 35 – Multi-potentiostat in conjunction with the solar simulator (Ivisun® IVIUM Technologies – IVIUM Compactstat).

The multi-potentiostat operates as an electrochemical control and measurement system capable of applying controlled potentials and recording resulting currents as a function of time or applied voltage. When used in conjunction with a solar simulator, the system reproduces lighting conditions close to standard solar radiation, allowing for a realistic evaluation of DSSC performance [66]. In the present study, an incidence power of 100 mW/cm² (standard condition AM 1.5G) was used [26], with a fixed distance of 15 cm between the solar cell and the light source, ensuring uniformity in irradiation and reproducibility of experimental results.

The relevance of this type of instrumentation for DSSCs is directly associated with the need to understand the processes of generation, separation, and transport of photoinduced charges. In these cells, the absorption of photons by the sensitizing dye promotes electronic excitation (transition from HOMO to LUMO), followed by the injection of electrons into the semiconductor (TiO_2 or ZnO) [26-28]. The multi-potentiostat allows for the quantitative monitoring of these processes through the electrical response of the device under controlled illumination. The photovoltaic response of DSSC can be described, to a first approximation, by the characteristic equation of semiconductor devices under illumination [26]:

$$I = I_{ph} - I_0\left(e^{\frac{qV}{nkT}} - 1\right) \quad (3.13)$$

Where I_{ph} represents the photogenerated current, I_0 is the saturation current, q is the elementary charge, n is the ideality factor, k is the Boltzmann constant, and T is the absolute temperature [26, 66]. This equation, implicitly implemented in the equipment's software algorithms, allows modeling the nonlinear behavior of the cell.

During the voltage sweep, fundamental parameters such as the short-circuit current (Jsc), obtained when V = 0, and the open-circuit voltage (Voc), corresponding to the condition where I = 0, are determined [66]. These points are extracted directly from the J–V curves generated by the system. Precise control of the voltage sweep rate, current resolution (typically in the nA to mA range), and signal stability ensure the reliability of the data obtained [66-69].

Furthermore, the equipment's software performs real-time acquisition, noise filtering, and automatic scaling adjustments, allowing for high resolution in experimental curves. The integration between hardware and software enables not only data acquisition but also mathematical modeling of the device's behavior, which is essential for detailed analysis of DSSC performance.

Therefore, the use of a multi-potentiostat coupled to a solar simulator constitutes an indispensable tool for the electrical and photovoltaic characterization of dye-sensitized cells, allowing for the direct correlation of internal physicochemical processes with the macroscopic performance parameters of the device.

3.3.1 Characteristic Curves of Photovoltaic Cells (J-V) and (P-V)

The electrical response of a solar cell under illumination can be described, to a first approximation, by the illuminated diode model. In this model, the total current of the device results from the difference between the photogenerated current by light absorption and the recombination current associated with the diode behavior of the device, as shown in Eq. 3.13. Since the multi-potentiostat measures the electric current I, this must be normalized by the active area of the solar cell to obtain the current density [66,67]:

$$J = \frac{I}{A} \tag{3.14}$$

Replacing I with J, we obtain the current density form [26,66]:

$$J = J_{ph} - J_0 \left[\exp\left(\frac{qV}{nkT}\right) - 1\right] \tag{3.15}$$

Where J_{ph} is the photogenerated current density and J_0 is the saturation current density. The short-circuit current density J_{sc} is obtained when the cell terminals are short-circuited, that is, when the voltage is zero V = 0. Substituting this condition into the equation for the illuminated cell [26-28,66]:

$$J_{sc} = J_{ph} - J_0 \left[\exp\left(\frac{q \cdot 0}{nkT}\right) - 1\right] \tag{3.16}$$

So we have:

$$J_{sc} = J_{ph} - J_0(1 - 1) \tag{3.17}$$

Therefore, under ideal conditions, the short-circuit current density is approximately equal to the photogenerated current density [26,66-68]:

$$J_{sc} \approx J_{ph} \tag{3.18}$$

This result shows that J_{sc} depends directly on the amount of photons absorbed, the efficiency of electron injection of the dye into the semiconductor, the electron transport in the photoanode, and the collection of charges in the conducting electrode. The open-circuit voltage, V_{oc}, it is obtained under the condition where the net current in the external circuit is equal to zero. (J = 0) [66]. Substituting this condition into the cell equation (3.15), dividing by J_0 and applying the natural logarithm [26]:

$$V_{oc} = \frac{nkT}{q} \ln\left(\frac{J_{sc}}{J_0} + 1\right) \tag{3.19}$$

This equation demonstrates that V_{oc} increases with the photogenerated current and decreases with an increase in J_0, which is associated with recombination processes [26-27]. In

DSSCs, V_{oc} is related to the difference between the quasi-Fermi level of electrons in the semiconductor and the redox potential of the electrolyte [26-29]. Figure 36 shows the J-V and P-V characteristic curves, with their electrical parameters Jsc, Voc, and Pmax.

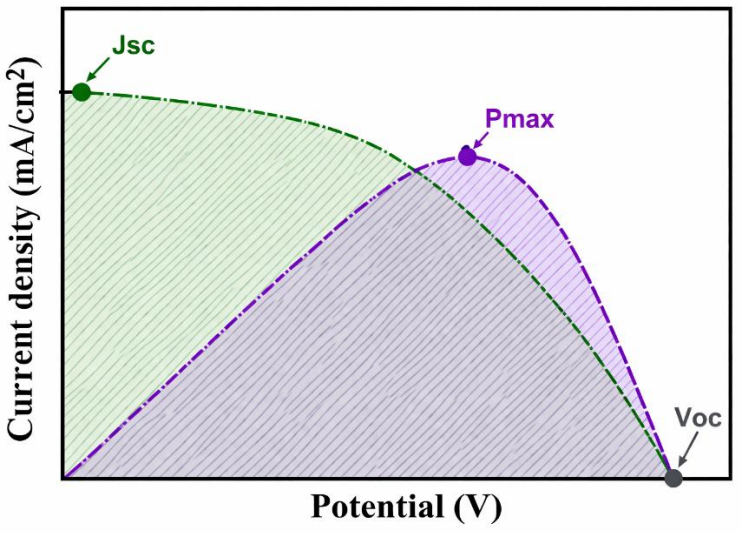


Figure 36 – Characteristic curves of DSSCs (J–V) and (P–V).

From the J-V curve, the software calculates the corresponding power point by point, generating the P-V curve. The point of maximum power is defined as [26]:

$$P_{max} = V_{max} \times I_{max} \tag{3.20}$$

The fill factor, FF, is obtained by the ratio between the actual maximum power of the cell and the theoretical maximum power given by $V_{oc} \times J_{sc}$ [26,28]:

$$FF = \frac{P_{max}}{V_{oc} \times J_{sc}} \tag{3.21}$$

The fill factor (FF) expresses the electrical quality of the cell. The more rectangular the J–V curve, the higher the fill factor and the lower the device's resistive and recombination losses [26-30]. Figure 37 graphically illustrates how the FF relates to Jsc and Voc.

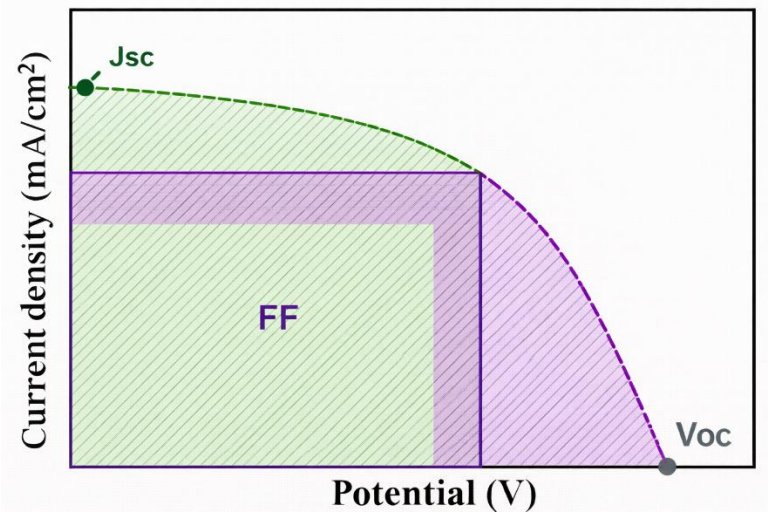


Figure 37 – Fill Factor (FF).

Therefore, the equation used to calculate the efficiency of DSSCs becomes [26,38,44]:

$$\eta = \frac{J_{sc} \times V_{oc} \times FF}{P_{in}} \times 100 \tag{3.22}$$

Comparative analysis of J-V curves between different photovoltaic technologies (silicon, perovskites, DSSCs, among others) is essential to determine specific advantages in efficiency, cost, and applicability [67-69]. In short, the J-V curve goes beyond simple electrical characterization, providing a comprehensive diagnosis that combines semiconductor physics, interface chemistry, and materials science [68]. This makes its analysis indispensable in the advancement of DSSCs and emerging photovoltaic technologies.

3.3.2 Electrochemical Impedance Spectroscopy (EIS)

Electrochemical Impedance Spectroscopy (EIS) was performed using the IVIUM CompactStat multi-potentiostat, operated via IviumSoft software, with the aim of investigating the dynamic processes of charge transport, electronic recombination, and ionic diffusion in dye-sensitized solar cells (DSSCs). Unlike direct current (DC) measurements, such as J–V curves, the EIS technique is based on the application of a

small-amplitude sinusoidal perturbation to the system, allowing the analysis of the electrochemical response as a function of frequency [66,70]. Mathematically, the system is excited by an alternating voltage signal of the type [26,72]:

$$V(t) = V_0 \sin(\omega t) \tag{3.23}$$

Resulting in an electric current [71]:

$$I(t) = I_0 \sin(\omega t + \phi) \tag{3.24}$$

Where V_0 and I_0 represent the amplitudes of the applied signal and the response, respectively, $\omega = 2\pi f$ is the angular frequency, and ϕ corresponds to the phase difference between voltage and current. From these quantities, the complex impedance of the system is defined [70-72]:

$$Z(\omega) = \frac{V(t)}{I(t)} = Z' + jZ'' \tag{3.25}$$

Where Z' represents the real (resistive) component and Z'' the imaginary component (associated with capacitive or diffusional effects) [28,38,70]. The IviumSoft software automatically performs frequency sweeps, typically over a wide range (from mHz to kHz), recording the Z' and Z'' values for each applied frequency [66,70-72].

The results are represented by the Nyquist diagram, in which the real part of the impedance (Z') is plotted on the horizontal axis and the negative imaginary part ($-Z''$) on the vertical axis. In this type of graph, each point corresponds to a distinct frequency, with high-frequency regions associated with fast processes, while low frequencies reflect slower phenomena, such as diffusion of species in the electrolyte [66,71].

Thus, to present the results, Nyquist diagrams (real part versus imaginary part of the impedance) and their equivalent circuit are generated, as shown in Figure 38.

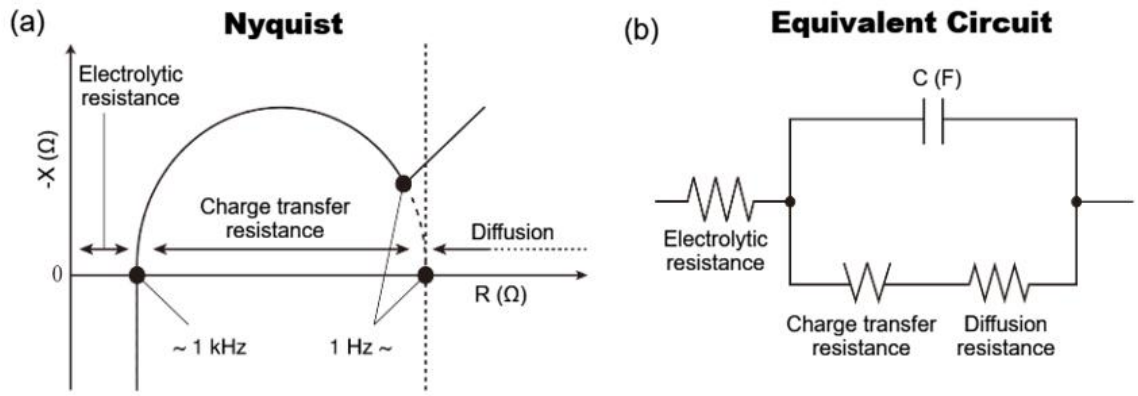


Figure 38 – (a) Nyquist and (b) Equivalent Circuit. Adapted from: [72].

Figure 38 (a) shows a typical Nyquist diagram for DSSCs. The initial intercept on the real axis corresponds to the electrolytic resistance R_s, which includes the ohmic contributions of the electrolyte, the conductive substrate, and the electrical contacts [26,66,72]. Next, a semicircular arc is observed, whose diameter is directly related to the charge transfer resistance R_{ct}, associated with electronic recombination processes and electron transfer at the semiconductor/electrolyte interface. Mathematically, this resistance can be estimated by the difference between the initial and final intercepts of the semicircle on the real axis [70-72]:

$$R_{ct} = Z'_{\text{final}} - Z'_{\text{inicial}} \tag{3.26}$$

Finally, in the low-frequency region, a characteristic slope associated with the diffusion process of redox species in the electrolyte is observed, described by Warburg impedance [66,72]:

$$Z_W = \sigma \frac{(1-j)}{\sqrt{\omega}} \tag{3.27}$$

Where σ represents the diffusion coefficient and ω the angular frequency. This contribution indicates limitations in mass transport within the electrolyte.

Figure 38 (b) shows the equivalent circuit used to model the electrochemical behavior of the DSSC. In this model, the electrolytic resistance R_s appears in series with a parallel branch composed of the charge transfer resistance R_{ct} and the capacitance (C),

in addition to an element associated with diffusion. The capacitance can be described by the relation [38,44,66,72]:

$$Z_C = \frac{1}{j\omega C} \tag{3.28}$$

This quantity is associated with the capacitance of the electrical double layer formed at the interface between the semiconductor (TiO_2 or ZnO doped with CuO) and the electrolyte. This parameter is directly related to the density of electronic states and the charge storage capacity at the interface [44,72].

The fitting of experimental data obtained via IviumSoft to this equivalent circuit is performed using numerical methods, allowing the quantitative extraction of fundamental physical parameters such as R_s, R_{ct}, C, and the diffusional contribution [66,71-73]. These parameters provide detailed information about the charge transport and recombination mechanisms in DSSCs, and are essential for correlating structural modifications, such as doping with copper oxide (CuO), with the photovoltaic performance of the device [72]. Therefore, EIS, when combined with the use of a multi-potentiostat, constitutes an indispensable tool for the in-depth analysis of the internal electrochemical processes of DSSCs, allowing for a more complete understanding of the factors that limit or enhance their efficiency.

To evaluate the frequency response of each DSSC, two impedance curves were generated. One represents the ideal, "fitted" behavior obtained from the electrical circuits modeled in IviumSoft software and presented in the Nyquist diagrams. The other refers to the actual frequency response generated from the experimental results using a multi-potentiostat (IVIUM Compactastat) and a solar simulator (Ivisun IVIUM Technologies). These same tools were used to obtain the J-V and P-V characteristic curves already presented in the previous subsection.

4 Results and Discussion

This chapter presents the results obtained from measurements performed using the instruments mentioned in the previous section. For optical characterizations, transmittance and absorbance analyses are presented. For morphological and structural characterizations, the results of counts, intensity, electron microscopy, and atomic force microscopy are presented. Finally, the current density curves, power supplied by each Grätzel cell, photovoltaic parameters, and electrochemical impedance are presented.

4.1 Transmittance (FTIR)

Transmittance-mode infrared spectroscopy (FTIR) is a fundamental tool for the structural characterization of organic and inorganic materials, and is widely used in the identification of functional groups present in natural dyes used in DSSCs [73]. Transmittance (T) is defined as the ratio between the intensity of electromagnetic radiation transmitted through a sample (I) and the intensity of incident radiation (I_0), as described by Eq. (4.1) [74]:

$$T = \frac{I}{I_0} \tag{4.1}$$

In the context of DSSCs, the characterization of dyes by FTIR is extremely important, since the photovoltaic performance of these devices strongly depends on the interfacial interaction between the sensitizing dye and the semiconductor, typically titanium dioxide (TiO_2). For efficient electron injection from the excited dye into the semiconductor's conduction band, the dye must possess functional groups capable of anchoring to the oxide surface. Among these groups, phenolic hydroxyls (–OH), carbonyls (C=O), carboxylic groups (–COOH), and C–O bonds stand out, frequently present in natural compounds such as anthocyanins and flavonoids [44,71,73].

Transmittance analysis in FTIR allows the identification of these functional groups and, consequently, inferences about the dye's adsorption potential on TiO_2. Furthermore, the presence of π-conjugated systems, associated with aromatic C=C bonds, is essential for light absorption in the visible region and for the efficiency of the

photoexcitation process. Therefore, spectroscopic characterization not only provides structural information but also establishes a direct correlation between the dye's chemical composition and its performance as a sensitizer [68,71].

Figure 39 shows the transmittance of the analyzed dyes. All spectra exhibit bands in the typical region of phenolic compounds and natural pigments with π-conjugated systems, which is consistent with the presence of classes of secondary metabolites with photosensitizing potential, such as anthocyanins, flavonoids, phenolic acids, carotenoids, and other oxygenated species. In DSSCs, the relevance of these chemical functions is directly associated with the dye's ability to adsorb to the semiconductor surface and promote electron transfer after photoexcitation. In particular, oxygen-containing groups, such as phenolic hydroxyls and oxygenated carbonyls/conjugations, are crucial for dye anchoring on the hydroxylated surface of TiO_2 and ZnO [28,30].

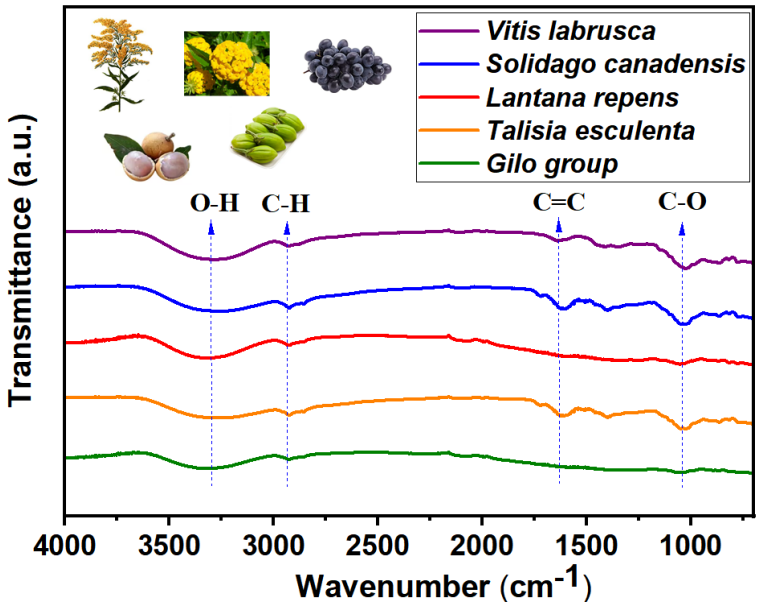


Figure 39 – Transmittance spectra of the evaluated dyes. Adapted from: [28,30].

The broad band observed between approximately 3600 and 3000 cm^{-1}, with a minimum around 3300 cm^{-1}, was attributed to O–H stretching. This broad absorption is typical of hydroxyl groups involved in hydrogen bonding, especially in phenols, alcohols, sugars linked to glycosylated pigments, and adsorbed residual water. In the context of sensitized cells, the presence and intensity of this band are relevant because

TiO_2 surfaces have terminal and bridged –OH groups, which participate in the adsorption of the sensitizer; furthermore, organic molecules containing hydroxyl and carbonyl groups tend to interact with these surface sites through coordination, hydrogen bonding, or partial chelation [28-30].

In the 3000–2850 cm^{-1} region, particularly near 2920 cm^{-1}, a band attributed to the C–H stretching of aliphatic groups is observed. Although this region is not, by itself, the main factor responsible for anchoring to TiO_2 and ZnO, it is consistent with the presence of methyl/methylene groups and organic substituents belonging to the framework of pigments and phenolic compounds present in the extracts [38,68]. In anthocyanins and other substituted flavonoids, this contribution may be associated with methoxyl groups and fragments of the lateral organic structure [68]. Thus, this band helps confirm the organic nature of the extracts and the presence of a sufficiently complex aromatic-aliphatic molecular matrix to act as a visible light absorber[71-73].

The band located around 1600–1650 cm^{-1} was assigned in the graph to the C=C mode, consistent with the stretching of aromatic conjugated double bonds of the flavylium/flavonoid skeleton and other aromatic systems in the extracts [75]. This assignment is coherent with chromophore compounds responsible for the intense coloration of natural dyes. However, from a spectroscopic point of view, this region may also contain overlapping contributions from conjugated ν(C=O) and/or the angular deformation of H–O–H from adsorbed water [68,75]. In extracts rich in anthocyanins and conjugated phenolic compounds, this band is particularly relevant because it indicates the existence of a delocalized π system, essential for the absorption of visible light and for the promotion of dye electrons to the excited state. This point is central to DSSCs: in addition to adsorbing well, the dye must possess a conjugated electronic structure capable of injecting electrons into the conduction band of TiO_2 and ZnO [28,30,38].

In the 1200–1000 cm^{-1} region, particularly near 1040 cm^{-1}, a band associated with C–O stretching is observed, possibly with a contribution from C–O–C. This band is typical of alcohols, phenols, aryl ethers, and especially glycosidic linkages, which are very common in plant pigments [28-30]. In glycosylated anthocyanins, this region is frequently intense and is related to both alcoholic/phenolic functions and the saccharide fragment of the molecule [68]. From a functional point of view, this band is particularly

important because it signals the high oxygenation of the dye structure. In natural sensitizers, greater availability of oxygenated groups tends to favor interfacial interaction with the semiconductor oxide, especially when phenolic hydroxyls and carbonyl/conjugated systems coexist [71,75].

By qualitatively comparing the spectra, the *Vitis labrusca* extract presents the most consistent vibrational set with a matrix rich in conjugated phenolic compounds and oxygenated groups potentially active for adsorption [28]. Its O–H band is broad and well-defined, the absorption at ~1600 cm^{-1} is clearly perceptible, and the C–O region is more pronounced than in some of the other extracts [28,38]. This behavior suggests a greater relative abundance, or greater spectroscopic accessibility, of typical anthocyanin and polyphenol functions [30,75]. This interpretation is consistent with the known chemical composition of dark grapes and materials derived from *Vitis labrusca*, in which the skin concentrates anthocyanins, in addition to other phenolics, such as flavonols and stilbenes. In grapes, the phenolic fraction of the skin is particularly important for photosensitizing applications because it combines conjugated chromophores with multiple oxygenated groups, two desirable requirements for TiO_2- and ZnO-based DSSCs [38].

This spectral signature of *Vitis labrusca* therefore supports its selection as a reference sensitizer in the present work. In mechanistic terms, the better interaction previously observed between this dye and TiO_2 can be rationalized by the presence of phenolic hydroxyl groups and conjugated oxygenated functions, capable of establishing interaction with surface Ti(IV) sites and/or with hydroxyl groups of the oxide. In DSSCs, this strong interaction is fundamental because it simultaneously controls: (i) the amount of dye adsorbed; (ii) the stability of the molecular coating; (iii) the electronic coupling between the LUMO of the dye and the TiO_2 conduction band; and (iv) the degree of interfacial recombination. In other words, it is not enough for the extract to absorb light: it needs to adsorb efficiently and in an electronically favorable way [28,30,38]. The spectrum of *Vitis labrusca* points precisely to a molecular chemistry more suited to this role.

In contrast, the spectra of *Lantana repens*, *Talisia esculenta*, and the *Gilo group* exhibit more discrete or less resolved bands in the key O–H, C=C/C=O conjugated, and C–O regions, suggesting a lower relative density of anchoring groups and/or a lower

concentration of conjugated phenolic chromophores in the crude extract [28,30]. The *Solidago canadensis* extract also shows relevant bands, especially in the O–H and C–O regions, but the overall profile is still less favorable than that of *Vitis labrusca* to justify its adoption as a model dye in this study [28,30]. In an analysis focused on DSSCs, less intense spectra in these regions are generally associated with a weaker interaction with the TiO_2 and ZnO surface, less coverage of the mesoporous film, and consequently, greater adsorption heterogeneity. This tends to penalize electron injection and increase the chance of recombination [38].

For the purpose of pre-selecting the dye, the spectral behavior of *Vitis labrusca* is sufficiently convincing and is in full agreement with the previous results of better interaction with TiO_2 and ZnO obtained by the group [38]. Thus, the use of this extract in the present study was not arbitrary, but rather based on consistent chemical and interfacial evidence.

Based on this selection, the strategy adopted in this work, namely the doping of TiO_2 and ZnO with CuO, acts on the other critical component of the photoanode: the semiconductor. The scientific justification is that, once the dye with the best interfacial affinity is chosen, it becomes possible to investigate more cleanly the effect of oxide modification on electronic transport and charge separation. The incorporation of CuO into TiO_2 and ZnO is reported in the literature as a route capable of modifying the optical and electronic response of the photoanode, promoting better use of visible radiation and favoring charge separation by forming p–n TiO_2/CuO and ZnO/CuO heterojunctions, provided that the copper concentration is adequately controlled [28,38]. Recent studies show that TiO_2 and ZnO photoanodes doped/modified with Cu can increase current density and efficiency, with evidence of lower resistance to electronic transport and greater resistance to recombination; On the other hand, excess CuO can introduce trap centers and intensify recombination losses [38].

4.2 Absorbance (UV-VIS)

Absorbance is a physicochemical quantity that expresses the ability of a substance to absorb electromagnetic radiation at specific wavelengths. In the context of UV-Vis spectroscopy, this property is directly related to electronic transitions between

molecular energy levels, especially $\pi \rightarrow \pi^*$ and $n \rightarrow \pi^*$ type transitions in conjugated organic compounds, such as the natural dyes used in DSSCs. Absorbance (A) is quantitatively described by Beer-Lambert's Law, given by Eq. (4.2) [38]:

$$A = \varepsilon \cdot l \cdot c \tag{4.2}$$

Where ε is the molar absorptivity coefficient ($L \cdot mol^{-1} \cdot cm^{-1}$), l is the optical path length (cm) and c is the concentration of the absorbing species ($mol \cdot L^{-1}$). This relationship demonstrates that absorbance is proportional to both the concentration of the dye and its intrinsic ability to absorb light at a given wavelength [38,71].

In the case of DSSCs, absorbance analysis plays a central role, as the photovoltaic performance of these devices is directly associated with the efficiency with which the dye is able to absorb photons from solar radiation and convert them into free electrons [44,75]. The basic operation of a DSSC involves the excitation of the dye by incident light, promoting an electron from the ground state (HOMO) to an excited state (LUMO) [67]. From this excited state, the electron is injected into the conduction band of the semiconductor (typically TiO_2 or ZnO), initiating the process of generating electric current [38].

Therefore, an ideal dye for DSSCs should exhibit high absorbance in the visible region (≈ 380–780 nm), which corresponds to the largest fraction of the solar spectrum incident on the Earth's surface [68,71]. Dyes that absorb predominantly in the ultraviolet region (< 380 nm) tend to be less efficient, since this range represents a smaller fraction of the total solar irradiance. Furthermore, the position and intensity of the absorbance bands provide important information about the dye's electronic structure, the degree of molecular conjugation, and the presence of active functional groups.

Furthermore, comparative analysis of absorbance spectra between different dyes allows selection of the one that exhibits the greatest overlap with the solar spectrum, the highest absorption intensity, and the best potential for interaction with the semiconductor. This step is essential in the development of DSSCs, as the choice of sensitizer directly impacts parameters such as current density (Jsc) and, consequently, the efficiency of the device. Figure 40 shows the absorbance spectra of the natural dyes analyzed [28,30,38].

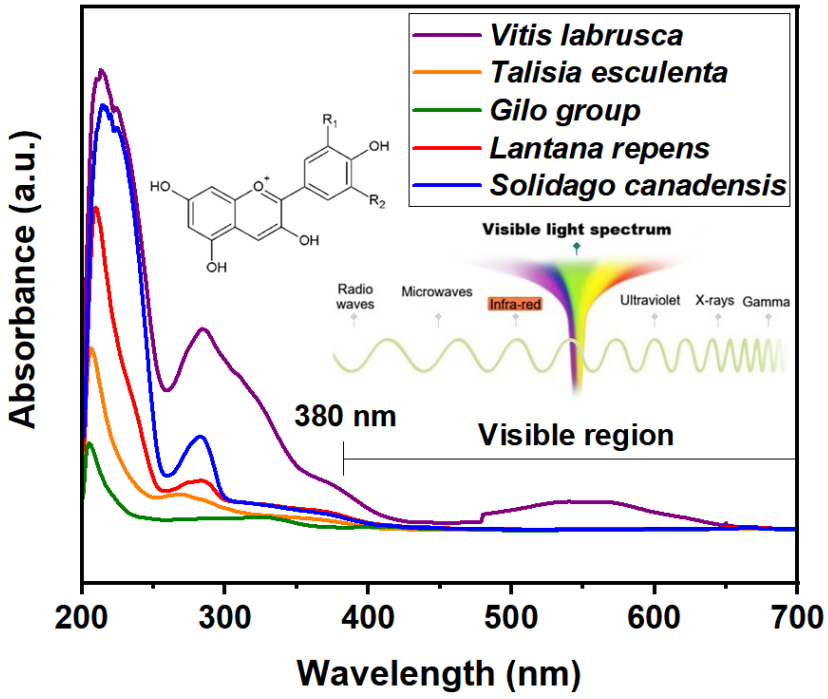


Figure 40 – Absorbance of natural dyes. Adapted from: [28,30].

Among the five extracts, the *Vitis labrusca* extract presents the most favorable optical profile. Extremely intense absorption is observed in the deep UV, with a main maximum visually located around 220–230 nm, followed by a broad secondary band/shoulder between approximately 280 and 330 nm, in addition to a spectral tail that extends into the visible region [28]. This extract is the only one that maintains a perceptible and relatively broad absorbance between about 500 and 620 nm, with a broad maximum around 540–580 nm [38,44]. This behavior is typical of extracts rich in anthocyanins, whose electronic transitions in the visible range are responsible for the red, purple, and violet colorations. The molecular structure of anthocyanin can be seen in Figure 41 [73].

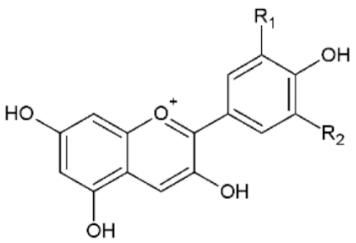


Figure 41 – Basic molecular structure of anthocyanin [69].

The extract of *Solidago canadensis*, in turn, also exhibits very high absorbance in the UV, with a main maximum near 220–235 nm and a second maximum/shoulder around 280–290 nm. However, unlike *Vitis labrusca*, its absorbance drops abruptly after ~300 nm, becoming practically zero above 380–400 nm [28,30]. This profile is compatible with extracts dominated by compounds that preferentially absorb in the UV, such as flavonoids without an intense visible band and other less conjugated phenolics. In terms of DSSC application, this behavior is less favorable because, despite indicating the presence of aromatic chromophores, it reveals low absorption capacity in the visible region, limiting photocurrent Generation [28-30]. Thus, an extract may even exhibit high absolute absorbance in the UV, but still be inferior as a sensitizer if it does not adequately cover the visible range.

The *Lantana repens* curve shows a pronounced maximum at approximately 220–225 nm, followed by a rapid decrease in absorbance and a discrete shoulder between 270 and 300 nm. The response above 350–380 nm is minimal [30]. This type of profile suggests that the extract contains phenolic and flavonoid compounds, but in insufficient concentration, composition, or chemical state to produce a significant visible band. The literature on species of the genus *Lantana repens* reports the presence of flavonoids, phenols, and other secondary metabolites, which is consistent with the observed UV absorption, however, from a photoelectrochemical point of view, the low absorption in the visible range implies less potential as a primary sensitizer compared to *Vitis labrusca* [28,30,38].

For *Talisia esculenta*, a curve of lower overall intensity is observed, with predominant absorption in the 210–240 nm range and a practically monotonic decrease up to approximately 350–400 nm, without a relevant visible band [28]. This suggests a predominance of compounds that absorb in the UV range, probably associated with phenolics and flavonoids with lower chromophoric effectiveness for DSSC. Phenolic compounds, flavonoids, and anthocyanins are present in *Talisia esculenta*; however, in the obtained spectrum, these constituents did not generate a visible signature comparable to that observed for *Vitis labrusca* [28,30,44]. Therefore, even though the extract possesses antioxidant activity and phytochemical richness, its capacity as a photosynthetic sensitizer seems limited by the restricted spectral coverage.

The *Gilo group* exhibits the lowest optical response among all extracts analyzed.

The curve shows moderate absorbance in the deep UV, with a maximum around 210–220 nm, followed by low and practically constant values up to the threshold of 350–400 nm, becoming negligible in the visible spectrum [28]. This behavior suggests the presence of phenolic compounds, but with lower chromophore density or with less efficient conjugated systems for absorbing visible light. The spectral profile of this dye indicates weak potential as a light sensitizer for DSSCs when compared to *Vitis labrusca* [28,38].

Based on UV-Vis spectra, the *Vitis labrusca* extract showed the most favorable combination of absorption intensity, spectral extent, and presence of a band in the visible region, unlike the other extracts, whose absorption was mainly concentrated in the ultraviolet. This result, associated with the recognized presence of anthocyanins and hydroxyl/carbonyl groups with anchoring capacity on TiO_2, justifies its selection as a sensitizer in the present study involving TiO_2 and ZnO photoanodes modified with CuO.

4.3 Counts (XRD)

The structural characterization of semiconductor materials used in DSSCs is a determining factor for understanding their physicochemical properties and, consequently, their photovoltaic performance. In this context, X-ray diffraction (XRD) stands out as one of the most important tools for identifying crystalline phases, evaluating the degree of crystallinity, determining structural parameters, and investigating possible doping-induced modifications [38,76].

Figures 42 and 43 show the samples (XRD) respectively: CuO, TiO_2, TiO_2-$CuO_{5\%}$, TiO_2-$CuO_{10\%}$, TiO_2-$CuO_{20\%}$, TiO_2-$CuO_{30\%}$, TiO_2-$CuO_{50\%}$; and ZnO, ZnO-$CuO_{5\%}$, ZnO-$CuO_{10\%}$, ZnO-$CuO_{20\%}$, ZnO-$CuO_{30\%}$, ZnO-$CuO_{50\%}$. The diffractograms of the samples were evaluated in the range of 20º to 80º, since before 20º and after 80º there was no relevant information for the identification of the phases of the compounds. Figures 44 and 45 show the overlaps of the TiO_2 and ZnO samples respectively, varying according to the CuO doping.

Table 2 shows the percentage relationship between the amount of crystalline matter and the amount of amorphous matter contained in the samples. Table 3 shows the

compounds found in each sample and the semi-quantitative percentages of each compound in the samples. The crystalline structure of copper oxide was in the form of tenorite. The structure of titanium dioxide was in two forms: anatase and rutile. Finally, the crystalline structure of ZnO was in the form of zincite.

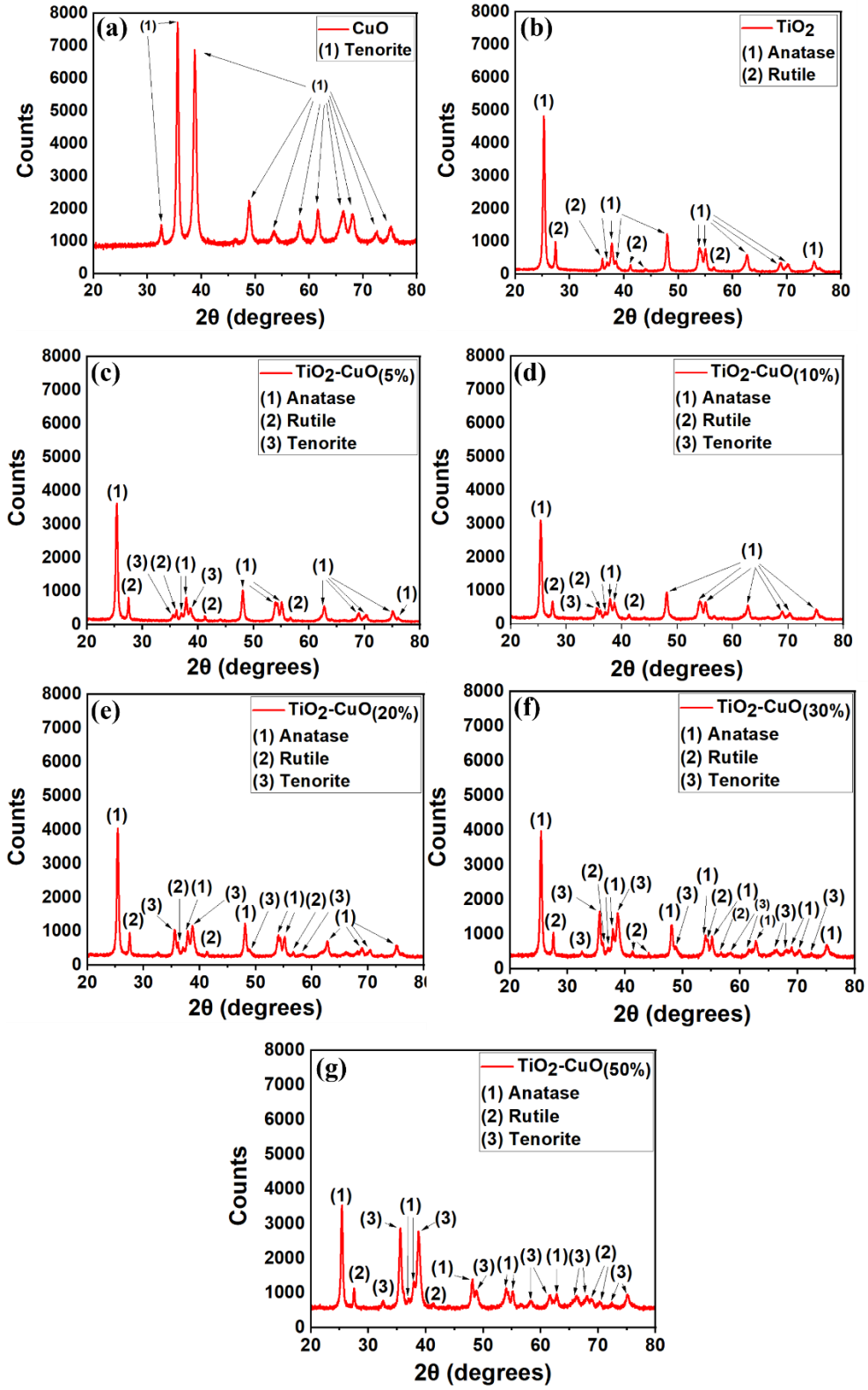


Figure 42 – Samples (XRD): (a) CuO, (b) TiO_2, (c) TiO_2-$CuO_{5\%}$, (d) TiO_2-$CuO_{10\%}$, (e) TiO_2-$CuO_{20\%}$, (f) TiO_2-$CuO_{30\%}$, (g) TiO_2-$CuO_{50\%}$. Adapted from: [38].

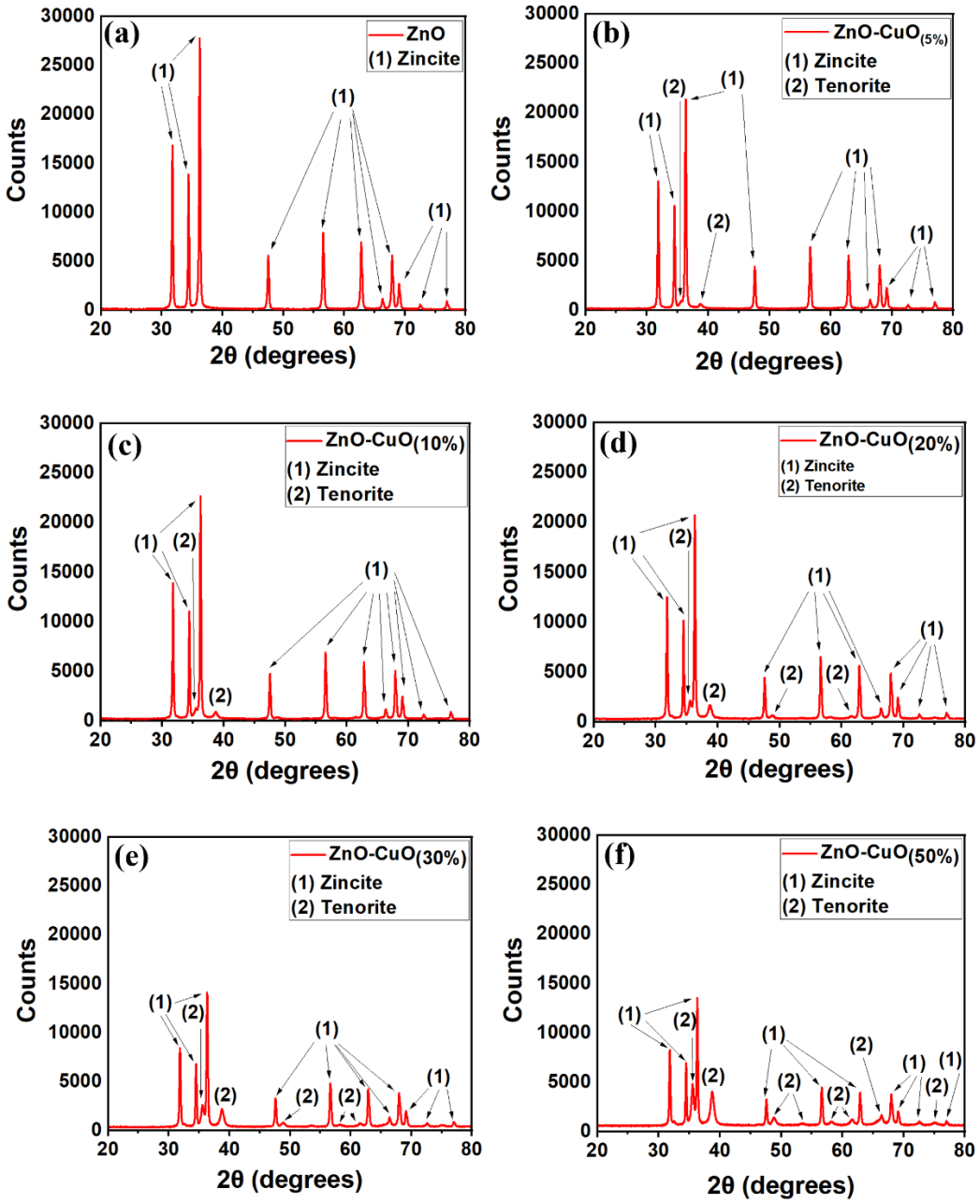


Figure 43 – Samples (XRD): (a) ZnO, (b) ZnO-$CuO_{5\%}$, (c) ZnO-$CuO_{10\%}$, (d) ZnO-$CuO_{20\%}$, (e) ZnO-$CuO_{30\%}$, (f) ZnO-$CuO_{50\%}$. Adapted from: [38].

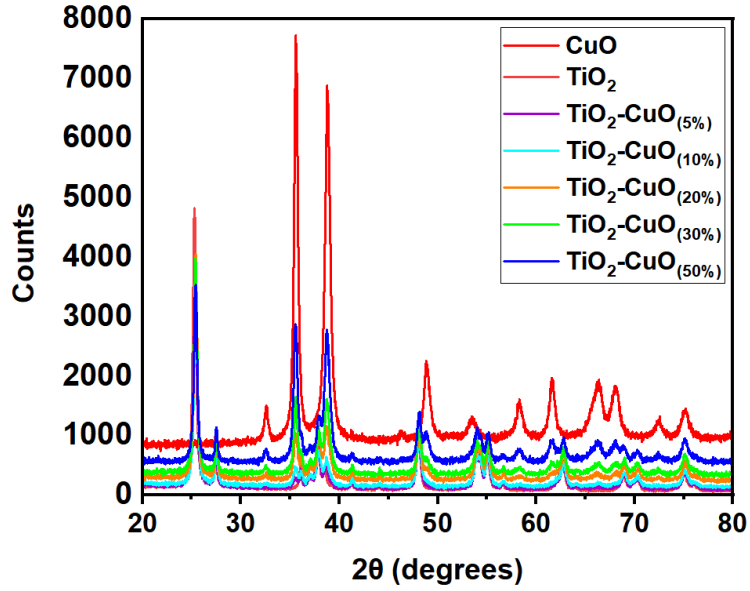


Figure 44 – Overlap of TiO_2 samples varying with CuO doping. Adapted from: [38].

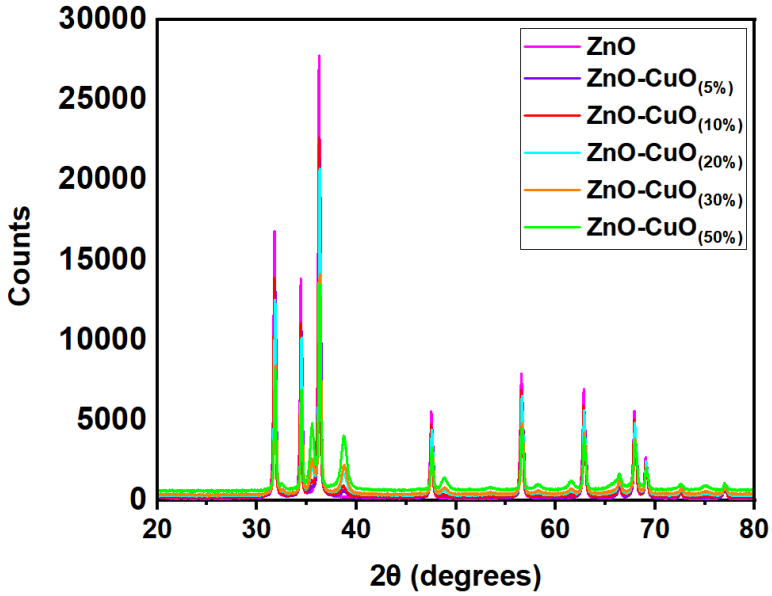


Figure 45 – Overlap of ZnO samples varying with CuO doping. Adapted from: [38].

Table 2 - Percentage ratio between the crystalline and amorphous parts of the samples**.**

Sample	% Crystalline	% Amorphous
CuO	55.9	44.1
TiO_2	81.0	19.0
TiO_2-CuO5%	80.1	19.9
TiO_2-CuO10%	80.0	20.0
TiO_2-CuO20%	79.9	20.1
TiO_2-CuO30%	75.7	24.3
TiO_2-CuO50%	65.9	34.1
ZnO	88.9	11.1
ZnO-CuO5%	88.5	11.5
ZnO-CuO10%	87.0	13.0
ZnO-CuO20%	84.1	15.9
ZnO-CuO30%	81.9	18.1
ZnO-CuO50%	78.7	21.3

Table 3 - Semi-quantitative percentage of compounds in the samples.

Sample	Composition	Percentage (%)
CuO	Tenorite	100
TiO_2	Anatase	79.3
	Rutile	20.7
TiO_2-CuO5%	Anatase	73.2
	Rutile	20.7
	Tenorite	6.1
TiO_2-CuO10%	Anatase	69.3
	Rutile	19,8
	Tenorite	10.9
TiO_2-CuO20%	Anatase	61.5
	Rutile	19.6
	Tenorite	18.9
TiO_2-CuO30%	Anatase	56.8
	Rutile	16.1
	Tenorite	27.1
TiO_2-CuO50%	Anatase	43.8
	Rutile	15.5
	Tenorite	40.7
ZnO	Zincite	100
ZnO-CuO5%	Zincite	94.4
	Tenorite	5.6
ZnO-CuO10%	Zincite	94.5
	Tenorite	5.5
ZnO-CuO20%	Zincite	90.2
	Tenorite	9.8
ZnO-CuO30%	Zincite	81.1
	Tenorite	18.9
ZnO-CuO50%	Zincite	69.4
	Tenorite	30.6

As can be seen in the tables above, Table 2 presents the percentage relationship between the amount of crystalline matter and the amount of amorphous matter present in the samples. Table 3 describes the compounds found in each sample, along with the semi-quantitative percentages of each compound.

The crystalline structure of copper oxide was identified as tenorite. Regarding titanium dioxide, two crystalline forms were observed: anatase and rutile. Finally, the crystalline structure of ZnO was identified as zincite.

In this way, it was possible to characterize the phases of the crystalline chemical compounds and obtain semi-quantitative values for each chemical compound in the thirteen samples.

Following the X-ray evaluations, the next subsection presents the results and discussion of the fluorescence technique.

4.4 Photon Intensity (XRF)

The XRF technique is based on the interaction between incident X-ray radiation and the atoms of the material, promoting the ejection of electrons from the inner layers and, consequently, the emission of characteristic radiation associated with each chemical element present in the sample.

In the context of semiconductor materials such as TiO_2, ZnO, and CuO, XRF analysis plays a fundamental role in the qualitative and quantitative identification of chemical elements, allowing verification of the purity, composition, and efficiency of the doping process. In particular, the incorporation of metallic dopants, such as copper (Cu), can be confirmed by the presence of characteristic peaks in the fluorescence spectrum, which correspond to the specific electronic transition energies of these elements [28,38].

Table 4 shows the samples analyzed. When analyzing ZnO doped with 5% CuO, a high degree of similarity to undoped ZnO was observed. Therefore, a total of 12 different samples were analyzed: 3 pure samples (Ti, Cu, and Zn), 5 Ti samples doped with Cu (concentrations of 5%, 10%, 20%, 30%, and 50% Cu), and 4 Zn samples doped with Cu (concentrations of 10%, 20%, 30%, and 50% Cu).

Table 4 - Samples analyzed (X-ray fluorescence).

Identification	Sample
Sample 1	Ti
Sample 2	Cu
Sample 3	Zn
Sample 4	Ti – Cu 5 %
Sample 5	Ti – Cu 10 %
Sample 6	Ti – Cu 20 %
Sample 7	Ti – Cu 30 %
Sample 8	Ti – Cu 50 %
Sample 9	Zn – Cu 10 %
Sample 10	Zn – Cu 20 %
Sample 11	Zn – Cu 30 %
Sample 12	Zn – Cu 50 %

Figures 46 and 47 show the samples (XRF) respectively: CuO, TiO_2, TiO_2-$CuO_{5\%}$, TiO_2-$CuO_{10\%}$, TiO_2-$CuO_{20\%}$, TiO_2-$CuO_{30\%}$, TiO_2-$CuO_{50\%}$; and ZnO, ZnO-$CuO_{10\%}$, ZnO-$CuO_{20\%}$, ZnO-$CuO_{30\%}$, ZnO-$CuO_{50\%}$. The spectra were evaluated in the energy range of 1 keV to 15 keV, since no intensities (photons/s) were found before and after these limits in any of the samples. To illustrate the doping effects of Ti and Zn according to the variation in the aforementioned concentrations, Figures 46 and 49 are shown. Finally, using Table 5, it was possible to obtain the concentrations of the oxides TiO_2, CuO, and ZnO.

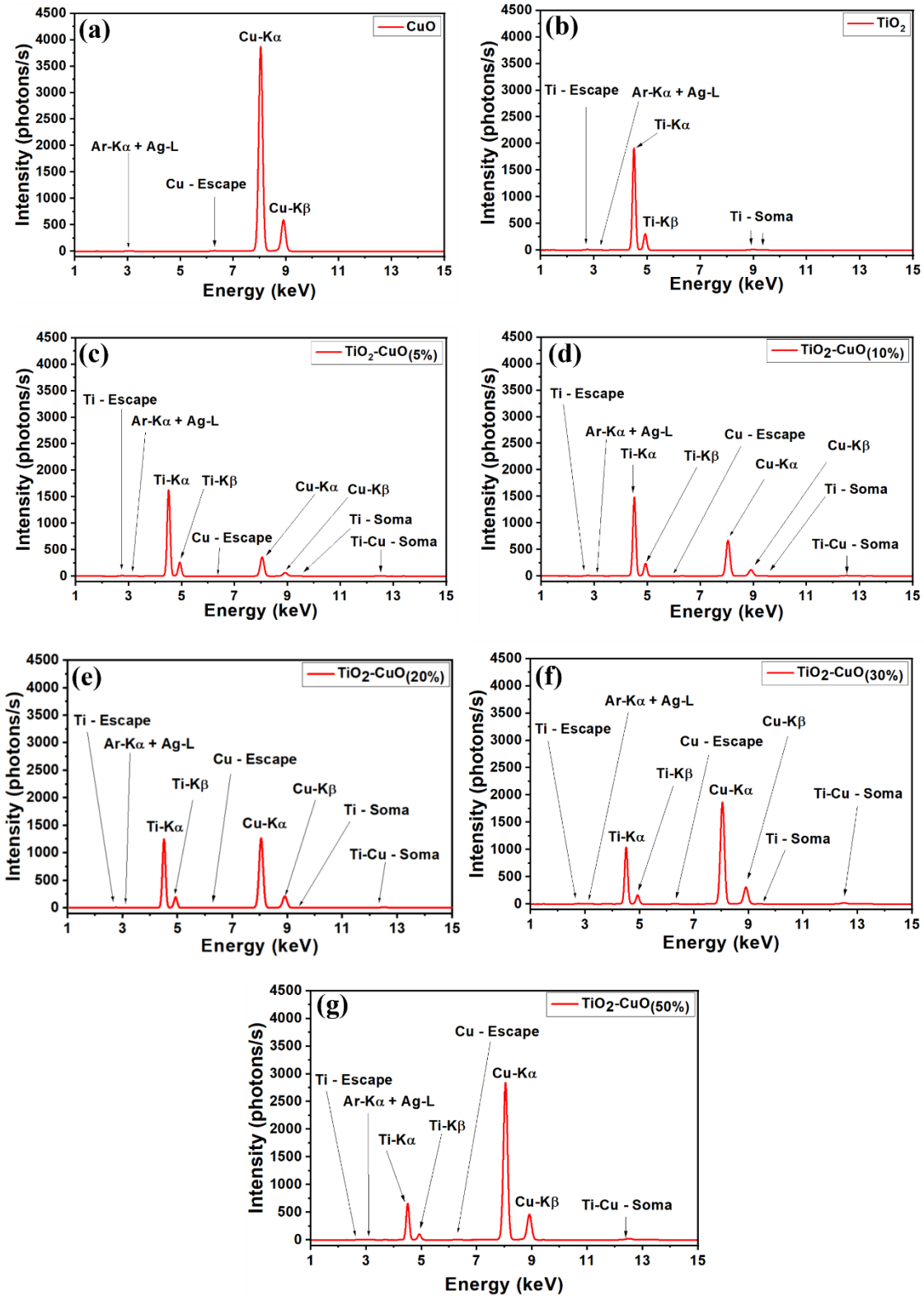


Figure 46 – Samples (XRF): (a) CuO, (b) TiO_2, (c) TiO_2-$CuO_{5\%}$, (d) TiO_2-$CuO_{10\%}$, (e) TiO_2-$CuO_{20\%}$, (f) TiO_2-$CuO_{30\%}$, (g) TiO_2-$CuO_{50\%}$. Adapted from: [38].

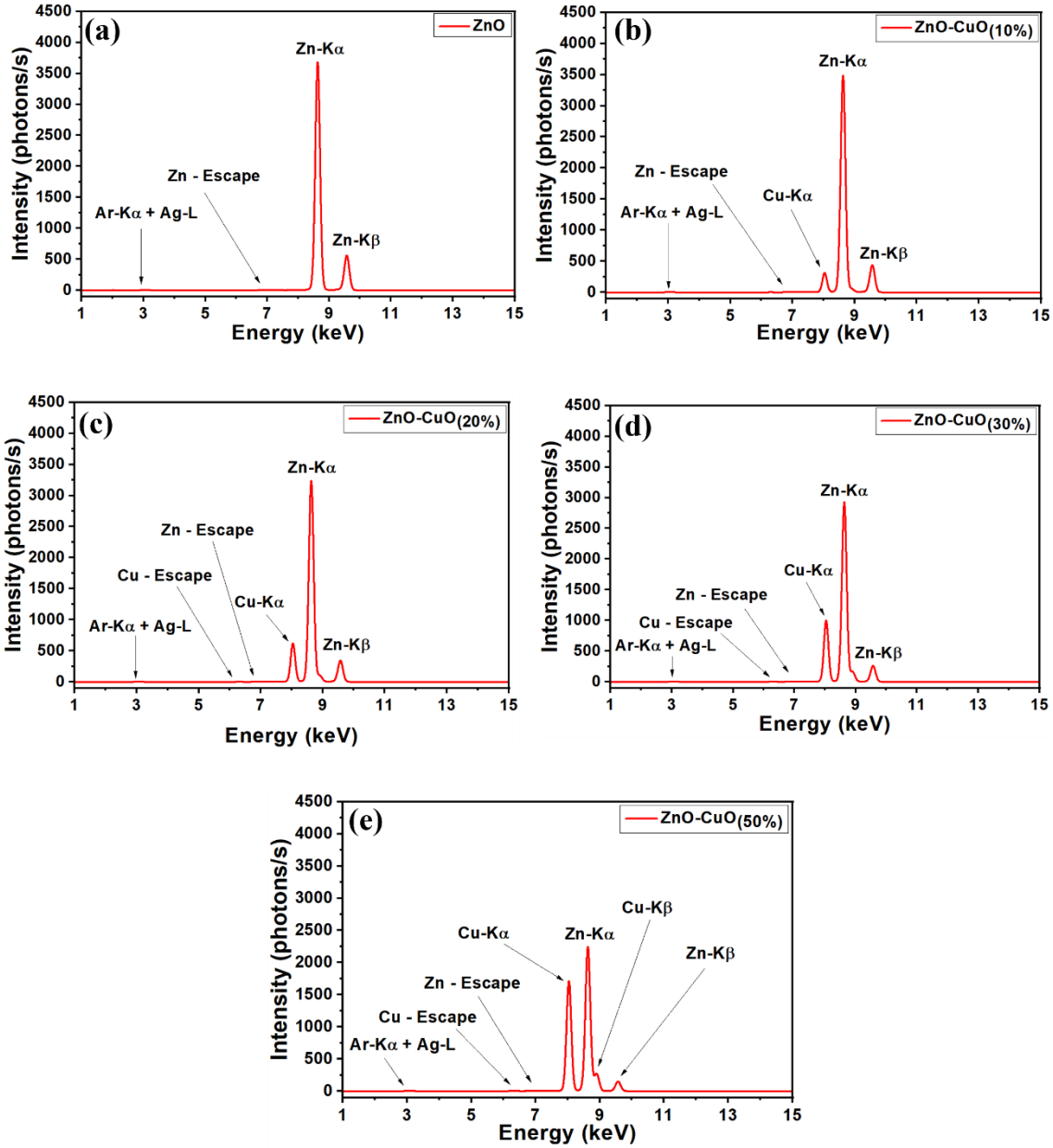


Figure 47 – Samples (XRF): (a) ZnO, (b) ZnO-$CuO_{10\%}$, (c) ZnO-$CuO_{20\%}$, (d) ZnO-$CuO_{30\%}$, (e) ZnO-$CuO_{50\%}$. Adapted from: [38].

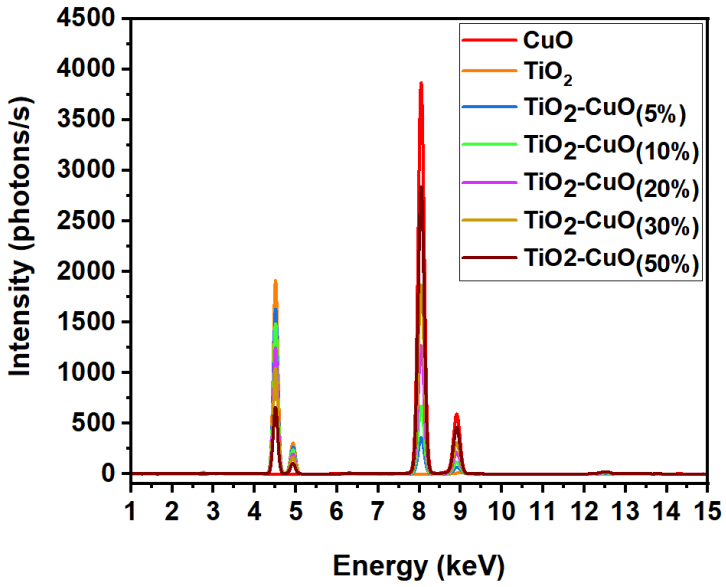


Figure 48 – XRF spectra of TiO_2 samples doped with CuO. Adapted from: [38].

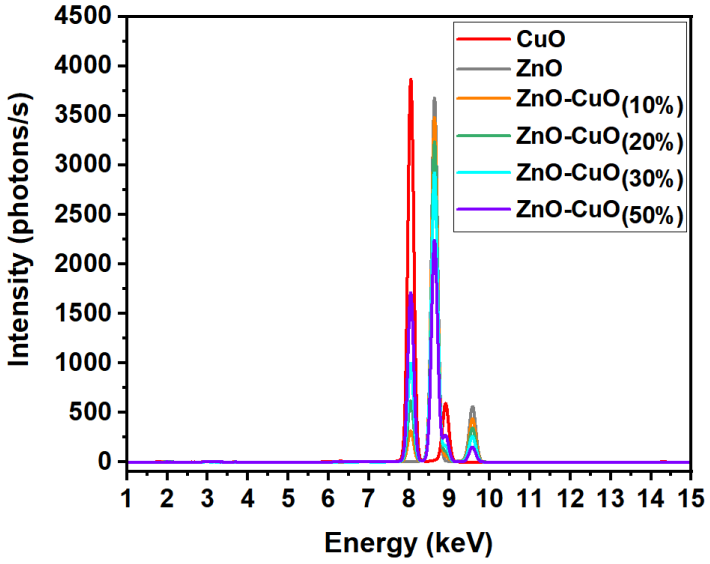


Figure 49 – XRF spectra of ZnO samples doped with CuO. Adapted from: [38].

Table 5 - Oxide concentration in the analyzed samples.

Sample	TiO_2 (%)	CuO (%)	ZnO (%)
Ti	99.6 ± 0.1	–	–
Cu	–	99.5 ± 0.2	–
Zn	–	–	99.5 ± 0.2
Ti – Cu 5%	94.5 ± 0.3	5.5 ± 0.3	–
Ti – Cu 10%	89.8 ± 0.2	10.2 ± 0.2	–
Ti – Cu 20%	80.5 ± 0.1	19.5 ± 0.1	–
Ti – Cu 30%	71.1 ± 0.3	28.9 ± 0.3	–
Ti – Cu 50%	52.9 ± 0.1	47.1 ± 0.1	–
Zn – Cu 10%	–	9.8 ± 0.4	90.2 ± 0.4
Zn – Cu 20%	–	19.4 ± 0.2	80.6 ± 0.2
Zn – Cu 30%	–	30.4 ± 0.1	69.6 ± 0.1
Zn – Cu 50%	–	50.2 ± 0.2	49.8 ± 0.2

It was possible to obtain the concentrations of the oxides TiO_2, CuO, and ZnO. Table 5 shows the oxide concentrations obtained in the XRF analyses of the analyzed samples. As mentioned before the graphical plots, Figures 46 to 49 show the XRF spectra of the analyzed oxide samples.

4.5 Surface Morphology (SEM)

Scanning electron microscopy (SEM) is one of the main morphological characterization techniques used in the investigation of materials used in photovoltaic devices, especially in DSSCs. This technique allows the acquisition of images with high spatial resolution, enabling detailed analysis of surface topography, particle size, granulometric distribution, porosity, and degree of agglomeration of semiconductor materials.

The morphological characterization of semiconductor oxides, such as TiO_2, ZnO, and their structures modified by doping with CuO, is extremely important, since the efficiency of the device is directly related to the surface area available for dye adsorption, the connectivity between particles, and the electron transport capacity [28,41,38]. The film morphology significantly influences electrolyte diffusion, charge

recombination, and the electron injection process, critical factors for photovoltaic performance.

To understand the desired results, comparisons were made with literature studies that obtained satisfactory results regarding the surfaces. Figure 50 shows the electrodes with chemical compositions similar to those developed in this work. For a reliable comparative analysis, the samples in this study were evaluated at the same scale (100 nm).

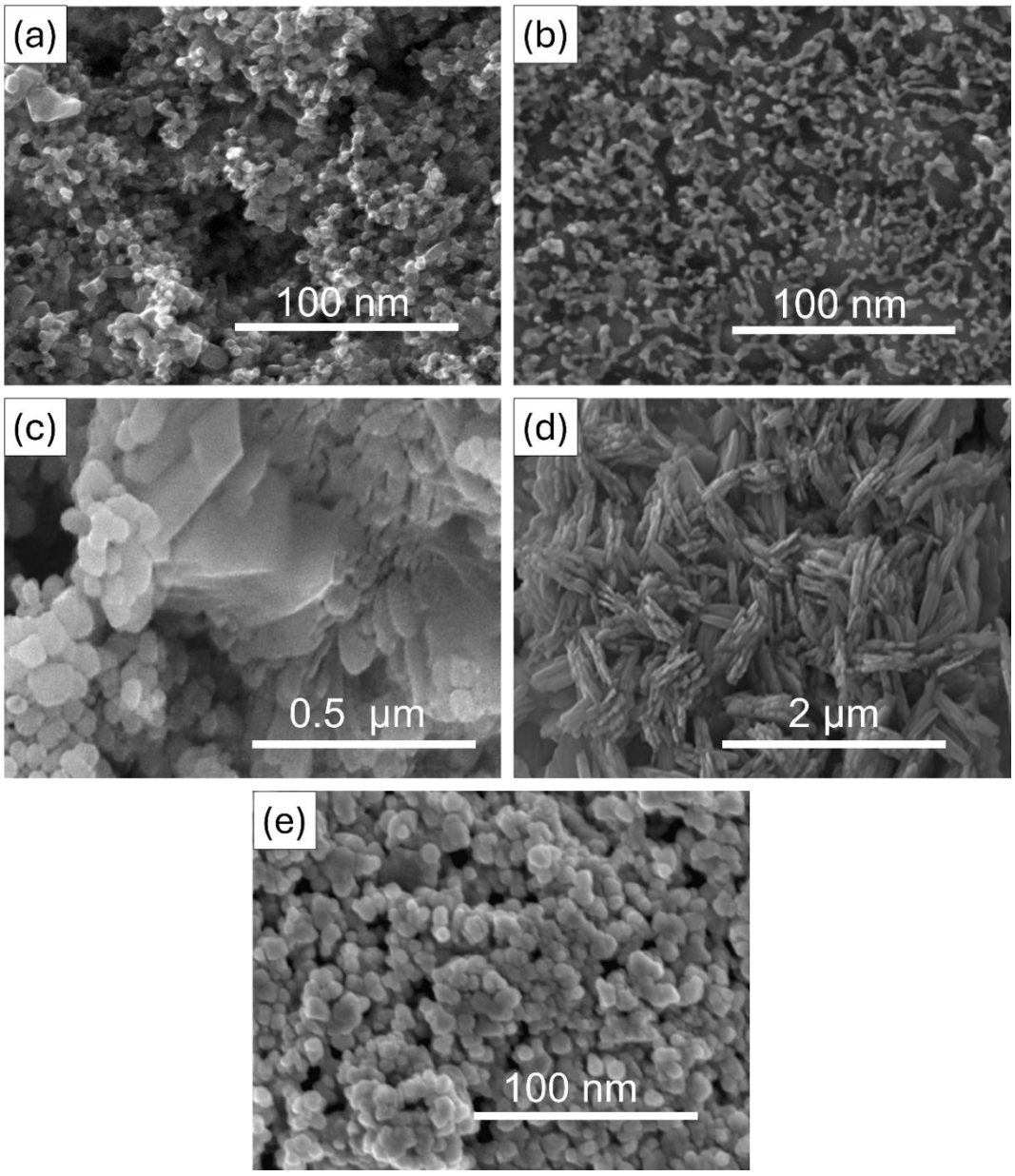


Figure 50 – Surface morphologies performed by SEM: (a) TiO_2 anode, (b) Pt cathode, (c) TiO_2-CuO anode, (d) ZnO-CuO anode, (e) ZnO [30,73,77-79].

For comparison with the images above provided in the literature, Figure 51 shows the TiO_2 and ZnO electrodes before they were doped with CuO.

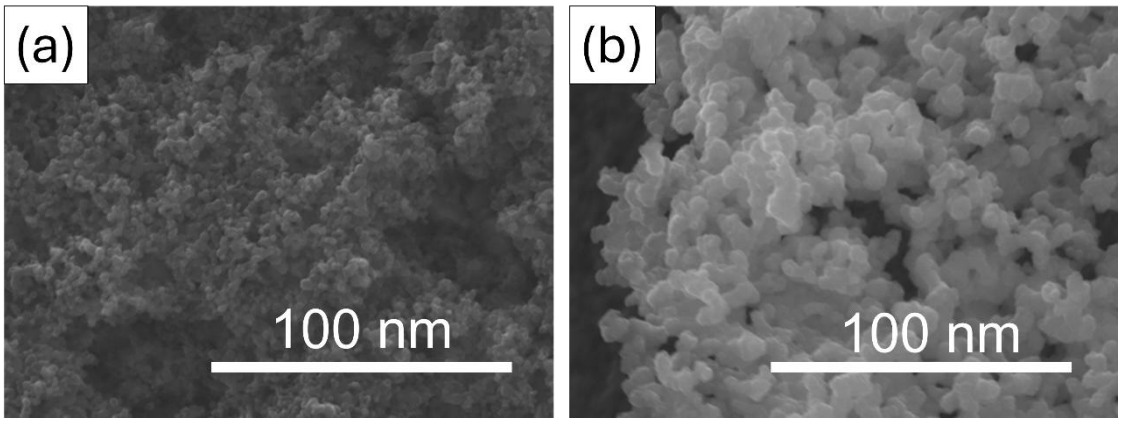


Figure 51 – Surface morphologies from this work performed using SEM: (a) TiO_2, (b) ZnO [38].

Both SEM micrographs (Fig. 51 (a) and Fig. 50 (a)) show typical structures of TiO_2 nanocrystalline films, characterized by aggregates of approximately spherical nanoparticles, with dimensions in the range of tens of nanometers. This morphology is highly desirable in DSSCs, as it promotes a high specific surface area, favoring the adsorption of the natural dye (*Vitis labrusca*) and increasing the active conditions for electron injection.

However, Figure 51 (a) shows a more homogeneous distribution of nanoparticulate aggregates, with fewer densely packed regions and better definition of particle boundaries. This characteristic suggests greater uniformity in film deposition, formation of a more accessible mesoporous network, facilitating electrolyte diffusion and reduction of recombination regions associated with structural defects or excessive agglomerations [29,30].

Figure 50 (a), although also showing a typical nanoparticulate structure, shows a greater tendency towards irregular agglomeration, with denser and less defined regions, which may result in a reduction of the effective surface area available for dye adsorption, difficulties in electrolyte percolation and possible increase in electronic recombination [38,67].

Both images demonstrate a nanocrystalline structure consistent with TiO_2 (anatase phase, typically obtained at ~450 °C), highly porous and interconnected morphology, and nanoscale (~100 nm), ideal for applications in DSSCs.

Figure 51 (a) can be associated with better control of synthesis and deposition parameters (example: paste viscosity, drying rate, heat treatment), resulting in a film with an optimized balance between porosity and electronic connectivity (a crucial factor for maximizing photovoltaic efficiency) [38,67].

The ZnO micrographs also exhibit characteristics typical of nanostructured semiconductor materials used in DSSCs, with approximately spherical particles organized in aggregates [38].

Figure 51 (b) shows a more uniform and less clustered morphology, with better distributed particles and less formation of dense clusters. This implies greater accessibility of the active surface to the dye, better electron injection due to the better-defined interface between dye and semiconductor, and more continuous electron transport paths, reducing charge traps.

In Figure 50 (e), greater coalescence and formation of agglomerates can be observed, which may limit the penetration of the dye into the pores, reduce the efficiency of dye-ZnO interaction and favor recombination processes. Both exhibit nanometric morphology compatible with photoelectrochemical applications and a porous structure with potential for dye adsorption [38,44,75]. The morphology shown in Figure 51 (b) presents a more efficient surface, with control over the nucleation and growth of ZnO particles. This is particularly relevant because ZnO is more susceptible to dissolution in acidic media (such as natural dyes), and a more homogeneous morphology can contribute to greater stability and performance of the DSSC.

The results indicate that, even before doping with CuO, the materials synthesized in this work (Figure 51) exhibit clear morphological advantages compared to those reported in the literature (Figure 50), especially in terms of structural homogeneity, particle size distribution, agglomeration control, and functional porosity (interconnected mesoporosity). These factors are crucial for increasing the adsorption of the natural dye, improving electron transport kinetics, reducing recombination, and consequently, increasing the photovoltaic efficiency of DSSCs [30,38]. Figure 52 shows the Pt cathode developed in this work.

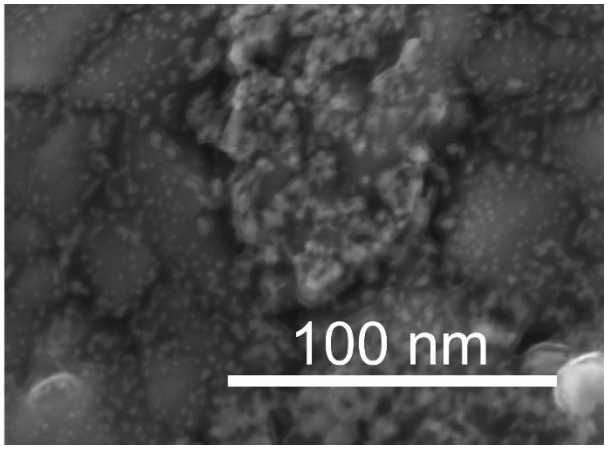


Figure 52 – Surface morphology of this work performed using SEM: Pt cathode [38].

SEM morphological analysis of the Pt surfaces shown in Figure 50 (b) and Figure 52 reveals fundamental characteristics related to catalytic activity at the DSSC counter electrode, especially in the redox electrolyte reduction process ($I_3^- \rightarrow I^-$).

Both micrographs show nanoparticulate structures distributed over the substrate, typical of Pt films obtained by thermal or chemical deposition, and the presence of a heterogeneous surface, essential for maximizing the catalytic active área [29,38]. A continuous surface network indicates good coverage of the conductive substrate (FTO). These characteristics confirm that both the electrode from the literature and the one developed in this work are functionally suitable for application in DSSCs.

Although both images show some similarity, Figure 52 highlights important advantages in morphology, such as greater dispersion of Pt nanoparticles. The surface presents a finer and more homogeneous distribution of nanoparticles, reducing the formation of large agglomerates. This implies a significant increase in the electrochemically active surface area (ECSA), and a greater number of catalytic sites accessible for the redox reaction [29,38,44]. Regarding the more refined surface texturing, a topography with well-distributed microdomains is observed. This suitable condition favors better electrode-electrolyte interaction and increased efficiency in charge transfer. Unlike Figure 50 (b), where there are indications of denser and partially coalesced regions, Figure 52 presents a more open and accessible structure, less blockage of active sites, and better electrolyte diffusion at the interface.

In other words, both microstructures (Fig. 50 (b) and Fig. 52) are suitable for application as counter electrodes in DSSCs, but Figure 52 presents clear morphological advantages, especially with regard to greater homogeneity in the distribution of nanoparticles, better accessibility of catalytic sites and a surface structure more favorable to redox kinetics. These factors make the Pt electrode developed in this work potentially superior in terms of electrocatalytic performance, directly contributing to the improvement of the photovoltaic efficiency of DSSCs.

As shown in Figure 51, the singularized anodes, Figures 53 and 54 respectively show the comparison of both TiO_2 and ZnO electrodes doped with CuO in different proportions.

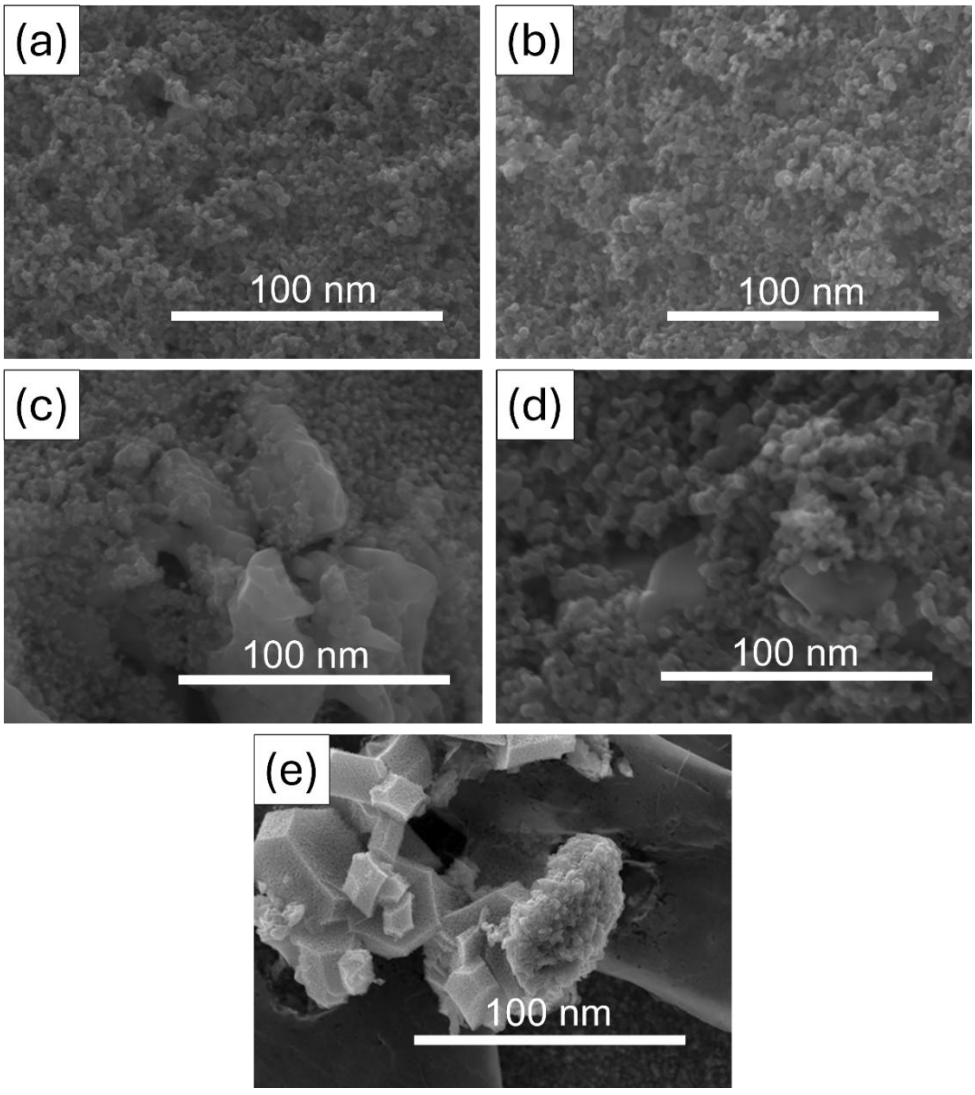


Figure 53 – Surface morphologies of TiO_2-CuO from this work performed by SEM at different concentrations: (a) 5%, (b) 10%, (c) 20%, (d) 30%, (e) 50% [38].

The comparison between the SEM micrographs in Figure 53 (a–e) (this work, with different CuO concentrations) and Figure 50 (c) (literature, fixed ratio 1:1) allows for an in-depth analysis of the morphological evolution as a function of CuO doping in TiO_2 and its impacts on the photoanode architecture in DSSCs. In general, both approaches present typical characteristics of TiO_2–CuO heterostructures, with the formation of interfaces between distinct semiconductor phases, fundamental for charge separation. However, the approach in this work (Figure 53) demonstrates a more refined and controlled morphological condition, clearly highlighting the effect of dopant concentration.

Figure 50 (c) shows the formation of larger and denser structures, with growth of CuO crystalline domains, evident phase segregation, with regions where CuO stands out as lamellar/plate structures, reduced uniformity of the TiO_2 matrix, possible impairment of surface area and electron percolation. Despite this, the image still maintains a certain homogeneity, with good surface coverage, which guarantees basic functionality in DSSCs.

Figure 53 (a) shows a morphology very similar to pure TiO_2, with fine and well-distributed nanoparticles, high porosity and interconnectivity. Compared to Fig. 50 (c), it shows better homogeneity and dispersion of the dopant, absence of CuO segregation and better preservation of the original TiO_2 structure. With this low doping, CuO acts as a dispersed active center, favoring charge separation and compromising the surface morphology.

Figure 53 (b) shows a slight increase in aggregate size, while maintaining good distribution and accessible porous structure. Compared to Fig. 50 (c), this figure is even more homogeneous and less agglomerated, providing better TiO_2–CuO integration (more efficient interface). With increasing doping, there is an intensification of the formation of local p–n heterojunctions, improving electron transport.

Figure 53 (c) shows the most suitable morphology, characterized by a balance between particle growth and maintenance of porosity, formation of well-distributed interfaces, and a structure highly accessible to the dye. Compared to Fig. 50 (c) and Fig. 53 (a), (b), the 20% doping with CuO is clearly superior, showing less phase segregation, better CuO distribution, and a larger active area. This is the point where maximum efficiency in charge separation (heterojunction effect) occurs, an optimal

relationship between surface area and electronic connectivity, and minimization of recombination. Unlike the 1:1 ratio (Fig. 50(c), Fig. 53 (d) and (e)), here the system avoids excess CuO, maintaining the functionality of TiO_2 as a carrier matrix.

Figure 53 (d) shows the beginning of more evident morphological changes, with increased agglomeration and the emergence of denser regions. Compared to Fig. 50 (c), it is still more homogeneous than in the literature, but it begins to approach segregation behavior. CuO(30%) doping begins to block active sites, reduce the effective surface area, and introduce recombination centers.

Figure 53 (e) shows the presence of larger, crystalline CuO structures, phase segregation, and reduced uniformity. Compared to Fig. 50 (c), it shows high structural similarity; however, it still exhibits better distribution and a lower degree of extreme coalescence. In this case, the dopant saturation region is observed, where CuO ceases to act as a dopant and begins to dominate the morphology, compromising electron transport in TiO_2 and increasing recombination.

The comparison shows that the approach in the literature (Fig. 50 (c), 1:1) represents a morphologically saturated system with clear structural limitations, whereas the present work (Fig. 53) demonstrates a systematic and progressive control of doping, allowing the identification of the optimal behavior of the material.

Therefore, it was observed that doping from 5% to 20% (Fig. 53 a–c) resulted in progressive improvement in morphology, increased potential efficiency, and ideal heterojunction formation, while for cases ≥ 30% (Fig. 53 d–e) there was the onset of structural degradation, undesirable agglomeration, and saturation. Figure 54 follows, showing the CuO doping performed this time on ZnO.

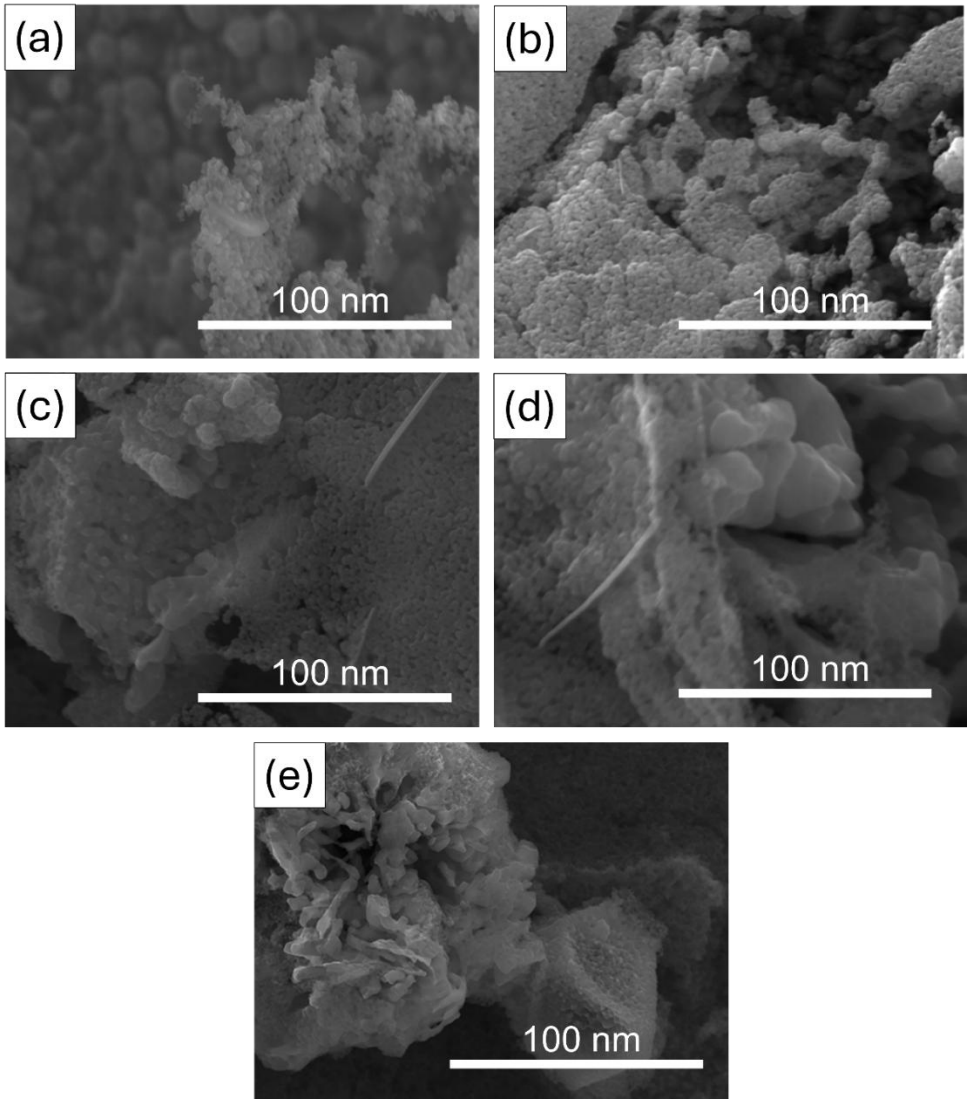


Figure 54 – Surface morphologies of ZnO-CuO from this work performed by SEM at different concentrations: (a) 5%, (b) 10%, (c) 20%, (d) 30%, (e) 50% [38].

The comparative analysis between Figure 50 (d) (literature, fixed ratio ZnO:CuO = 1:1), Figure 53 (a–e) (TiO_2–CuO) and Figure 54 (a–e) (ZnO–CuO, this work) shows a highly consistent morphological behavior in CuO-doped systems, allowing us to establish a clear trend of structural optimization as a function of dopant concentration. Figure 50 (d) presents a typical morphology of saturated systems, characterized by excessive growth of CuO domains, formation of denser structures and evidence of phase segregation, although it still maintains a relatively homogeneous and functional coverage of the substrate. In contrast, Figures 54 (a–c), as previously observed for the TiO_2–CuO system in Figures 53 (a–c), demonstrate a progressive evolution of

morphology with increasing CuO concentration from 5% to 20%, where initially (5%) a predominantly nanometric and highly porous structure is observed, with excellent dopant dispersion, followed by (10%) an intensification of heterojunction formation without significant loss of homogeneity; and culminating at (20%) an optimal condition, in which there is an ideal balance between surface area, electronic connectivity and CuO distribution, favoring the efficient formation of p–n interfaces and maximizing the potential performance in DSSCs.

This behavior is analogous to that observed in the TiO_2–CuO system (Figure 53), reinforcing that controlled doping up to ~20% promotes a superior functional architecture in different semiconductor matrices. However, from higher concentrations (30% and 50%), as evidenced in Figures 54 (d–e) and also in 53 (d–e), a clear saturation process of the system is observed, with increased agglomeration, growth of larger structures attributed to CuO, and reduction of effective porosity, resulting in less favorable morphologies. In this condition, CuO ceases to act as an efficient dopant and begins to dominate the microstructure, a behavior similar to that observed in Figure 50 (d), although the materials in this work generally exhibit better morphological control and a lower degree of extreme coalescence.

Thus, it is concluded that CuO doping in ZnO follows the same trend observed for TiO_2, presenting an optimal range up to approximately 20%, and that above this percentage (30% and 50%) structural degradation occurs, compromising essential properties such as dye adsorption, charge transport, and photovoltaic performance.

4.6 Electrode Structures (AFM)

Nanoscale structural characterization plays a fundamental role in understanding the performance of DSSCs, since the properties of particle distribution, grain size, and structural uniformity directly influence key processes such as dye adsorption, charge transport, and electronic recombination. In this context, Atomic Force Microscopy (AFM) stands out as an indispensable tool for the three-dimensional analysis of the surface of the semiconductor materials used, such as TiO_2, ZnO, and their CuO-doped structures. In the context of semiconductor doping, such as the incorporation of CuO into TiO_2 and ZnO matrices, AFM allows the identification of structural modifications

resulting from the introduction of the dopant, such as variations in particle distribution, cluster formation, and alterations in surface homogeneity. These changes can significantly impact electron mobility and recombination mechanisms, and are therefore crucial for the interpretation of the electrochemical and photovoltaic results obtained [29].

Thus, the use of AFM in this study provides a solid basis for comparative analysis between different compositions and doping levels, allowing the establishment of direct relationships between the surface nanostructure and the performance of DSSCs. The results obtained are presented and discussed below, with emphasis on the correlation between morphological parameters and the functional properties of the investigated materials.

When performing the procedures, it is emphasized that to obtain satisfactory dye adsorption results on the substrate, it is necessary that there are cavities or pores in the thin film of the nanostructure, and that there are homogeneous and mesoporous coatings throughout the substrate, without any elevations or large craters in the anodic film [29,67]. For comparison regarding the structural surface topography to what is intended, some anodes and cathodes available in the literature can be observed, as shown in Figure 55.

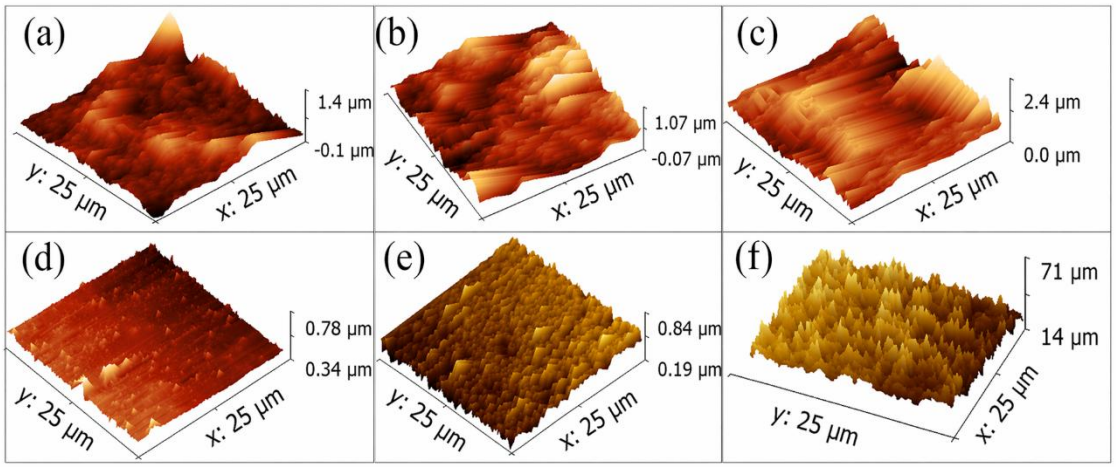


Figure 55 – TiO_2 anodes by spin coating technique: (a), (b) and (c). Pt cathodes by drop casting technique: (d), (e) and (f) [29,80,71].

For a better result, it is desirable that the generated images be very uniform, as can be seen in Figure 55 (a), (b) and (c). This is because a uniform film hinders the chances of recombination processes along it. The spin coating method also allows greater control of the thickness and smoothness of the thin film and is less subject to non-uniformity when compared to the scraper blade method, as is the drop casting method for cathodes, as shown in Figure 55 (d), (e) and (f) [29]. Figure 55 (f) showed better structural morphology compared to Figure 55 (d) and (e), as it showed the formation of pores suitable for electrolyte allocation, providing better electron transport.

The conversion efficiency of DSSCs depends on several factors present in the manufacturing process. Therefore, great attention must be paid to each stage of construction to achieve maximum conversion efficiency using the components employed. Anodes composed of nanostructured semiconductor oxides have a very important influence on photovoltaic performance [28,38], and for this reason, TiO_2 and ZnO oxides were used in this work to analyze photovoltaic performance according to evaluations on each anodic surface. For the cathodes, a Pt solution was used. Figure 56 illustrates the results of the measurements in this study, firstly after CuO doping on TiO_2.

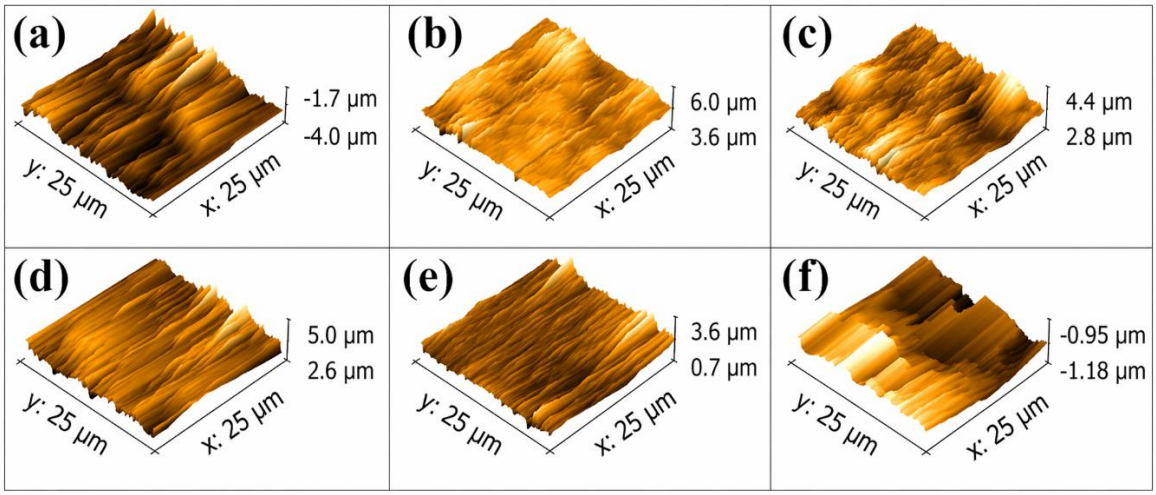


Figure 56 – Anode AMFs: (a) TiO_2, (b) TiO_2-$CuO_{5\%}$, (c) TiO_2-$CuO_{10\%}$, (d) TiO_2-$CuO_{20\%}$, (e) TiO_2-$CuO_{30\%}$, (f) TiO_2-$CuO_{50\%}$ [38].

In Figure 56 (a) it is possible to observe the image showing the surface topology of a thin film composed solely of TiO_2, at the 25 µm scale, which, incidentally, presents a good result, which is one of the justifications for these oxides being well employed in the development of DSSCs [94,95]. Its surface demonstrates uniformity and at the same time adequate porosity, contributing to good dye adsorption and good electron flow in the semiconductor due to the porosity that will be occupied by the electrolytic solution. Similarly, through Figure 56 (b), it is possible to observe a slight improvement in the surface for the hybrid compound. Naturally, as the CuO doping was carried out, the surfaces underwent changes. It can be seen that from Figure 56 (a) to (e), the changes occur in a less pronounced way. In the transition from 30% doping to 50%, certain irregularities are noted that can compromise the solar cells' ability to perform well. This transition can be understood as a saturation region [95,97]. In general, with the exception of Figure 56 (f), the anodes presented surfaces with potential. In fact, when compared to those shown in Figure 55 (a), (b), and (c) provided in the literature which were already considered adequate, those developed in the study are slightly better, especially those in Figure 55 (a) and (b). Similarly, Figure 57 shows the results of CuO doping performed on ZnO, and Figure 58 shows the cathode.

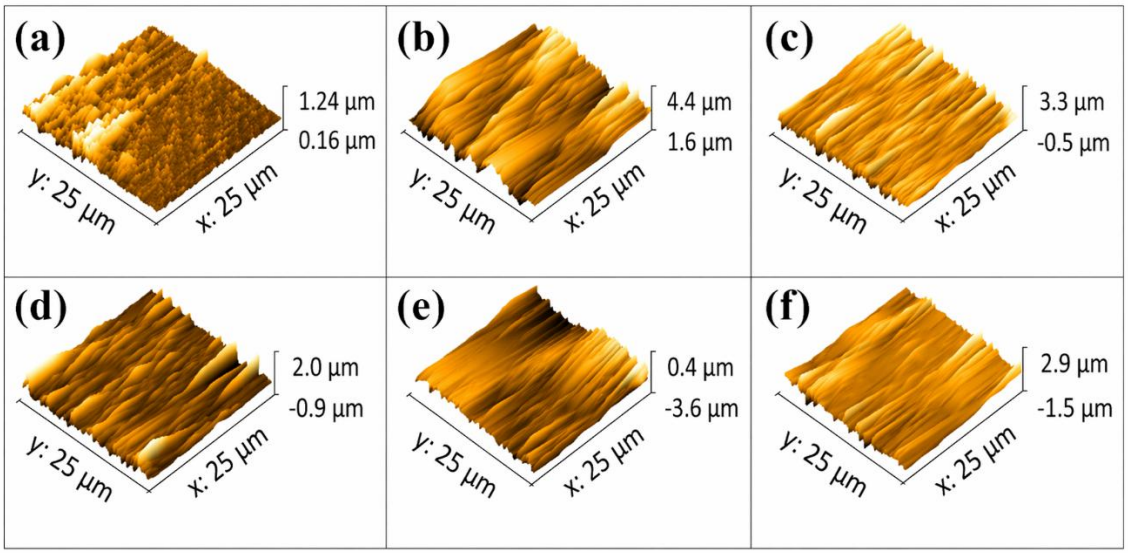


Figure 57 – Anode AMFs: (a) ZnO, (b) ZnO-$CuO_{5\%}$, (c) ZnO-$CuO_{10\%}$, (d) ZnO-$CuO_{20\%}$, (e) ZnO-$CuO_{30\%}$. (f) ZnO-$CuO_{50\%}$ [38].

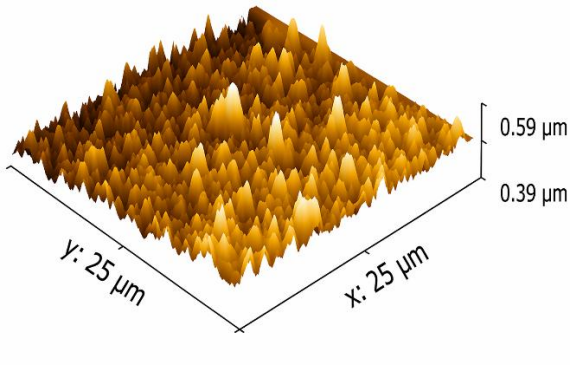


Figure 58 – Pt cathode (AFM) [38].

Just as Figure 56 (a)-(e) showed excellent results related to suitable surfaces for good electrolyte allocation and electrochemical interaction between the oxide and dye, CuO doping on ZnO anodes also demonstrated promising potential in their structures. However, it is noticeable that in this case, significant surface saturation begins to occur in the transition from 20% to 30%, as shown in Figure 57 (d)-(e). Furthermore, visible saturation was also observed at 50% doping, as also occurred in Figure 56 (f). Compared to Figure 55 (a)-(c), the surfaces in this study also showed a slight improvement, approaching, for example, Figure 55 (c), which appears to have been the surface with the best regularity. In the case of the cathode, shown in Figure 58, it is noticeable that the FTO coated with platinum solution was very similar to the cathode provided in the literature, illustrated in Figure 55 (f), which, incidentally, in its structural form, was more effective in the electrochemical reduction process than Figure 55 (d) and (e). That is, of the three cathodes presented in the literature, the most suitable was that of Figure 55 (e), which was the closest to the cathode developed in this study; therefore, the deposition technique applied did indeed demonstrate conditions favorable to the expected result. Through these analyses, it is possible to estimate, for example, that the oxidations and electrochemical interactions will possibly undergo changes according to the transitions on some surfaces. A suitable surface is one of the parameters considered fundamental for DSSCs to have good photovoltaic conversion.

4.7 Current Density (J-V Curve)

The electrochemical characterization of photovoltaic properties in DSSCs is fundamental to understanding the charge transport and electronic recombination mechanisms in the semiconductor materials used. In this context, current density versus potential (J–V) curves constitute one of the most important tools for evaluating device performance.

In the present study, J–V curves were obtained for TiO_2 and ZnO-based systems modified by different CuO doping concentrations, ranging from the undoped condition to 50% by mass, as shown in Figure 59. The introduction of CuO, a p-type semiconductor with lower bandgap energy (~1.5 eV), into n-type semiconductor matrices such as TiO_2 (~3.2 eV) and ZnO (~3.3 eV), promotes the formation of heterostructures that favor the separation of photogenerated charges, reducing recombination processes and expanding the spectral response of the devices [41-43].

Comparative analysis of these curves allows for a systematic investigation of the effect of CuO concentration on the electrical behavior of DSSCs. At low doping concentrations, an improvement in electron transport and charge collection is expected, attributed to the formation of preferential conduction paths and a more favorable energy alignment between the materials. On the other hand, at higher concentrations, adverse effects may occur, such as the formation of recombination centers and saturation of the active surface, compromising photovoltaic performance [28,38,41].

Therefore, discussing the results of the J–V curves across different CuO proportions becomes essential for identifying the optimal doping condition, as well as for understanding the structural and electronic limits of these systems, contributing to the advancement in the development of more efficient and stable DSSCs.

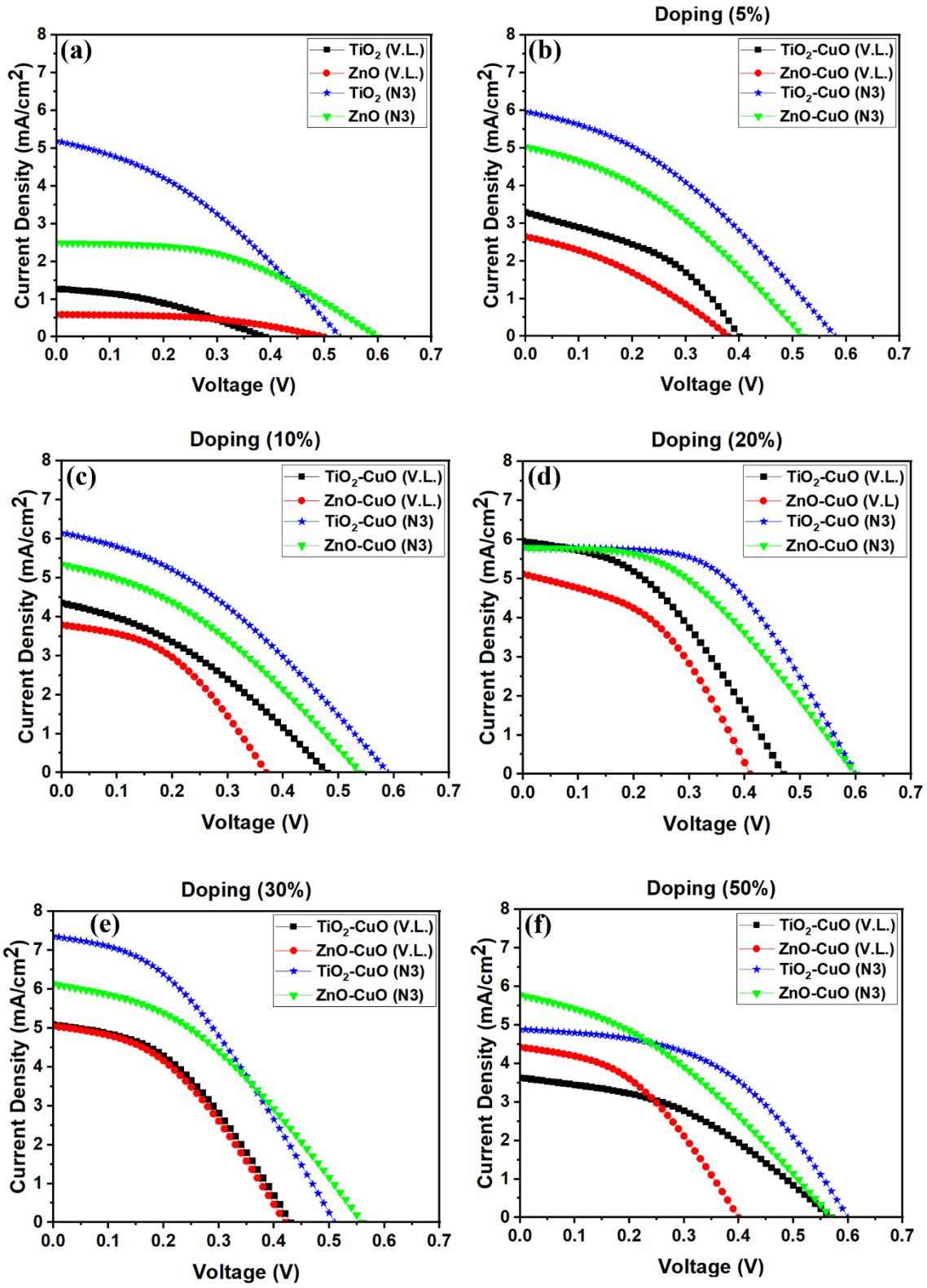


Figure 59 – J-V curves of CuO doping in TiO_2 and ZnO: (a) no doping, (b) 5%, (c) 10%, (d) 20%, (e) 30%, and (f) 50% [38].

Figure 59 shows the J–V curves of TiO_2 and ZnO based DSSCs, sensitized with V.L. and N3 dyes, for different CuO doping levels: (a) 0%, (b) 5%, (c) 10%, (d) 20%, (e) 30%, and (f) 50%. In general, it is observed that the progressive introduction of CuO initially promotes a shift in the curves towards regions of higher current density and, in several cases, also higher open-circuit voltage, evidencing an improvement in photovoltaic performance. This behavior is more pronounced up to 20% doping, a condition in which the system achieves the best balance between generation, transport, and collection of charges. Starting at 30%, the beginning of a saturation process is noticeable, and at 50% a partial loss of performance is observed in virtually all configurations, suggesting an excess of CuO phase, increased interfacial defects, obstruction of active sites, and intensification of electronic recombination.

In the undoped case, Figure 59 (a), the devices exhibit the lowest overall performance. For TiO_2 (V.L.), the black curve shows Jsc ≈ 1.3 mA/cm² and Voc ≈ 0.38–0.39 V, with a rather modest profile and relatively early current drop. For ZnO (V.L.), the red curve is even lower, with Jsc ≈ 0.6 mA/cm² and Voc ≈ 0.50 V, indicating very limited photogenerated current. With the N3 dye, the behavior improves substantially: TiO_2 (N3), blue curve, reaches Jsc ≈ 5.1 mA/cm² and Voc ≈ 0.50–0.51 V, clearly the best undoped condition; While ZnO(N3), green curve, shows Jsc ≈ 2.4–2.5 mA/cm² and Voc ≈ 0.56–0.57 V. Thus, even under reference conditions, N3 surpasses the V.L. in both semiconductors, and TiO_2 surpasses ZnO in current density, although ZnO(N3) shows a slight advantage in Voc. In other words, without CuO, the main limitation seems to be in the charge injection and transport capacity, especially in films sensitized with V.L.

With 5% CuO, Figure 59 (b), a clear and simultaneous improvement occurs in all curves. TiO_2-CuO (V.L.) rises to Jsc ≈ 3.3 mA/cm² and Voc ≈ 0.39–0.40 V, which represents a significant increase in current compared to undoped TiO_2, although the voltage varies little. ZnO-CuO (V.L.) also improves significantly, reaching Jsc ≈ 2.6 mA/cm² and Voc ≈ 0.37–0.38 V; in this case, the current gain is large, but there is a reduction in Voc compared to pure ZnO with V.L., suggesting that the low doping favors collection, but does not yet fully stabilize interfacial alignment. For TiO_2-CuO (N3), a quite robust blue curve is observed, with Jsc ≈ 5.9–6.0 mA/cm² and Voc ≈ 0.56 V, superior to that of pure TiO_2, both in current and voltage. Similarly, ZnO-CuO (N3)

achieves Jsc ≈ 5.0 mA/cm² and Voc ≈ 0.53–0.54 V, practically doubling the current compared to undoped ZnO with N3. Therefore, even at 5%, CuO acts in a clearly beneficial way, especially in ZnO, which was the most limited system in the undoped condition. The order of performance at 5% becomes approximately: TiO_2-CuO (N3) > ZnO-CuO (N3) > TiO_2-CuO (V.L.) > ZnO-CuO (V.L.).

Under the 10% CuO condition, Figure 59 (c), the improvement trend continues. TiO_2-CuO (V.L.) increases to Jsc ≈ 4.4 mA/cm² and Voc ≈ 0.47–0.48 V, showing further improvement not only in current but also in voltage, indicating a more effective reduction in recombination losses and better charge extraction. ZnO-CuO (V.L.) reaches Jsc ≈ 3.8 mA/cm² and Voc ≈ 0.37–0.38 V; despite the consistent increase in current, the voltage remains lower, indicating that the system still faces energy or interfacial limitations. The TiO_2-CuO (N3) reaches Jsc ≈ 6.1 mA/cm² and Voc ≈ 0.58–0.59 V, establishing itself as one of the best curves in the set. The ZnO-CuO (N3) also increases to Jsc ≈ 5.3 mA/cm² and Voc ≈ 0.52–0.53 V. Comparing 5% and 10%, it is observed that both semiconductors continue to respond positively to the increase in CuO content, but TiO_2, especially with N3, responds more efficiently, with more “rectangular” curves, which also suggests an improvement in the form factor, even though it was not explicitly calculated in the figure.

The most relevant point occurs at 20% doping, Figure 59 (d), which visually stands out as the best overall case. Under this condition, TiO_2-CuO (V.L.) reaches Jsc ≈ 5.9–6.0 mA/cm² and Voc ≈ 0.46–0.47 V, representing a very significant gain compared to undoped TiO_2, with a more than fourfold increase in short-circuit current. ZnO-CuO (V.L.) rises to Jsc ≈ 5.1 mA/cm² and Voc ≈ 0.40–0.41 V, becoming much more competitive than under the previous conditions. TiO_2-CuO (N3) exhibits one of the highest and most stable curves in the entire figure, with Jsc ≈ 5.9–6.0 mA/cm² and Voc ≈ 0.60–0.61 V. Although the initial current is similar to that of TiO_2-CuO(V.L.), the crucial difference lies in the fact that the blue curve maintains high currents up to higher voltages, resulting in a clearly superior area under the curve and, consequently, a higher probable maximum power. ZnO-CuO (N3) also exhibits excellent performance, with Jsc ≈ 5.8–5.9 mA/cm² and Voc ≈ 0.60 V. In comparative terms, panel (d) shows the most balanced scenario between high current and high voltage for almost all formulations, which supports the interpretation that 20% CuO constitutes the optimal

concentration. Physically, this suggests that, up to this limit, CuO promotes favorable heterojunctions, enhances absorption, and/or facilitates charge separation, without yet causing structural saturation or an excess of recombinant centers.

When increasing to 30% CuO, Figure 60 (e), although some curves remain high, clear signs of the beginning of saturation appear. TiO_2-CuO (V.L.) shows Jsc ≈ 5.1 mA/cm² and Voc ≈ 0.41–0.42 V, decreasing in both current and voltage compared to 20%. ZnO-CuO (V.L.) is very close, with Jsc ≈ 5.0–5.1 mA/cm² and Voc ≈ 0.40–0.41 V, indicating a behavior almost equivalent to that of TiO_2 with V.L., but still short of the best performance obtained at 20%. The TiO_2-CuO (N3) achieves the highest visual Jsc in the entire figure, approximately 7.3 mA/cm², but with Voc ≈ 0.50 V, lower than in the 20% doping case. This means there was a current gain, but at the cost of voltage loss, which does not always translate into higher overall efficiency. The ZnO-CuO (N3) exhibits Jsc ≈ 6.0–6.1 mA/cm² and Voc ≈ 0.55 V, also lower, overall, than the 20% case. This point is central to the discussion: although the 30% doping still maintains high currents, especially with N3, the decrease in Voc and the less favorable shape of the curves indicate that the system begins to suffer from excess CuO. In a photovoltaic performance analysis, the best device is not necessarily the one with the highest isolated Jsc, but the one that most harmoniously combines Jsc, Voc, and FF. From this perspective, 20% remains higher than 30%.

In the extreme condition of 50% CuO, Figure 59 (f), the saturation process becomes even more evident. TiO_2-CuO (V.L.) drops to Jsc ≈ 3.6–3.7 mA/cm² and Voc ≈ 0.56–0.57 V. Although Voc is relatively high, the reduced current shows that the excess CuO has begun to impair electron transport or electron injection. ZnO-CuO (V.L.) shows Jsc ≈ 4.4 mA/cm² and Voc ≈ 0.40 V, remaining below the best-case scenario at 20%. TiO_2-CuO (N3) drops sharply to Jsc ≈ 4.8–4.9 mA/cm² and Voc ≈ 0.60 V, losing the superiority observed at 20–30%. ZnO-CuO (N3), in turn, shows Jsc ≈ 5.7–5.8 mA/cm² and Voc ≈ 0.56–0.57 V, still relatively high, but already below the optimum behavior at 20%. In summary, the increase to 50% does not sustain the gains observed at intermediate concentrations; on the contrary, it indicates that the excess CuO begins to act as a limiting factor, possibly due to the formation of agglomerates, pore blockage, excessive coating of the active surface, unfavorable modification of electron percolation, and increased interfacial recombination.

Specifically comparing the evolution of TiO_2 with V.L., the approximate values of Jsc follow the sequence 1.3 → 3.3 → 4.4 → 5.9 → 5.1 → 3.6 mA/cm² for 0, 5, 10, 20, 30, and 50%, respectively, while Voc varies from approximately 0.38 → 0.40 → 0.47 → 0.47 → 0.42 → 0.56 V. This series shows that the large gain promoted by CuO occurs mainly up to 20%, when the current almost quadruples compared to the undoped material. After that, the drop in Jsc at 30% and 50% indicates saturation. For ZnO with V.L., the evolution of Jsc is approximately 0.6 → 2.6 → 3.8 → 5.1 → 5.0 → 4.4 mA/cm², with Voc ≈ 0.50 → 0.38 → 0.37 → 0.40 → 0.40 → 0.40 V. In this case, the main benefit of doping is strongly associated with the increase in current, but without a significant voltage increase. Even so, the improvement of up to 20% is unequivocal.

For the system with N3, the gains are even more evident. In TiO_2(N3), the Jsc sequence is approximately 5.1 → 5.9 → 6.1 → 5.9 → 7.3 → 4.8 mA/cm², while Voc evolves approximately as 0.50 → 0.56 → 0.58 → 0.60 → 0.50 → 0.60 V. Although the 30% condition exhibits the highest Jsc, the most balanced set remains 20%, as it combines high current with the highest voltage plateau and a more favorable curve shape. In ZnO(N3), the Jsc sequence is approximately 2.5 → 5.0 → 5.3 → 5.8 → 6.0 → 5.7 mA/cm², with Voc ≈ 0.56 → 0.54 → 0.53 → 0.60 → 0.55 → 0.56 V. Here too, 20% represents the best compromise between the parameters, while 30% and 50% indicate partial maintenance of the current gain, but with loss of the overall optimum condition.

From a mechanistic point of view, the results indicate that doping with CuO in moderate amounts improves performance through several complementary pathways: formation of p–n heterostructures between CuO and TiO_2/ZnO, favorable modification of band alignment, increased electron-hole pair separation, creation of alternative charge transport pathways, and possible amplification of the photoanode's optical response [38,41,42]. However, when the CuO fraction becomes excessive, this benefit ceases to grow and becomes counterproductive. Excess CuO can introduce less efficient electrical regions, act as a recombination center, reduce the connectivity of the host semiconductor's main transport network, and compromise dye adsorption or electrolyte infiltration [28,38]. This explains why, experimentally, the improvement is progressive up to 20%, and why, from 30% onwards, the system enters a saturation regime.

Therefore, detailed analysis of the J–V curves consistently demonstrates that doping with CuO was effective in improving the photovoltaic performance of both TiO_2

and ZnO, but only up to an optimum limit. Among all the conditions analyzed, 20% CuO constitutes the best balance between high current density, high open-circuit voltage, and the most favorable curve profile, thus being the most promising condition for application in DSSCs. The samples with 30% and 50% still preserve some of the gains obtained compared to the undoped material, but already clearly reveal the saturation effects, confirming that optimizing the dopant concentration is crucial to maximizing the device's efficiency.

4.8 Power (P-V Curve)

The analysis of power-versus-voltage (P-V) curves is an essential tool for evaluating the photovoltaic performance of Grätzel cells, as it allows for the direct determination of the maximum power point (Pmax) and, consequently, the energy conversion efficiency of the devices. Unlike J-V curves, which provide fundamental parameters such as short-circuit current density (Jsc) and open-circuit voltage (Voc), P-V curves offer a more direct view of the actual electrical energy generation capacity under operating conditions, being particularly relevant for comparative analysis between different photoanode compositions.

The aim is to understand how the progressive incorporation of CuO influences the balance between beneficial mechanisms, such as increased optical absorption and improved charge separation, and the deleterious effects associated with excess dopant, such as the formation of recombinant centers, particle agglomeration, and reduction of the active surface área [43]. In this sense, the analysis of P-V curves allows us to identify not only the optimal doping condition, but also the threshold from which saturation or degradation of photovoltaic performance occurs. Thus, this subsection aims to present and discuss, in detail, the evolution of the electrical behavior and power generated by DSSCs as a function of CuO concentration, establishing correlations between the structure, electronic properties, and energy efficiency of the devices. Figure 60 shows the results of the (P-V) curves.

.

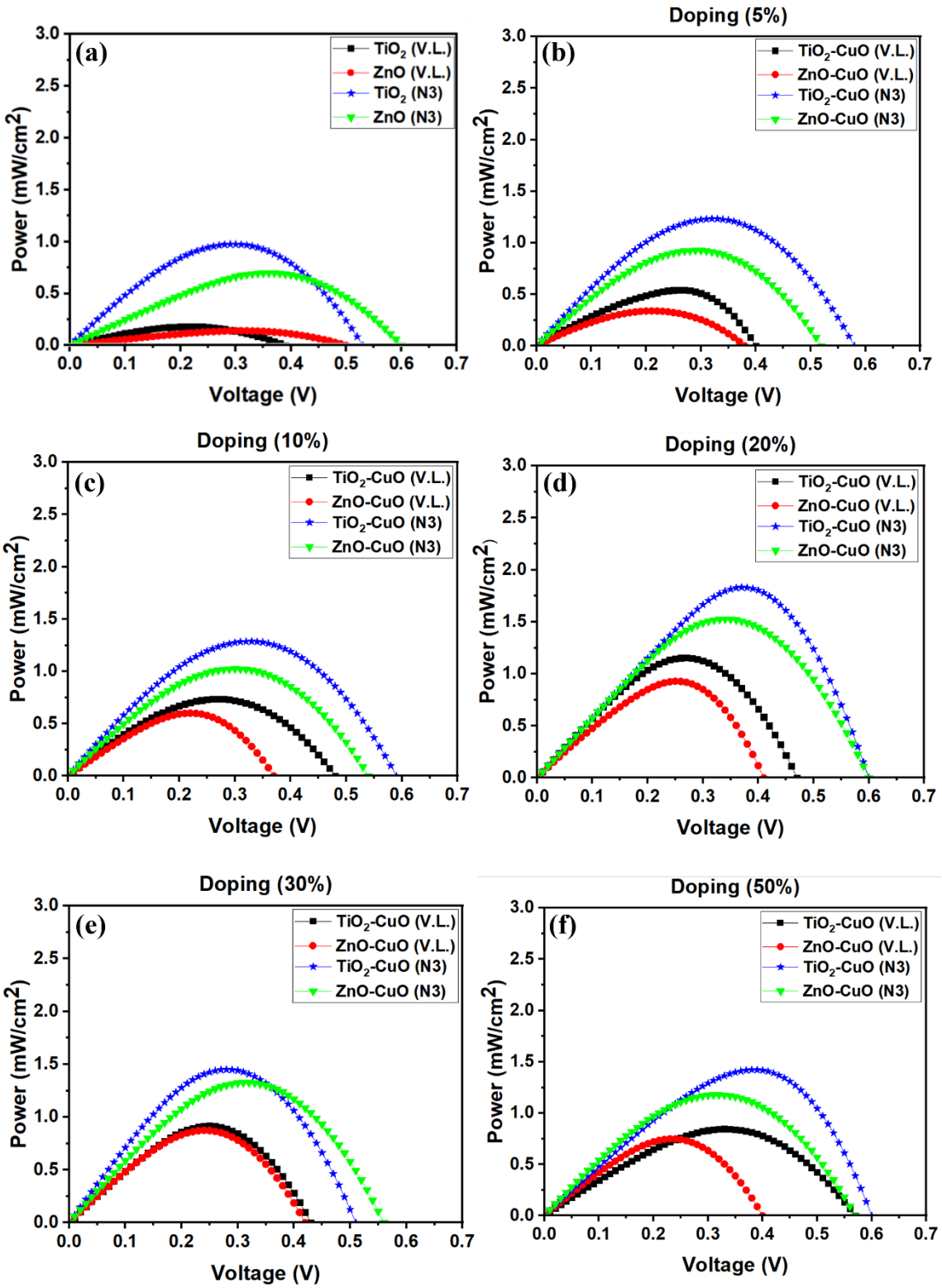


Figure 60 – P-V curves of CuO doping in TiO_2 and ZnO: (a) no doping, (b) 5%, (c) 10%, (d) 20%, (e) 30%, and (f) 50% [38].

The P-V curve figure clearly shows that the progressive incorporation of CuO simultaneously modifies the magnitude of the maximum power and the useful operating voltage range of TiO_2 and ZnO-based photoanodes, for both the V.L. dye and N3. In general terms, it is observed that doping promotes a systematic increase in Pmax from the undoped condition up to 20% CuO, a condition in which the best overall performance of the devices is achieved. From 30% and, more clearly, at 50%, the curves begin to indicate a saturation regime, with a reduction in maximum power and, in some cases, a narrowing of the operating region, suggesting that the excess CuO ceases to act only as a charge separation promoter and begins to introduce deleterious effects, such as increased recombination, partial blockage of electronic transport, and the formation of sites less favorable to charge injection/collection [28,41].

In the undoped condition, Fig. 60 (a), the worst performing system is ZnO (V.L.), whose red curve shows a maximum power (Pmax) of approximately 0.12 mW/cm^2 at around 0.24–0.26 V, with power cancellation around 0.49–0.50 V. Undoped TiO_2 (V.L.), in turn, shows only slightly superior behavior in terms of maximum power, with a maximum power (Pmax) of about 0.14–0.16 mW/cm^2 at approximately 0.21–0.23 V, but with the curve extinction at a lower voltage, close to 0.35–0.36 V, indicating a significant limitation of the operating window. When the N3 dye is analyzed, the response is substantially superior. ZnO (N3) exhibits a maximum power (Pmax) of around 0.68–0.70 mW/cm^2, at approximately 0.36–0.38 V, with zero power near 0.60–0.61 V. TiO_2 (N3), on the other hand, shows the best curve of the undoped system, with a maximum power (Pmax) of approximately 0.96–0.98 mW/cm^2 at 0.30–0.32 V, decaying around 0.52–0.53 V. Therefore, in the undoped system, the hierarchy is clearly TiO_2 (N3) > ZnO (N3) >> TiO_2 (V.L.) ≳ ZnO (V.L.), which already shows that the N3 dye confers a much higher photovoltaic response than V.L., regardless of the semiconductor.

With 5% CuO, Fig. 61 (b), an unequivocal gain is already observed in all systems. TiO_2-CuO raises its Pmax to approximately 0.53–0.55 mW/cm^2 at around 0.25–0.27 V, with power extinction around 0.40–0.41 V. Compared to TiO_2 doped with V.L., this represents an increase of approximately 250–290% in maximum power. ZnO-CuO (V.L.) also improves significantly, reaching approximately 0.33–0.35 mW/cm^2 at 0.20–0.22 V, with zero power around 0.35–0.36 V. In this case, the gain compared to

undoped ZnO is approximately 175–190%. For the N3 dye, TiO_2-CuO (N3) achieves approximately 1.20–1.23 mW/cm^2 at 0.31–0.33 V, with the curve ending at approximately 0.57–0.58 V, while ZnO-CuO (N3) reaches approximately 0.91–0.93 mW/cm^2 at 0.29–0.31 V, with extinction at 0.52–0.53 V. In relative terms, the gain is approximately ~25–27% for TiO_2 (N3) and ~33–37% for ZnO (N3). Thus, even at low doping levels, CuO already positively affects the extracted power and, in particular, enhances the robustness of the ZnO response, which becomes closer to the behavior of TiO_2.

Under the 10% CuO condition, Fig. 60 (c), the improvement trend continues. TiO_2-CuO (V.L.) reaches Pmax around 0.72–0.75 mW/cm^2, at approximately 0.27–0.29 V, with power extinction around 0.47–0.48 V. Compared to the undoped sample, this corresponds to a significant increase, which already demonstrates an important reconfiguration of the photovoltaic response of TiO_2 with V.L. ZnO-CuO (V.L.) reaches about 0.57–0.59 mW/cm^2 at 0.21–0.23 V, with extinction around 0.37–0.38 V, which also represents a significant gain compared to undoped ZnO with the same dye. In the case of N3, TiO_2-CuO (N3) exhibits a maximum power (Pmax) of approximately 1.27–1.30 mW/cm^2 at 0.32–0.34 V, with power tending to zero at 0.56–0.57 V, while ZnO-CuO (N3) reaches about 1.00–1.02 mW/cm^2 at 0.29–0.31 V, becoming zero around 0.53–0.54 V. In other words, a 10% doping further amplifies the gain obtained at 5%, but the difference between 5% and 10% is more moderate in the case of N3, suggesting that, for this dye, the heterostructure was already functional at low levels and begins to evolve incrementally.

The most favorable behavior of the entire series appears at 20% CuO, Fig. 60 (d), which is, in fact, the optimum point of the experimental setup. Under this condition, TiO_2-CuO (V.L.) exhibits a maximum power (Pmax) of approximately 1.13–1.16 mW/cm^2 at 0.26–0.28 V, with zero power at approximately 0.47–0.48 V. Compared to the undoped sample, the gain is considerable, revealing an extremely significant effect of doping. ZnO-CuO (V.L.), in turn, reaches approximately 0.90–0.93 mW/cm^2 at 0.25–0.27 V, with extinction around 0.40–0.41 V, corresponding to a significant increase compared to undoped ZnO. For the N3 dye, TiO_2-CuO (N3) registers the highest power in the entire figure, with a Pmax of approximately 1.80–1.83 mW/cm^2 at 0.36–0.38 V, and power tending to zero around 0.59–0.60 V. ZnO-CuO (N3) reaches approximately

1.50–1.53 mW/cm^2 at 0.33–0.35 V, also with extinction near 0.59–0.60 V. This result is central to the discussion, where at 20%, CuO seems to establish the best compromise between heterojunction formation, improved charge separation, possible amplification of absorption in the visible spectrum, and maintenance of efficient electron transport pathways.

When the doping increases to 30%, Fig. 60 (e), the beginning of the saturation process becomes evident. TiO_2-CuO (V.L.) decays to a Pmax of approximately 0.88–0.91 mW/cm^2 at 0.24–0.25 V, with extinction around 0.42–0.43 V. Compared to the maximum obtained at 20%, this represents a reduction of approximately 20–23%. ZnO-CuO (V.L.) shows approximately 0.85–0.88 mW/cm^2 at 0.23–0.25 V, with power cancellation around 0.40–0.41 V. In this case, the drop compared to 20% is small, on the order of 4–8%, suggesting that ZnO with V.L. It better supports this increase in CuO content than TiO_2 with the same dye. For N3, TiO_2-CuO (N3) drops to approximately 1.42–1.45 mW/cm^2 at 0.28–0.30 V, with extinction at around 0.50–0.51 V, representing a reduction of ~20–22% compared to the 20% peak. ZnO-CuO (N3) decreases to approximately 1.28–1.32 mW/cm^2 at 0.32–0.34 V, with zero power around 0.55–0.56 V, corresponding to a drop of ~13–16%. Therefore, at 30%, although the devices remain superior to the undoped samples, the same electron transfer efficiency obtained at 20% is no longer observed, indicating that the excess CuO begins to compromise the functional architecture of the photoanode.

Under the 50% CuO condition, Fig. 60 (f), saturation becomes even clearer. TiO_2-CuO (V.L.) exhibits a Pmax of approximately 0.82–0.85 mW/cm^2 at 0.32–0.34 V, with the curve ending at 0.55–0.56 V. Although still significantly exceeding undoped TiO_2, this value remains below that observed at 20% and also slightly below that at 30%, indicating a further loss of performance. ZnO-CuO (V.L.) reaches approximately 0.72–0.75 mW/cm^2 at 0.23–0.25 V, with extinction around 0.40–0.41 V, also lower than the maximum at 20% and the value at 30%. For the N3 dye, TiO_2-CuO (N3) exhibits a maximum power (Pmax) of approximately 1.40–1.43 mW/cm^2 at 0.38–0.40 V, with zero power around 0.59–0.60 V, while ZnO-CuO (N3) reaches approximately 1.14–1.17 mW/cm^2 at 0.31–0.33 V, with extinction near 0.55–0.56 V. Regarding 20% reduction, the decreases are on the order of ~21–23% for TiO_2 (N3) and ~23–25% for ZnO (N3). These results show that increasing the CuO fraction to 50% not only fails to provide

additional benefits, but also begins to penalize the system's response, consistent with a scenario in which the dopant ceases to act as a favorable electronic modifier and begins to impose transport barriers and/or recombination centers.

When each system is tracked individually throughout the entire doping series, the pattern becomes even more robust. For TiO_2 with V.L., the Pmax evolves from approximately 0.15 (0%) to 0.54 (5%), 0.74 (10%), and 1.15 mW/cm^2 (20%), then falling to 0.90 (30%) and 0.84 mW/cm^2 (50%). For ZnO with V.L., the sequence is approximately 0.12, 0.34, 0.58, 0.92, 0.87, and 0.74 mW/cm^2. For TiO_2 with N3, the values evolve from about 0.97 to 1.22, 1.29, 1.82, 1.44, and 1.42 mW/cm^2. Finally, for ZnO with N3, an approximate progression of 0.69, 0.92, 1.01, 1.52, 1.31, and 1.16 mW/cm^2 is observed. In all series, therefore, the maximum performance unequivocally occurs at 20% CuO, followed by a decrease at 30% and 50%, characterizing the aforementioned saturation.

Another relevant aspect is the comparison between the two semiconductors. In virtually all conditions, TiO_2 outperforms ZnO when both are sensitized with the same dye, especially with N3, where TiO_2 is superiority is consistent across all doping levels. This suggests that the TiO_2/CuO interface more strongly favors charge separation and transport than the ZnO/CuO interface, possibly due to more favorable band alignment, greater interfacial stability, and better compatibility with dye anchoring and electron injection. However, ZnO also responds positively to doping up to 20%, demonstrating that the beneficial effect of CuO is not exclusive to TiO_2, but is more pronounced in the latter. Furthermore, the fact that ZnO exhibits very high relative gains, especially in V.L. and in N3 up to 20%, shows that it significantly benefits from heterostructure formation, even though it starts from a less efficient initial state.

From a physical standpoint, the observed behavior can be interpreted as a competition between two regimes. Up to 20% CuO, the beneficial effects prevail: formation of local p-n heterojunctions, better electron-hole pair separation, reduction of interfacial recombination, and probable amplification of the optical response in the visible region, which translates into higher and wider P-V curves. Above this content, especially at 30% and 50%, the excess CuO likely begins to excessively coat the active surface, reducing the effectiveness of percolation paths in the host semiconductor and creating regions of recombination or electronic discontinuity, reducing the maximum

extractable power. In device terms, this means that there is an optimal CuO content beyond which morphological and electronic modification ceases to be constructive and becomes limiting.

Thus, the detailed comparative analysis of the P-V curves confirms that doping with CuO promotes a progressive and substantial improvement in the photovoltaic performance of TiO_2 and ZnO-based systems up to 20%, a condition in which the highest maximum power values and the most favorable curves are obtained. From 30% and 50%, saturation of the beneficial effect is observed, with a reduction in Pmax values, which supports the conclusion that 20% CuO constitutes the optimal composition among all the samples analyzed.

4.9 Photovoltaic Parameters (Jsc, FF, Voc, η)

Comparative analysis of the parameters Jsc, Voc, FF, and η as a function of dopant content allows for the identification of photovoltaic performance optimization trends, as well as an understanding of the structural and electronic limits associated with over-doping. Typically, an optimal CuO concentration is expected (frequently observed at intermediate levels around 20%) where photovoltaic parameters are maximized, followed by a possible degradation of performance at higher concentrations (30% and 50%), attributed to saturation effects, the formation of recombinant centers, and impaired electronic connectivity of the semiconductor matrix [28,38,42].

The bar graphs presented in Figures 61 and 62 provide a clear and quantitative visualization of the influence of CuO doping on the photovoltaic performance of TiO_2 and ZnO systems, allowing for an in-depth discussion of the physical mechanisms responsible for the observed variations and contributing to the optimization of materials applied in DSSCs.

Based on the results, it was observed that there was a gradual increase in power, evaluating the DSSCs with CuO dopant increasing from up to 5% to 20%, while between 30% and 50%, the power began to decline due to saturation of the CuO dopant. In Figure 61 (d), the best results for the N3 photosensitizer in the TiO_2-CuO (1.83 mW/cm^2) and ZnO-CuO (1.52 mW/cm^2) combinations are highlighted. It is worth

noting that, being a natural dye, the *Vitis labrusca* photosensitizer in the TiO_2-CuO combination showed good photovoltaic conversion efficiency, resulting in 1.15 %.

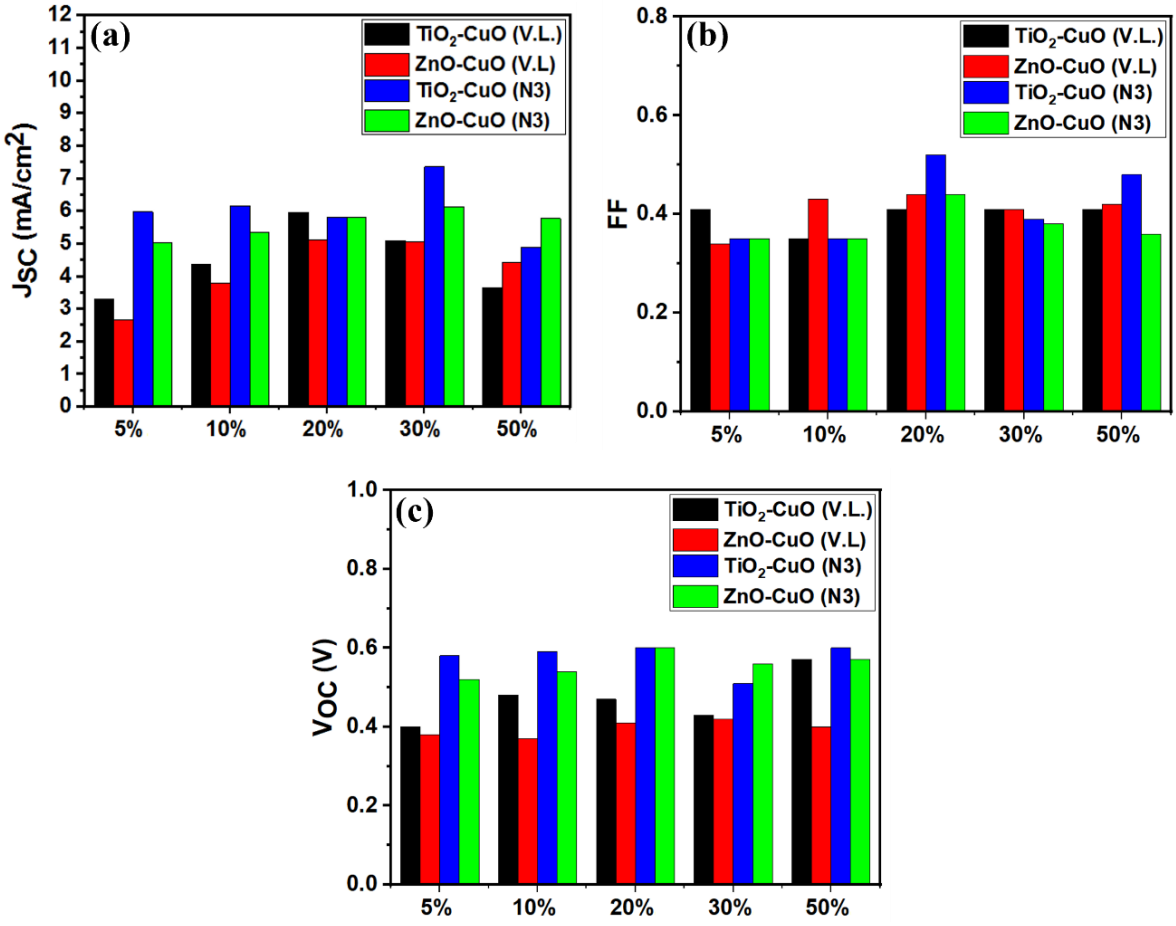


Figure 61 – Photovoltaic parameters: (a) J_{SC}, (b) FF and (c) V_{OC}.

With *Vitis labrusca*, doping with CuO to 20% in TiO_2 improves J_{SC} (5.96 mA/cm²) and FF (0.41), which are the maximum values among the combinations. For ZnO, the best current density also occurs with 20% CuO (J_{SC} = 5.12 mA/cm²), but the highest FF is at 50% CuO (0.42). For the N3 dye, the highest current density occurs with 30% CuO in TiO_2 (J_{SC} = 7.35 mA/cm²), while in ZnO the best performance is with 50% (J_{SC} = 5.77 mA/cm² and V_{OC} = 0.57 V). Figure 62 shows a comparison of the solar conversion efficiencies of each DSSC.

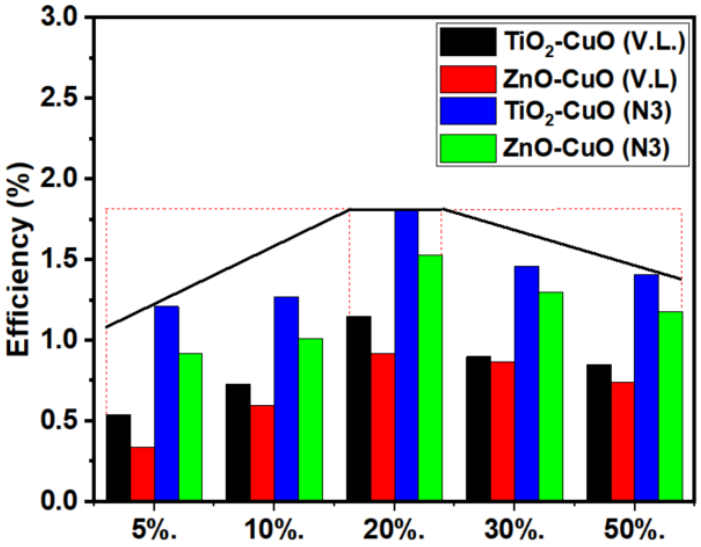


Figure 62 – Solar conversion efficiencies.

With V.L., a 20% CuO concentration led to the highest η for both anodes: 1.15% (TiO_2) and 0.90% (ZnO). Higher concentrations (30% and 50%) resulted in decreased efficiency, indicating a possible saturation/unfavorable effect. Regarding N3, the maximum efficiency value was observed with 20% CuO in TiO_2 (η = 1.80%), which was approximately 24% higher than that observed with 30% (η = 1.45%). Anodes with ZnO also showed a similar trend, but with a lower η, reaching 1.50% with 20% CuO. TiO_2 consistently demonstrated higher efficiency compared to ZnO, regardless of the dye or CuO concentration. For the N3 dye and CuO at 20%, η with TiO_2 (1.80%) was approximately 20% higher than ZnO (1.50%). Similarly, for Vitis labrusca, the performance with TiO_2 (1.15%) was approximately 27.8% higher than ZnO (0.92%). Table 6 presents a comparison of the parameters of the DSSCs developed in this work with some from the literature.

Table 6 - Comparison of the electrical parameters obtained in this work, shown in reference [38], with the values obtained from the literature.

Dye	**Anode**	J_{SC} **(mA/cm²)**	V_{OC} **(V)**	***FF***	η **(%)**	**Ref.**
Physalis peruviana	TiO_2	0.34	0.39	0.43	0.06	[68]
Lantana repens	TiO_2	0.45	0.69	0.34	0.12	[30]
Gerbera	TiO_2	1.22	0.59	0.53	0.38	[80]
Leucanthemum	TiO_2	0.42	0.54	0.27	0.05	[29]
Alpinia purpurata	TiO_2	0.49	0.53	0.40	0.10	[75]
Chrysanthemum	TiO_2	0.34	0.47	0.48	0.08	[73]
Malus domestica	TiO_2	0.62	0.52	0.49	0.16	[44]
Boranil	TiO_2	0.96	0.60	0.39	0.22	[71]
Beta vulgaris	TiO_2	1.13	0.04	0.77	0.03	[81]
Beta vulgaris	TiO_2-CuO (10%)	1.17	0.06	0.77	0.05	[81]
Beta vulgaris	TiO_2-CuO (20%)	1.18	0.07	0.77	0.06	[81]
Beta vulgaris	TiO_2-CuO (30%)	0.38	0.01	0.52	0.002	[81]
Vitis labrusca	TiO_2	1.23	0.39	0.37	0.18	this work [38]
Vitis labrusca	ZnO	0.59	0.50	0.47	0.14	this work [38]
Vitis labrusca	TiO_2-CuO (5%)	3.30	0.40	0.41	0.54	this work [38]
Vitis labrusca	ZnO-CuO (5%)	2.65	0.38	0.34	0.34	this work [38]
Vitis labrusca	TiO_2-CuO (10%)	4.36	0.48	0.35	0.73	this work [38]
Vitis labrusca	ZnO-CuO (10%)	3.79	0.37	0.43	0.60	this work [38]
Vitis labrusca	TiO_2-CuO (20%)	5.96	0.47	0.41	1.15	this work [38]
Vitis labrusca	ZnO-CuO (20%)	5.12	0.41	0.44	0.92	this work [38]
Vitis labrusca	TiO_2-CuO (30%)	5.09	0.43	0.41	0.90	this work [38]
Vitis labrusca	ZnO-CuO (30%)	5.05	0.42	0.41	0.87	this work [38]
Vitis labrusca	TiO_2-CuO (50%)	3.64	0.57	0.41	0.85	this work [38]
Vitis labrusca	ZnO-CuO (50%)	4.42	0.40	0.42	0.74	this work [38]
N3	ZnO-CuO (1%)	1.67	0.96	0.71	1.15	[82]
N3	ZnO-CuO (3%)	1.80	1.09	0.69	1.34	[82]
N3	ZnO-CuO (5%)	1.60	0.99	0.69	1.09	[82]
N3	TiO_2	5.19	0.53	0.35	0.85	this work [38]
N3	ZnO	2.49	0.60	0.47	0.70	this work [38]
N3	TiO_2-CuO (5%)	5.97	0.58	0.35	1.21	this work [38]
N3	ZnO-CuO (5%)	5.03	0.52	0.35	0.92	this work [38]
N3	TiO_2-CuO (10%)	6.15	0.59	0.35	1.27	this work [38]
N3	ZnO-CuO (10%)	5.34	0.54	0.35	1.01	this work [38]
N3	TiO_2-CuO (20%)	5.81	0.60	0.52	1.81	this work [38]
N3	ZnO-CuO (20%)	5.79	0.60	0.44	1.53	this work [38]
N3	TiO_2-CuO (30%)	7.35	0.51	0.39	1.46	this work [38]
N3	ZnO-CuO (30%)	6.13	0.56	0.38	1.30	this work [38]
N3	TiO_2-CuO (50%)	4.89	0.60	0.48	1.41	this work [38]
N3	ZnO-CuO (50%)	5.77	0.57	0.36	1.18	this work [38]

The comparison of photovoltaic performance clearly demonstrates the superiority of this work in relation to the literature references, especially in the optimized doping regime with CuO. While previous studies with natural dyes based on TiO_2 typically show low efficiencies, ranging from 0.03% to 0.38% (such as *Gerbera* with 0.38% or Boranil with 0.22%), the results obtained in this work for *Vitis labrusca* demonstrate substantial gains even at low doping concentrations: with 5% CuO, the efficiency reaches 0.54% (TiO_2), representing an increase of approximately 200% compared to the undoped system (0.18%), while at 10% this gain rises to about 305% (0.73%). The optimum point is observed at 20% CuO, where maximum efficiency reaches 1.15% (TiO_2) and 0.92% (ZnO), far exceeding the values reported for natural dyes in the literature and even equivalent doped systems (such as *Beta vulgaris*, with only 0.06% in 20% CuO). A similar trend is observed for the standard dye N3, in which efficiency increases from 0.85% (pure TiO_2) to 1.21% (5%), 1.27% (10%) and reaches 1.81% at 20%, consolidating this point as the optimum condition. However, for higher concentrations (30% and 50%), a clear trend towards saturation/decline is observed: for Vitis labrusca, efficiency decreases from 1.15% (20%) to 0.90% (30%) and 0.85% (50%), while for N3 it reduces from 1.81% to 1.46% (30%), showing that excess CuO compromises performance, possibly due to the formation of recombination centers and blockage of electronic transport. Thus, quantitatively, the present work not only surpasses the literature in absolute efficiency in the optimal regime, but also consistently demonstrates the typical behavior of increase (5–20%) followed by saturation (≥30%), reinforcing the robustness and relevance of the results obtained. As a final step in the characterizations, the next subsection presents the impedances of each of the DSSCs using the electrochemical impedance spectroscopy (EIS) technique.

4.10 Impedance of DSSCs (EIS)

Electrochemical impedance spectroscopy (EIS) is one of the most robust tools for investigating charge transport and recombination processes in photovoltaic devices, especially in DSSCs. By applying a small-signal sinusoidal perturbation over a wide frequency range, this technique allows the decomposition of resistive and capacitive contributions associated with different device interfaces, such as the

electrode/semiconductor contact, the semiconductor/dye/electrolyte interface, and diffusive processes in the electrolyte [83]. Thus, the analysis of impedance curves is typically represented by Nyquist diagrams, enabling a deeper understanding of the mechanisms governing photovoltaic performance [84].

Figure 63 shows the electrochemical impedance results obtained from all DSSCs. The graphs provided present Nyquist diagrams for different material configurations and experimental conditions. Each graph reflects the impedance response of an electrochemical system, composed of one or more semicircular arcs and, in some cases, a linear slope at lower frequencies [85-87]. The detailed comparison focuses on qualitative and quantitative aspects, highlighting the differences in electrochemical behavior between the analyzed systems.

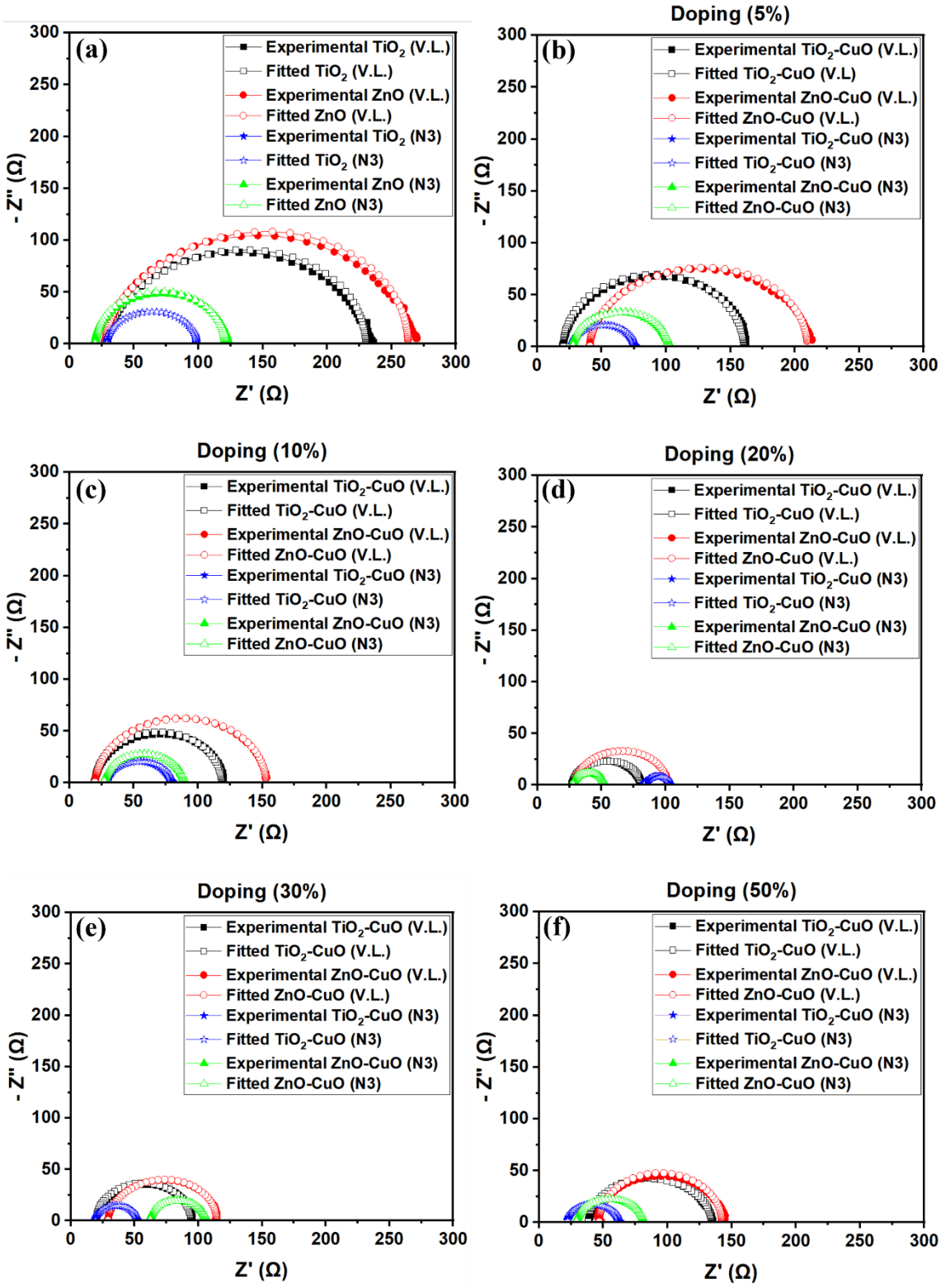


Figure 63 – EIS curves of CuO doping in TiO_2 and ZnO: (a) no doping, (b) 5%, (c) 10%, (d) 20%, (e) 30%, and (f) 50% [38].

The size of the semicircular arc is directly related to the charge transfer resistance (Rct) [88,89]. In the graphs with TiO_2 as the base material, the semicircular arcs are significantly smaller compared to those of ZnO, indicating a lower resistance to charge transport in TiO_2-based systems. The addition of CuO to the composites resulted in a noticeable decrease in the size of the semicircular arcs, especially in the samples with 20% CuO. This reduction reflects a more efficient electrochemical interface for electron transport [90-93].

At high frequencies, the intersection of the graphs with the real axis represents the series resistance (Rs) [91]. Rs remained approximately constant between the different configurations, indicating that the observed variations are predominantly related to the interfaces and not to the intrinsic resistance of the materials. The linear slope observed at lower frequencies reflects the Warburg diffusion impedance (Wd), associated with the limited diffusion of ions or electrons [92,93]. The graphs of the systems with 50% CuO showed steeper slopes, suggesting greater difficulty in charge transport compared to lower CuO concentrations (such as 20%).

The graphs with the N3 dye show smaller semicircular arcs than those of *Vitis labrusca*. This indicates that the N3 dye facilitates charge transfer, possibly due to a higher electron collection efficiency at the photoactive interface. The difference is particularly evident in the combinations with 20% CuO, where the semicircular arcs associated with the N3 dye are about 30% smaller than those of *Vitis labrusca*.

Comparative analysis of Nyquist plots reveals significant differences in the electrochemical behavior of the different configurations. Systems based on TiO_2 and the N3 dye demonstrated greater efficiency in charge transport, evidenced by smaller semicircular arc sizes and lower Rct values. The ideal CuO concentration was identified as 20%, where improvements in electron transport are most pronounced. In contrast, higher CuO concentrations (50%) introduced diffusion limitations, as evidenced by the steep linear slope at low frequencies.

The results demonstrate that the electrochemical impedance characterizations are consistent with the previous results obtained in the optical, structural, morphological, and electrochemical characterizations of each electrode and dye. To increase the reliability of the measurements, the modeling of each DSSC was performed using IviumSoft software, demonstrating the smallest possible error between the experimental

and the measured values, as shown in Table 7, and the corresponding equivalent circuit is shown in Figure 64.

Table 7 - Values of each element of the equivalent circuit with their associated errors.

Dye/Anode	R_S (Ω)	R_1 (Ω)	R_2 (Ω)	R_3 (Ω)	C_1 (μF)	C_2 (μF)	C_3 (μF)
V.L.: TiO_2	29.62 ± 0.51	160.8 ± 3.06	39.51 ± 12.72	1.532 ± 7.82	11.43 ± 5.92	12.75 ± 5.93	60.61 ± 7.49
V.L.: ZnO	28.01 ± 0.52	200.7 ± 2.22	34.22 ± 13.40	2.159 ± 9.53	14.92 ± 4.65	21.28 ± 5.98	76.17 ± 9.01
V.L.: TiO_2-CuO (5%)	20.21 ± 0.61	139.9 ± 0.71	37.16 ± 10.12	2.486 ± 7.93	33.89 ± 0.94	42.37 ± 4.69	90.48 ± 7.63
V.L.: ZnO-CuO (5%)	41.07 ± 0.26	125.1 ± 3.98	43.52 ± 11.75	1.468 ± 5.25	49.70 ± 7.09	45.83 ± 5.93	116.2 ± 8.32
V.L.: TiO_2-CuO (10%)	19.87 ± 0.54	98.51 ± 0.63	32.47 ± 12.08	1.259 ± 7.64	35.92 ± 0.93	53.74 ± 8.47	120.9 ± 92
V.L.: ZnO-CuO (10%)	19.76 ± 0.18	97.53 ± 5.80	34.15 ± 16.52	1.459 ± 9.08	58.21 ± 8.60	73.18 ± 9.80	134.4 ± 7.27
V.L.: TiO_2-CuO (20%)	27.28 ± 0.37	28.77 ± 11.09	24.69 ± 13.02	1.239 ± 5.81	48.31 ± 18.42	19.30 ± 6.51	62.59 ± 9.23
V.L.: ZnO-CuO (20%)	28.85 ± 0.15	49.82 ± 3.64	21.78 ± 8.22	1.977 ± 7.99	56.03 ± 5.61	50.43 ± 4.25	77.12 ± 11.68
V.L.: TiO_2-CuO (30%)	19.90 ± 0.51	74.18 ± 0.61	8.928 ± 812.45	1.745 ± 8.22	36.06 ± 0.99	80.41 ± 7.35	93.74 ± 41
V.L.: ZnO-CuO (30%)	29.21 ± 0.18	75.55 ± 1.41	9.645 ± 11.25	1.368 ± 7.41	40.75 ± 2.73	84.36 ± 4.88	73.27 ± 94
V.L.: TiO_2-CuO (50%)	38.19 ± 0.16	27.73 ± 10.31	65.89 ± 4.23	2.396 ± 8.26	183.1 ± 16.38 ±	27.71 ± 1.93	70.20 ± 7.15
V.L.: ZnO-CuO (50%)	46.83 ± 0.49	95.52 ± 0.74	35.77 ± 8.65	1.286 ± 5.46	28.81 ± 1.36	19.84 ± 2.75	53.74 ± 7.37
N3: TiO_2	28.88 ± 0.14	41.82 ± 4.71	26.48 ± 7.28	1.199 ± 8.62	66.48 ± 7.16	41.85 ± 3.68	83.09 ± 8.78
N3: ZnO	19.93 ± 0.58	100.9 ± 0.67	25.42 ± 5.62	1.531 ± 5.77	35.12 ± 0.99	36.26 ± 3.42	100.7 ± 6.16
N3: TiO_2-CuO (5%)	27.45 ± 0.37	28.63 ± 10.45	18.88 ± 15.91	1.741 ± 9.12	32.68 ± 17.11	17.37 ± 7.99	127.6 ± 7.76
N3: ZnO-CuO (5%)	27.82 ± 0.32	49.69 ± 6.88	24.24 ± 14.25	2.237 ± 6.42	36.65 ± 11.49	26.09 ± 7.34	98.36 ± 68
N3: TiO_2-CuO (10%)	29.73 ± 0.35	26.27 ± 8.14	22.73 ± 9.49	1.492 ± 8.28	71.66 ± 14.49	24.23 ± 4.20	50.47 ± 9.74
N3: ZnO-CuO (10%)	26.83 ± 0.28	10.66 ± 10.81	49.79 ± 2.18	2.221 ± 7.82	273.7 ± 19.59	15.19 ± 1.00	32.23 ± 8.62
N3: TiO_2-CuO (20%)	83.32 ± 0.10	16.57 ± 1.45	3.263 ± 7.22	1.372 ± 8.56	121.6 ± 3.31	78.74 ± 7.26	80.39 ± 47.63
N3: ZnO-CuO (20%)	27.83 ± 0.38	23.75 ± 0.78	7.527 ± 10.25	1.157 ± 9.64	44.46 ± 1.86	82.72 ± 6.93	50.47 ± 34
N3: TiO_2-CuO (30%)	19.33 ± 0.30	28.39 ± 2.32	3.771 ± 17.55	1.996 ± 6.42	55.65 ± 4.57	99.90 ± 7.25	62.36 ± 48
N3: ZnO-CuO (30%)	62.32 ± 0.14	12.91 ± 16.67	30.78 ± 7.03	1.729 ± 8.39	198.1 ± 27.60	27.49 ± 3.27	86.47 ± 34
N3: TiO_2-CuO (50%)	22.39 ± 0.35	15.34 ± 15.71	24.14 ± 10.02	1.825 ± 9.35	67.21 ± 25.68	14.92 ± 5.04	79.26 ± 9.02
N3: ZnO-CuO (50%)	29.09 ± 0.15	19.42 ± 7.09	30.78 ± 4.09	1.958 ± 10.58	123.7 ± 11.26	26.59 ± 1.70	60.15 ± 5.91

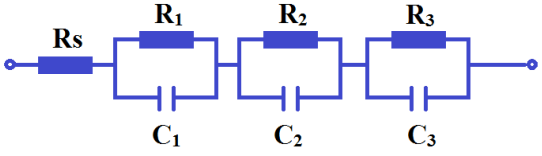


Figure 64 – Corresponding equivalent circuit [38].

Figure 64 shows the equivalent circuit adjusted from experimental Electrochemical Impedance Spectroscopy (EIS) data obtained using IviumSoft software associated with the IVIUM CompactStat multi-potentiostat. This circuit represents an electrical model of the dynamic behavior of the DSSC, allowing correlation of the device's internal physicochemical processes with ideal electrical elements [90].

The circuit consists of an initial series resistor R_s, followed by three parallel resistor-capacitor branches (R_1C_1, R_2C_2, and R_3C_3) connected in series with each other. Each of these elements is associated with different electrochemical processes that occur at distinct interfaces and timescales within the cell [89-93].

The (Rs) series resistance represents the ohmic losses of the system, including the resistance of the conductive substrate (FTO), the electrolyte resistance, and the contributions of the electrical contacts. This parameter is directly obtained from the high-frequency intercept in the Nyquist diagram and is independent of interfacial processes [91].

The first parallel branch, composed of R_1 and C_1, is generally associated with high-frequency processes related to the counter electrode/electrolyte interface [85-89]. The resistance R_1 describes the charge transfer at this interface, while C_1 represents the capacitance of the electrical double layer formed on the surface of the counter electrode. The associated capacitive impedance is given by Eq. (3.28).

The second branch, formed by R2 and C2, is related to the dominant processes at the photoanode/dye/electrolyte interface, often being the most relevant for DSSC performance [91]. The resistance R2 is associated with electronic recombination and charge transfer between the semiconductor (TiO_2 or ZnO doped with CuO) and the electrolyte. C2, on the other hand, is related to the chemical capacitance of the semiconductor, reflecting the density of available electronic states and charge storage in the material [87,89].

The third branch, consisting of R_3 and C_3, is associated with low-frequency processes, generally related to the diffusion of redox species in the electrolyte and mass transport within the cell. In many cases, this behavior can also be described by a Warburg element; however, its approximation by an RC circuit allows for a simplified and efficient modeling of experimental data [90-93].

The series association of these three RC branches reflects the distributed nature of electrochemical processes in the DSSC, where each interface contributes a characteristic time constant. These time constants τ can be expressed as [85-90]:

$$\tau = R \times C \tag{4.3}$$

Being fundamental for describing the system's response across different frequency ranges. IviumSoft performs the fitting of experimental data to the equivalent circuit using non-linear regression algorithms, providing the values of each element (Rs, Ri, Ci) along with their respective associated errors [90-93]. These errors represent the uncertainty of the fit and indicate the quality of the modeling employed. Low error values suggest good agreement between the proposed electrical model and the experimental data obtained [91,92].

Thus, the equivalent circuit shown in Figure 64 allows for a quantitative interpretation of the internal processes of the DSSC, making it possible to identify limitations related to charge transfer resistance, electronic recombination, and diffusion of species in the electrolyte. This approach is essential for understanding the impact of structural modifications, such as doping with copper oxide (CuO), on the electrochemical and photovoltaic performance of the device [28].

For better understanding, Figure 65 shows the physical-electrochemical representation associated with the equivalent circuit.

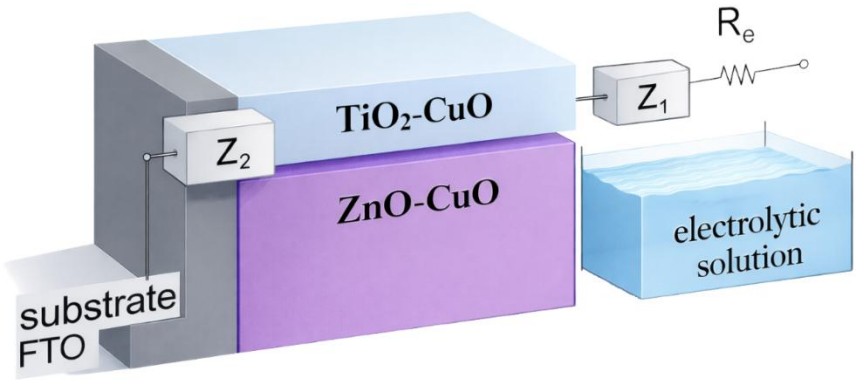


Figure 65 – Series model of the DSSC circuits associated with the impedances.

The Figure 65 presents a physical-electrochemical representation of the DSSC correlated to the impedance elements identified by EIS, establishing a link between the device structure and its equivalent circuit [72]. The conductive substrate FTO is associated with impedance Z_2, mainly representing ohmic and electrical contact contributions, while the TiO_2-CuO and ZnO-CuO semiconductor layers correspond to the active region of charge transport and storage, where electronic conduction processes and possible recombinations occur [85-89]. The interface between the semiconductor and the electrolytic solution is modeled by impedance Z_1, related to charge transfer and interfacial capacitance, whose response depends on the frequency as shown in Eq. 3.28.

Finally, the electrolyte is represented by the resistance Re, associated with the ionic conduction of the redox pair. Thus, the figure summarizes the spatial distribution of the electrochemical processes along the device (L-axis), showing that each region contributes differently to the total impedance of the DSSC, in agreement with the results obtained by electrochemical impedance spectroscopy [90,92]. Consequently, Figure 66 shows the Randles circuit, which includes the Warburg impedance (Zw), in addition to the processes already described.

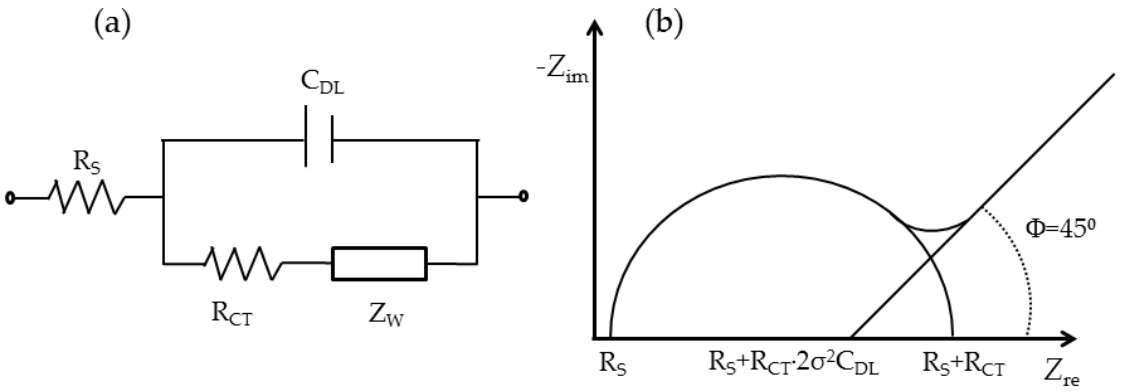


Figure 66 – (a) Randles circuit and (b) Randles frequency response for the Nyquist diagram. Adapted from: [99].

Figure 66 (a) shows the Randles equivalent circuit, widely used to describe electrochemical systems analyzed by electrochemical impedance spectroscopy (EIS). In this model, the series resistor RS represents the ohmic resistance of the electrolytic solution, the electrical contacts, and the substrate, and is independent of Frequency [85,87]. In parallel, the double-layer capacitor CDL is observed, associated with the

accumulation of charges at the electrode/electrolyte interface, reflecting the charge storage capacity in this interfacial region. In series with the diffusional element is the charge transfer resistance RCT, which is directly related to the kinetics of redox reactions at the interface, being one of the main parameters governing the efficiency of devices such as DSSCs [90-93]. The element ZW, known as Warburg impedance, describes the diffusive transport of ionic species in the electrolyte, showing frequency dependence and being more relevant at low frequencies [98,99]. Figure 66 (b) shows the Nyquist diagram response corresponding to this circuit, where the real axis (Zre) represents the resistive component and the negative imaginary axis (Zim) is associated with capacitive processes [92-95]. The initial intercept on the real axis corresponds to RS, while the diameter of the semicircle is directly related to RCT, indicating the charge transfer resistance; the peak of the semicircle occurs at a characteristic frequency defined by $\omega = 1/(RCT.CDL)$ [88,90,100]. At low frequencies, the presence of the inclined line, approximately at 45 degrees, characterizes the contribution of the Warburg impedance, highlighting diffusional limitations in the system [92-95]. Thus, the joint analysis of these elements allows correlating electrical, kinetic, and diffusional properties of the device, being fundamental for the interpretation of the electrochemical performance in DSSCs.

5 Conclusion and Future Work

5.1 Final Considerations

This thesis demonstrates that CuO doping in TiO_2 and ZnO is an effective strategy to enhance the performance of Dye-Sensitized Solar Cells (DSSCs). The combination of structural, optical, morphological, and electrochemical analyses enabled a consistent correlation between material modification and photovoltaic behavior.

FTIR results confirmed that CuO incorporation does not disrupt the fundamental chemical structure of the semiconductors or the dye molecules, preserving key vibrational modes (Ti–O, Zn–O, and organic functional groups). The appearance of Cu–O-related bands supports the successful incorporation of the dopant without inducing detrimental chemical transformations.

UV–Vis spectroscopy revealed a red shift in the absorption edge, indicating enhanced light harvesting in the visible region. This behavior is associated with the introduction of intermediate electronic states by CuO, which effectively reduces the bandgap and increases photon absorption.

XRD analysis showed that CuO incorporation leads to slight lattice distortions and reduced crystallinity in TiO_2, which favors dye adsorption. In ZnO, higher doping levels resulted in the formation of secondary phases, indicating a saturation limit. These results were supported by XRF, confirming homogeneous dopant distribution up to ~20%.

Morphological analyses (SEM and AFM) demonstrated that CuO doping increases surface roughness and porosity, leading to a larger active surface area. This directly contributes to improved dye loading and interfacial charge transfer.

Photovoltaic measurements (J–V and P–V) showed a consistent increase in short-circuit current density (Jsc) and overall efficiency (η) with doping. The best performance was obtained at ~20% CuO, reaching Jsc ≈ 5.96 $mA \cdot cm^{-2}$ and η ≈ 1.15% for Vitis labrusca-based devices, confirming the beneficial role of controlled doping.

Electrochemical impedance spectroscopy (EIS) revealed reduced charge transfer resistance and improved interfacial properties in doped systems, indicating more efficient electron transport and suppressed recombination processes.

The efficiency trend as a function of dopant concentration follows three distinct regimes: (i) an initial enhancement region (5–10%), (ii) an optimal performance point (~20%), and (iii) a degradation region at higher concentrations due to increased defects and recombination centers. These results indicate that performance gains arise from the combined effects of bandgap tuning, improved dye adsorption, and enhanced charge transport.

This work demonstrates that the integration of CuO as a dopant, combined with natural dyes such as Vitis labrusca, represents a viable and sustainable approach for improving DSSC performance, while maintaining low-cost and environmentally friendly fabrication routes.

5.2 Future Work

Based on the results obtained, several research directions can be proposed:

- Alternative dopants and semiconductors: Investigation of other dopants (e.g., Fe, Ni, N) and semiconductor matrices such as SnO_2 and WO_3 to further optimize electronic structure and charge transport;
- Advanced sensitizers: Development of more stable and efficient natural dyes, as well as hybrid systems combining natural and synthetic sensitizers to improve light absorption and durability;
- Device scaling and real conditions: Fabrication of larger-area DSSCs and evaluation under real environmental conditions, including temperature variation, humidity, and non-uniform illumination;
- Stability and degradation studies: Long-term and accelerated aging tests to identify degradation mechanisms and improve device lifetime;
- Theoretical modeling: Application of computational approaches such as density functional theory (DFT) to better understand the electronic effects of doping and guide experimental optimization.

References

[1] PATA, Ugur Korkut. How to progress towards sustainable development by leveraging renewable energy sources, technological advances, and human capital. Renewable Energy, v. 241, p. 122367, 2025. https://doi.org/10.1016/j.renene.2025.122367

[2] BASEER, Mohammad Abdul; KUMAR, Prashant; NASCIMENTO, Erick Giovani Sperandio. Advancements in hydrogen production through the integration of renewable energy sources with AI techniques: A comprehensive literature review. Applied energy, v. 383, p. 125354, 2025. https://doi.org/10.1016/j.apenergy.2025.125354

[3] ARIDI, Rima et al. Eco-environmental, and social impacts of producing electricity with various renewable energy sources. Energy, v. 320, p. 135139, 2025. https://doi.org/10.1016/j.energy.2025.135139

[4] ABED, Azher M. et al. Power generation by utilization of different renewable energy sources in five Middle Eastern countries: Present status, opportunities and challenges. Sustainable Energy Technologies and Assessments, v. 73, p. 104101, 2025. https://doi.org/10.1016/j.seta.2024.104101

[5] DE FREITAS, Illana Thayná Amaral; ABRAHÃO, Raphael. Study of global solar irradiance in Northeast Brazil with considerations on superirradiance and extreme superirradiance events. Theoretical and Applied Climatology, v. 156, n. 2, p. 107, 2025. https://doi.org/10.1007/s00704-024-05351-5

[6] FURIATI, Ricardo HG et al. Solar radiation times-series forecasting in southern Brazil: A comprehensive analysis. Ecological Informatics, p. 103601, 2026. https://doi.org/10.1016/j.ecoinf.2026.103601

[7] DE LIMA, Francisco Jose Lopes et al. Evaluation of the short and medium-term forecast quality of global solar irradiance from GFS-MOS and WRF-Solar models for the northeast region of Brazil. Energy Reports, v. 13, p. 2187-2203, 2025. https://doi.org/10.1016/j.ecoinf.2026.103601

[8] DADA, Modupeola; POPOOLA, Patricia. Recent advances in solar photovoltaic materials and systems for energy storage applications: a review. Beni-Suef University Journal of Basic and Applied Sciences, v. 12, n. 1, p. 1-15, 2023. https://doi.org/10.1186/s43088-023-00405-5

[9] KANDIL, Abdalrhman A. et al. Adaptation of the solar spectrum to improve the use of sunlight: A critical review on techniques, applications, and current trends. Advanced Sustainable Systems, v. 7, n. 6, p. 2300012, 2023. https://doi.org/10.1002/adsu.202300012

[10] KOPP, Greg. Solar irradiance measurements: G. Kopp. Living Reviews in Solar Physics, v. 22, n. 1, p. 1, 2025. https://doi.org/10.1007/s41116-025-00040-5

[11] ROY, Paramita et al. Effects of climate change and sea-level rise on coastal habitat: Vulnerability assessment, adaptation strategies and policy recommendations. Journal of Environmental Management, v. 330, p. 117187, 2023. https://doi.org/10.1016/j.jenvman.2022.117187

[12] SUBRAMANIAN, Aishwarya et al. Long-term impacts of climate change on coastal and transitional eco-systems in India: an overview of its current status, future projections, solutions, and policies. RSC advances, v. 13, n. 18, p. 12204-12228, 2023. DOI: 10.1039/D2RA07448F

[13] AMANCIO, Moisés do Amaral et al. Enhanced Grätzel Solar Cells Using Carbon Nanodots and Natural Dye. ACS Physical Chemistry Au, v. 5, n. 2, p. 151-161, 2024. https://doi.org/10.1021/acsphyschemau.4c00080

[14] SIGNIFICADOS. Sol. Disponível em: https://www.significados.com.br/sol/. Acesso em: 10 de janeiro de 2026.

[15] SUN, Fanglong et al. Ultraviolet-visible-near-infrared light responsive inorganic/organic S-scheme heterojunctions for efficient H2O2 production. Journal of Materials Science & Technology, v. 229, p. 287-295, 2025. https://doi.org/10.1016/j.jmst.2024.12.060

[16] CARPENTIERI, Maria Antonietta; DOMENICI, Valentina. Introducing UV–visible spectroscopy at high school level following the historical evolution of spectroscopic instruments: a proposal for chemistry teachers. Foundations of Chemistry, v. 26, n. 1, p. 115-139, 2024. https://doi.org/10.1007/s10698-024-09501-5

[17] LABXCHANGE. Disponível em: https://www.labxchange.org/library/items/lb:LabXchange:dde072b9:html:1. Acesso em: 12 de fevereiro de 2026.

[18] RICHARD, Erik et al. Advancements in solar spectral irradiance measurements by the TSIS-1 spectral irradiance monitor and its role for long-term data continuity. Journal of Space Weather and Space Climate, v. 14, p. 10, 2024. https://doi.org/10.1051/swsc/2024008

[19] NASA. Analyzing Cloud Effects on Earth's Energy Budget. Disponível em: https://mynasadata.larc.nasa.gov/mini-lessonactivity/analyzing-cloud-effects-earths-energy-budget. Acesso em: 13 de fevereiro de 2026.

[20] BANKSET ENERGY. Disponível em: https://bankset-energy.com/ . Acesso em: 21 de janeiro de 2026.

[21] INSTITUTO FEDERAL DO CEARÁ (IFCE). Módulo de execução de rede neural MLP para estimativa de irradiância solar global. Disponível em: https://polodeinovacao.ifce.edu.br/vitrine/modulo-de-execucao-de-rede-neural-mlp-para-estimacao-de-irradiancia-solar-global/ . Acesso em: 28 de janeiro de 2026.

[22] GAUTAM, Vaishali; KHATOON, Shahida; JALIL, Mohd Faisal. History of Solar PV System and its Recent Development. Photovoltaic Systems Technology, p. 1-26, 2024. https://doi.org/10.1002/9781394167678.ch1 .

[23] MOTA, N. S.; ALBUQUERQUE, V. F.; OLIVEIRA, R. M. M. ENERGIA SOLAR NA CONSTRUÇÃO CIVIL NOS GERAIS DE BALSAS, MARANHÃO UMA PERSPECTIVA DE SUSTENTABILIDADE: OPORTUNIDADES E DESAFIOS DO USO DA ENERGIA SOLAR EM EDIFICAÇÕES NO CERRADO MARANHENSE. In: OPEN SCIENCE RESEARCH XIX. Editora Científica Digital, 2025. p. 201-224. https://10.37885/250519295 .

[24] CHEN, Rongxin et al. Revealing the mechanism of Faradaic PN junction design strategy in enhancing electrochemical performance of supercapacitor. Chemical Engineering Journal, v. 488, p. 150981, 2024. https://doi.org/10.1016/j.cej.2024.150981

[25] BOYLESTAD, Robert L.; NASHELSKY, Louis. Dispositivos eletrônicos e teoria dos circuitos. 11. ed. São Paulo: Pearson Education do Brasil, 2013.

[26] O'REGAN, Brian; GRÄTZEL, Michael. A low-cost, high-efficiency solar cell based on dye-sensitized colloidal TiO_2 films. nature, v. 353, n. 6346, p. 737-740, 1991. https://doi.org/10.1038/353737a0

[27] NATIONAL LABOR RELATIONS BOARD (NLRB). [Página inicial]. Disponível em: https://www.nlr.gov/index . Acesso em: 19 de fevereiro de 2026.

[28] DA CUNHA, H. O. et al. Improved solar cells efficiency with TiO_2/CuO nanocomposite as photoanode sensitized by natural dyes from scarlet eggplant, pitomba and black grapes. Journal of Materials Science: Materials in Electronics, v. 36, n. 1, p. 35, 2025. https://doi.org/10.1007/s10854-024-14106-x

[29] FERREIRA, F. C. et al. Photoelectric performance evaluation of DSSCs using the dye extracted from different color petals of Leucanthemum vulgare flowers as novel sensitizers. Spectrochimica Acta Part A: Molecular and Biomolecular Spectroscopy, v. 233, p. 118198, 2020. https://doi.org/10.1016/j.saa.2020.118198

[30] FERREIRA, B. C. et al. Performance evaluation of DSSCs using naturally extracted dyes from petals of Lantana repens and Solidago canadensis flowers as light-harvesting units. Ionics, v. 28, n. 11, p. 5233-5242, 2022. https://doi.org/10.1007/s11581-022-04727-9

[31] REN, Yameng et al. Hydroxamic acid pre-adsorption raises the efficiency of cosensitized solar cells. Nature, v. 613, n. 7942, p. 60-65, 2023. https://doi.org/10.1038/s41586-022-05460-z

[32] EDUBILLA. Michael Grätzel. Disponível em: https://edubilla.com/inventor/michael-gratzel/ . Acesso em: 26 de fevereiro de 2026.

[33] KUMAR, P. et al. Solar cell-integrated energy storage devices for electric vehicles: a breakthrough in the green renewable energy. 2022. https://doi.org/10.1007/s11581-022-04700-6

[34] MAALOUF, Amani et al. A comprehensive review on life cycle assessment of commercial and emerging thin-film solar cell systems. Renewable and Sustainable Energy Reviews, v. 186, p. 113652, 2023. https://doi.org/10.1016/j.rser.2023.113652

[35] SCHMID, Martina. Revisiting the definition of solar cell generations. Advanced Optical Materials, v. 11, n. 20, p. 2300697, 2023. https://doi.org/10.1002/adom.202300697

[36] KANT, Neeraj; SINGH, Pushpendra. Review of next generation photovoltaic solar cell technology and comparative materialistic development. Materials Today: Proceedings, v. 56, p. 3460-3470, 2022. https://doi.org/10.1016/j.matpr.2021.11.116

[37] SILVA, Elisangela P. et al. Sustainability in Solar Cells. In: Handbook of Energy Materials. Singapore: Springer Nature Singapore, 2022. p. 1-28. https://doi.org/10.1007/978-981-16-4480-1_33-1

[38] DA CUNHA, Higor Oliveira et al. enhancing the efficiency of solar cells based on TiO_2 and ZnO photoanodes through copper oxide: A comparative study using vitis labrusca extract and N3 ruthenium dye. Colorants, v. 3, n. 4, p. 329-349, 2024. https://doi.org/10.3390/colorants3040023

[39] LUO, Hongxia; MOHAMMADNIA, Majid. Tuning the HOMO and LUMO energy levels of dye sensitizers with electron-accepting capability and electron-drawing capability of substituents to optimize the efficiency of dye-sensitized solar cells: Approach of theoretical. Inorganic Chemistry Communications, v. 141, p. 109522, 2022. https://doi.org/10.1016/j.inoche.2022.109522

[40] AL-FATLAWE, Bahaa A.; AL-TEMIMEI, Faeq A. Optimizing Electronic and Photovoltaic Properties of D–π–A Organic Dyes for DSSCs Using Density Functional Theory. Journal of Fluorescence, v. 35, n. 9, p. 7833-7845, 2025. https://doi.org/10.1007/s10895-024-04118-5

[41] RAGURAM, T.; RAJNI, K. S. Synthesis and characterisation of Cu-Doped TiO_2 nanoparticles for DSSC and photocatalytic applications. International Journal of Hydrogen Energy, v. 47, n. 7, p. 4674-4689, 2022. https://doi.org/10.1016/j.ijhydene.2021.11.113

[42] WISZ, G. et al. TiO_2: ZnO/CuO thin film solar cells prepared via reactive direct-current (DC) magnetron sputtering. Applied Materials Today, v. 29, p. 101673, 2022. https://doi.org/10.1016/j.apmt.2022.101673

[43] YADETA, Tamasgen Fikadu; IMAE, Toyoko. Effect of carbon dot on photovoltaic performance of n-TiO_2/p-NiO and n-TiO_2/p-CuO heterojunctions in dye-sensitized solar cells. Applied Surface Science, v. 637, p. 157880, 2023. https://doi.org/10.1016/j.apsusc.2023.157880

[44] LEITE, A. M. B. et al. Enhanced photovoltaic efficiency in dye-sensitized solar cells with natural co-sensitizers from Annona squamosa, Malus domestica and Musa fruits. Optical Materials, v. 157, p. 116124, 2024. https://doi.org/10.1016/j.optmat.2024.116124

[45] AGILENT TECHNOLOGIES. Cary 630 FTIR Spectrometer. Disponível em: https://www.agilent.com/en/product/molecular-spectroscopy/ftir-spectroscopy/ftir-benchtop-systems/cary-630-ftir-spectrometer. Acesso em: 10 de março de 2026.

[46] ISMAIL, Ashraf A.; VAN DE VOORT, Frederick R.; SEDMAN, Jacqueline. Fourier transform infrared spectroscopy: Principles and applications. In: Techniques and instrumentation in analytical chemistry. Elsevier, 1997. p. 93-139. https://doi.org/10.1016/S0167-9244(97)80013-3

[47] LIU, Guan-Lin; KAZARIAN, Sergei G. Recent advances and applications to cultural heritage using ATR-FTIR spectroscopy and ATR-FTIR spectroscopic imaging. Analyst, v. 147, n. 9, p. 1777-1797, 2022. DOI: 10.1039/D2AN00005A

[48] SHIMADZU. UV-2600i/UV-2700i – Espectrofotômetro UV-Vis-NIR. Disponível em: https://www.shimadzu.com.br/analitica/produtos/espectroscopia-molecular/uv-vis/espectrofotometro-uv-vis-nir/uv-2600i-uv-2700i/index.html . Acesso em: 12 de março de 2026.

[49] FENG, Xiaoqiang et al. Solid-phase fabrication of TiO_2/Chitosan-biochar composites with superior UV–vis light driven photocatalytic degradation performance. Colloids and Surfaces A: Physicochemical and Engineering Aspects, v. 648, p. 129114, 2022. https://doi.org/10.1016/j.colsurfa.2022.129114

[50] PATNI, Neha; PILLAI, Shibu G. Improvement in the performance of indium free dye sensitized solar cell by the use of polyaniline composite. Materials Chemistry and Physics, v. 329, p. 130108, 2025. https://doi.org/10.1016/j.matchemphys.2024.130108

[51] KAMESH, S. et al. Nitrogen-doped reduced graphene oxide enfolded zinc cobaltite micro flowers as efficient triiodide reduction for a platinum-free counter electrode in dye-sensitized solar cell applications. Electrochimica Acta, v. 475, p. 143262, 2024. https://doi.org/10.1016/j.electacta.2023.143262

[52] ABBOOD, Manal Abdulwahid et al. Enhancing dye-sensitized solar cell performance by employing an innovative WSe2: Zn counter electrode for improved electrocatalytic activity. Materials Science in Semiconductor Processing, v. 171, p. 108015, 2024. https://doi.org/10.1016/j.mssp.2023.108015

[53] UNIVERSITY OF OTAGO. X-ray crystallography. Disponível em: https://www.otago.ac.nz/chemistry/outreach/crystals/x-ray . Acesso em: 15 de março de 2026.

[54] ENCYCLOPAEDIA BRITANNICA. Bragg law. Disponível em: https://www.britannica.com/science/Bragg-law. Acesso em: 15 de março de 2026.

[55] BRUKER. D2 PHASER (without sample changer). Disponível em: https://store.bruker.com/products/d2-phaser-without-sample-changer . Acesso em: 17 de março de 2026.

[56] ALSUHAIBANI, Amnah Mohammed et al. Design of Highly Fluorescent Imidazole-Based Metal-Free D–π–A Dye for DSSC Application. Journal of Fluorescence, v. 35, n. 10, p. 9773-9790, 2025. https://doi.org/10.1007/s10895-025-04278-y

[57] CASTOLDI, Andrea et al. Qualification of the X-ray spectral performance of the DEPFET pixels of the DSSC imager. Nuclear Instruments and Methods in Physics Research Section A: Accelerators, Spectrometers, Detectors and Associated Equipment, v. 1057, p. 168686, 2023. https://doi.org/10.1016/j.nima.2023.168686

[58] BECKHOFF, Burkhard et al. (Ed.). Handbook of practical X-ray fluorescence analysis. Springer Science & Business Media, 2007. https://doi.org/10.1007/978-3-540-36722-2

[59] MALVERN PANALYTICAL. Epsilon 1. Disponível em: https://www.malvernpanalytical.com/en/products/product-range/epsilon-range/epsilon1 . Acesso em: 18 de março de 2026.

[60] JEOL. JSM-7100F Thermal Field Emission Electron Microscope. Disponível em: https://www.jeolbenelux.com/JEOL-BV-News/jsm-7100f-thermal-field-emission-electron-microscope . Acesso em: 19 de março de 2026.

[61] DATYE, Abhaya; DELARIVA, Andrew. Scanning electron microscopy (SEM). In: Springer handbook of advanced catalyst characterization. Cham: Springer International Publishing, 2023. p. 359-380. https://doi.org/10.1007/978-3-031-07125-6_18

[62] HAWKES, Peter W.; HŸTCH, Martin (Ed.). The Beginnings of Electron Microscopy-Part 2. Academic Press, 2022. https://doi.org/10.1016/S1076-5670(22)X0001-4

[63] NANOSURF. Software for AFM systems. Disponível em: https://www.nanosurf.com/en/software . Acesso em: 20 de março de 2026.

[64] JOSHUA, A. M.; CHENG, G.; LAU, E. V. Soft matter analysis via atomic force microscopy (AFM): A review. Applied Surface Science Advances, v. 17, p. 100448, 2023. https://doi.org/10.1016/j.apsadv.2023.100448

[65] ALI, Salah HR. Advanced nanomeasuring techniques for surface characterization. International Scholarly Research Notices, v. 2012, n. 1, p. 859353, 2012. https://doi.org/10.5402/2012/859353

[66] IVIUM TECHNOLOGIES. CompactStat2.h. Disponível em: https://www.ivium.com/product/compactstat2-h/ . Acesso em: 11 de março de 2026.

[67] DA CUNHA, H.O. Enhancing solar energy harvesting through TiO_2-Fe2O3 composite photoanodes sensitized with natural dyes in photovoltaic cells. APPLIED PHYSICS A-MATERIALS SCIENCE & PROCESSING, v. 132, p. 148, 2026. https://doi.org/10.1007/s00339-026-09332-5

[68] DA CONCEIÇÃO, L. R. B. et al. Influence of various solvents in extraction of natural pigments from Annona atemoya and Physalis peruviana as photosensitizers for dye-sensitized solar cells. Optik, v. 300, p. 171635, 2024. https://doi.org/10.1016/j.ijleo.2024.171635

[69] SHAKER, Lina M. et al. Comparative analysis of solar cells and hydrogen fuel: a mini-review. Results in Engineering, v. 23, p. 102507, 2024. https://doi.org/10.1016/j.rineng.2024.102507

[70] BONOMO, M. et al. Unreported resistance in charge transport limits the photoconversion efficiency of aqueous dye-sensitised solar cells: an electrochemical impedance spectroscopy study. Materials Today Sustainability, v. 21, p. 100271, 2023. https://doi.org/10.1016/j.mtsust.2022.100271

[71] LEITE, Arcano Matheus Bragança et al. Use of BODIPY and BORANIL Dyes to Improve Solar Conversion in the Fabrication of Organic Photovoltaic Cells Through the Co-Sensitization Method. Colorants, v. 3, n. 4, p. 311-328, 2024. https://doi.org/10.3390/colorants3040022

[72] LIM, Min-Gyu et al. Evaluation method of internal resistance for repurposing using middle and large-sized batteries. Energies, v. 16, n. 15, p. 5652, 2023. https://doi.org/10.3390/en16155652

[73] LEITE, A. M. B. et al. Construction and characterization of organic photovoltaic cells sensitized by Chrysanthemum based natural dye. Spectrochimica Acta Part A: Molecular and Biomolecular Spectroscopy, v. 284, p. 121780, 2023. https://doi.org/10.1016/j.saa.2022.121780

[74] ABED, Mira; EL-SHAFEI, Ahmed. Dye, DSSC. In: Encyclopedia of Color Science and Technology. Cham: Springer International Publishing, 2023. p. 738-744. https://doi.org/10.1007/978-3-030-89862-5_444

[75] DA CONCEIÇÃO, Leonardo Ricardo Bernardes et al. Evaluation of solar conversion efficiency in dye-sensitized solar cells using natural dyes extracted from Alpinia purpurata and Alstroemeria flower petals as novel photosensitizers. Colorants, v. 2, n. 4, p. 618-631, 2023. https://doi.org/10.3390/colorants2040032

[76] HACHEMI, Nadir et al. Microstructural and phase degradation of monocrystalline solar photovoltaic panels under extreme desert conditions: Insights from XRD and FTIR analysis. Materials Chemistry and Physics, v. 339, p. 130742, 2025. https://doi.org/10.1016/j.matchemphys.2025.130742

[77] ROKHMAT, Mamat et al. Performance improvement of TiO_2/CuO solar cell by growing copper particle using fix current electroplating method. Procedia Engineering, v. 170, p. 72-77, 2017. https://doi.org/10.1016/j.proeng.2017.03.014

[78] KILIC, Bayram et al. Interfacial engineering of CuO nanorod/ZnO nanowire hybrid nanostructure photoanode in dye-sensitized solar cell. Journal of Nanoparticle Research, v. 20, n. 1, p. 11, 2018. https://doi.org/10.1007/s11051-017-4103-4

[79] PATRA, Astam K.; DUTTA, Arghya; BHAUMIK, Asim. Self-assembled ultra small ZnO nanocrystals for dye-sensitized solar cell application. Journal of Solid State Chemistry, v. 215, p. 135-142, 2014. https://doi.org/10.1016/j.jssc.2014.03.036

[80] DOS SANTOS, F. M. M. et al. Effect of bandgap energies by various color petals of Gerbera jamesonii flower dyes as a photosensitizer on enhancing the efficiency of dye-sensitized solar cells. Journal of Materials Science: Materials in Electronics, v. 33, n. 25, p. 20338-20352, 2022. https://doi.org/10.1007/s10854-022-08849-8

[81] ASHOK, Archana et al. Bandgap engineering of CuO/TiO_2 nanocomposites and their synergistic effect on the performance of dye-sensitized solar cells. Optical Materials, v. 148, p. 114896, 2024. https://doi.org/10.1016/j.optmat.2024.114896

[82] ESGIN, Halil; CAGLAR, Yasemin; CAGLAR, Mujdat. Photovoltaic performance and physical characterization of Cu doped ZnO nanopowders as photoanode for DSSC. Journal of Alloys and Compounds, v. 890, p. 161848, 2022. https://doi.org/10.1016/j.jallcom.2021.161848

[83] SEEMA, Humaira et al. Performance evaluation of MXene and N-doped MXene counter electrodes in DSSCs through J–V and impedance spectroscopic analysis. Materials Science and Engineering: B, v. 323, p. 118890, 2026. https://doi.org/10.1016/j.mseb.2025.118890

[84] JOHN, Moriamo O. et al. Photovoltaic performance of semi-pure and crude dye extracts from the leaf of Lonchocarpus cyanescens as natural sensitizer for dye-sensitized solar cell (DSSC). Next Energy, v. 9, p. 100386, 2025. https://doi.org/10.1016/j.nxener.2025.100386

[85] ZHANG, Yameng et al. Sol-gel synthesis of magnesium doped TiO_2 thin film and its application in dye sensitized solar cell. Optical Materials, v. 158, p. 116446, 2025. https://doi.org/10.1016/j.optmat.2024.116446

[86] HOROZ, Sabit et al. Eco-engineered Fe3O4 cellulose APTES nanocomposites as efficient dye-sensitized solar cell counter electrodes: Electrochemical analysis and photovoltaic performance. International Journal of Biological Macromolecules, v. 361, p. 152010, 2026. https://doi.org/10.1016/j.ijbiomac.2026.152010

[87] SHAIKH, Rahilah H. et al. Synthesis of Sb2S3 nanostructures and carbon-based composites: Enhancing electrochemical catalysis and DSSC performance. Next Nanotechnology, v. 9, p. 100416, 2026. https://doi.org/10.1016/j.nxnano.2026.100416

[88] ABIRAM, A. et al. Optimizing anatase TiO_2 through aluminium doping: A comprehensive study for enhanced dye-sensitized solar cell performance. Next Materials, v. 9, p. 101006, 2025. https://doi.org/10.1016/j.nxmate.2025.101006

[89] BHULLAR, Viplove; MAHAJAN, Aman. Cu implanted TiO_2 based dye sensitized solar cells: Unraveling the effect of doping mechanism and type of metal ion on the photovoltaic properties. Solar Energy, v. 254, p. 8-14, 2023. https://doi.org/10.1016/j.solener.2023.03.002

[90] SIBIŃSKI, Maciej et al. Impact of blocking layers based on TiO_2 and ZnO prepared via direct current reactive magnetron sputtering on DSSC solar cells. Scientific Reports, v. 14, n. 1, p. 10676, 2024. https://doi.org/10.1038/s41598-024-61512-6

[91] JU, Hui-Won et al. Fabrication of TiO_2 photoelectrodes doped with copper and zirconium to improve electron generation and flow in dye-sensitized solar cell. Advanced Powder Technology, v. 35, n. 4, p. 104406, 2024. https://doi.org/10.1016/j.apt.2024.104406

[92] ROBLEDO, AG Flota et al. Characterization of natural dyes on ZnO and TiO_2 thin films for applications in DSSC. Journal of Materials Science: Materials in Electronics, v. 34, n. 11, p. 980, 2023. https://doi.org/10.1007/s10854-023-10381-2

[93] THATE, Ankush G. et al. Fabrication of TiO_2-ZnO nanocomposite photoanodes to enhance the dye-sensitized solar cell efficiency: AG. Thate et al. Research on Chemical Intermediates, v. 49, n. 1, p. 147-168, 2023. https://doi.org/10.1007/s11164-022-04878-4

[94] MANIMEKALAI, Alagumalai et al. Synergistic effects in the TiO_2 ZnO/MoSe2 ternary composite photoanode for enhanced solar cell efficiency. Journal of Physics and Chemistry of Solids, v. 204, p. 112786, 2025. https://doi.org/10.1016/j.jpcs.2025.112786

[95] DEMIR, Abdullah; ASLAN, Fehmi; ESEN, Hikmet. TiO_2/ZnO-based composite thin films coated on FTO surface by screen printing method: increasing dye-sensitized solar cell performance. Journal of Materials Science: Materials in Electronics, v. 35, n. 21, p. 1481, 2024. https://doi.org/10.1007/s10854-024-13213-z

[96] URSU, Daniel et al. Efficient indoor dye-sensitized solar cells based on TiO_2 hollow sphere. Journal of Alloys and Compounds, v. 976, p. 173134, 2024. https://doi.org/10.1016/j.jallcom.2023.173134

[97] VARGHESE, Meera; NINAN, Gisa Grace; BALACHANDRAN, Manoj. Carbon dots-Zno/TiO_2 ternary nanocomposite as a proficient material to enhance the performance of natural DSSC. Micro and Nanostructures, v. 194, p. 207934, 2024. https://doi.org/10.1016/j.micrna.2024.207934

[98] DUTTA, Arpita et al. Precipitation-assisted, low-temperature-annealed TiO_2 and its nanocomposites-based photoanode for DSSCs. Journal of Materials Science: Materials in Electronics, v. 35, n. 4, p. 292, 2024. https://doi.org/10.1007/s10854-024-12055-z

[99] BROSEL-OLIU, Sergi et al. Impedimetric transducers based on interdigitated electrode arrays for bacterial detection–A review. Analytica chimica acta, v. 1088, p. 1-19, 2019. https://doi.org/10.1016/j.aca.2019.09.026

[100] MOHAMMADIAN, Jamal et al. Electrochemical impedance spectroscopy analysis of dye-sensitized solar cells composed of electrospun composite photoanodes: A comparative study of natural and synthetic sensitizers. Optik, v. 303, p. 171730, 2024. https://doi.org/10.1016/j.ijleo.2024.171730